

Muon induced secondary electrons at the KATRIN experiment

Detector installation and setup & data analysis

Diplomarbeit
von

Philipp Rovedo

An der Fakultät für Physik
IKP - Institut für Kernphysik - KIT Karlsruhe

Erstgutachter:	Prof. Dr. Guido Drexlin
Zweitgutachter:	Prof. Dr. Ulrich Husemann
Betreuernder Mitarbeiter:	Dr. Nancy Wandkowsky
Zweiter betreuender Mitarbeiter:	Benjamin Leiber

Bearbeitungszeit: 27. September 2012 – 01. Oktober 2013

Ich versichere wahrheitsgemäß, die Arbeit selbstständig angefertigt, alle benutzten Hilfsmittel vollständig und genau angegeben und alles kenntlich gemacht zu haben, was aus Arbeiten anderer unverändert oder mit Abänderungen entnommen wurde.

PLACE, DATE

.....
(YOUR NAME)

Contents

1. Introduction	3
1.1. Neutrinos - the early years	3
1.2. Neutrino sources	4
1.3. Neutrinos in the standard model	5
1.4. Neutrino Oscillations	7
1.5. Indirect measurement of the neutrino mass	9
1.6. Direct measurement of the neutrino mass	10
1.7. Cosmic rays from the viewpoint of KATRIN	11
2. KATRIN experiment	15
2.1. Measurement principle	15
2.1.1. MAC-E Filter	16
2.2. Experimental Setup	18
2.2.1. WGTS and Rear Section	18
2.2.2. Transport Section	19
2.2.3. Pre-Spectrometer	21
2.2.4. Main Spectrometer	21
2.2.5. Monitor spectrometer	21
2.2.6. Focal Plane Detector System	21
2.2.7. Solenoids, LFCS and EMCS system	22
2.2.8. Background sources	24
3. Muon detection system	25
3.1. Data aquisition crate	28
3.1.1. First level trigger cards	28
3.1.2. Second level trigger cards	28
3.2. Orca control	28
3.3. Scintillator modules	29
3.4. Photomultipliers	30
3.5. Gains, Thresholds and Acceleration Voltages	31
4. Analysis software	35
4.1. Data structure	35
4.2. Search Algorithms	36
4.2.1. Frequency Search	37
4.2.2. Incremental Search	37
4.3. Member Functions of the class run	37
5. Simulation of Background Inducing Muons	43
5.1. Geant4	43
5.2. Geometry Setup	44
5.3. Muon Generator	44

5.4. Hit Counter	45
6. Comissioning measurements and analysis	47
6.1. Finding the best filter settings	47
6.2. Rates of single muon modules	49
6.3. Operation in high magnetic fields	49
6.4. Module Stability	51
6.5. Module Efficiency	51
6.6. Photo Multiplier Tube Test with ^{90}Sr source	53
6.7. Synchronization of moun detection system and FPD DAQs	54
6.8. Coincidence Search between Muon- and Detector Events	57
6.8.1. Monitor Spectrometer	60
6.8.2. Main Spectrometer	62
7. Conclusion & Outlook	69
Bibliography	71
Annex	77
A. ORCA air coil script	77
B. Connection scheme DAQ & high voltage settings	79
C. Weather data Christmas 2012	80
D. Other monitor spectrometer settings	81
E. Monitor spectrometer field setup and analysis	82
F. Main spectrometer analysis	92
G. A vis.mac file	92

List of Figures

1.1. Neutrino Sources	4
1.2. Standard Model Particles	6
1.3. Neutrino Mass Hierarchy	7
1.4. Effective Neutrino Mass	8
1.5. Cosmic Ray Composition	12
1.6. Landau Distribution	14
2.1. Schematic Tritium Energy Spectrum	16
2.2. MAC E Filter	17
2.3. KATRIN Beam Line	19
2.4. Rear Section and WGTS	20
2.5. DPS and CPS	20
2.6. Main Spectrometer and Wire Electrodes	22
2.7. Focal Plane Detector system	23
2.8. Detector wafer	23
2.9. Wire Electrodes	24
3.1. Muon module setup	26
3.2. East side modules	26
3.3. East side modules	26
3.4. Monitor spectrometer modules	27
3.5. Grounded multiplug	27
3.6. High voltage supplies	27
3.7. Photomultiplier tube	31
3.8. Muon modules' rate: noise problems	31
3.9. Six channel energy histogram with noise	32
3.10. Landau peak 1200 V acceleration voltage	33
3.11. Landau peak 1500 V acceleration voltage	33
4.1. Frequency search Algorithm	38
4.2. Incremental search Algorithm	38
5.1. Simulation Geometry Setup	44
5.2. Muon Angular Distribution	45
6.1. Muon Signal Shape	48
6.2. Function Generator Pulse Shape	48
6.3. Rate dependence on Magnetic Fields	50
6.4. Muon Module Stability	52
6.5. Daily Average Muon Rate	52
6.6. Cobalt Decay Scheme	54
6.7. Cobalt parallel scan	55
6.8. Cobalt perpendicular scan	55

6.9. Testing of Muon Modules with Sr Source - Modules 1 & 2	56
6.10. Testing of Muon Modules with Sr Source - Modules 3 - 5	56
6.11. Testing of Muon Modules with Sr Source - Modules 6 - 8	57
6.12. DAQ Synchronisation	58
6.13. Modules 1& 2 at Steep Cone	63
6.14. Flux Tube Setting A	65
6.15. Flux Tube Setting B	65
6.16. Flux Tube Setting C	66
6.17. Main Spectrometer Simulation	67
6.18. Main Spectrometer Peak?	67
B.1. FLT connector card	79
E.2. Asymmetric field 50 A	82
E.3. 50 A loops	82
E.5. 25 A asymmetric	83
E.4. 25 A asymmetric	83
E.6. 50 A loops	84
E.7. 50 A loops	84
E.8. 50 A loops	85
E.9. 50 A loops	85
E.10. 0 A loops	86
E.11. 0 A loops analysis	86
E.12. 0 A loops	87
E.13. 0 A loops analysis	87
E.14. 50 A loops	88
E.15. 50 A loops analysis	88
E.16. -50 A loops	89
E.17. -50 A loops analysis	89
E.18. 25 A loops	90
E.19. 25 A loops	90
E.20. 50 A loops	91
E.21. 50 A loops	91

List of Tables

1.1. Elementary Interactions	6
1.2. Neutrino Parameters	9
5.1. Angular Distribution Coefficients	45
5.2. Simulation Comparison	46
5.3. Single & Multi side Event Ratio	46
6.1. Energy Resolution dependent on Filter Setting	49
6.2. LFCS settings Stability Measurement	51
6.3. Synchronization Test Settings	59
6.4. Asymmetric Magnetic Field Measurements	60
6.5. Non Axially-Symmetric Magnetic Field Measurements	61
6.6. Main Spectrometer Runs	64
6.7. Main Spectrometer Magnetic field settings	64
B.1. High voltage settings	79
B.2. Main spectrometer DAQ channel assignment	79
C.3. Temperature and pressure Rheinstetten	80

Deutschsprachige Zusammenfassung

Die drei Neutrinos, nach der Postulation durch Pauli inzwischen etablierte Elementarteilchen, sind die einzigen Teilchen des Standardmodells, deren Masse bisher unbekannt ist. Zahlreiche Oszillationsexperimente haben gezeigt, dass die Masse endlich ist, finden jedoch nur Zugang zu den Differenzen der Massenquadrate. Die Bestimmung einer dieser Massen, die des Elektron-Neutrino, hat sich das KATRIN Experiment (Karlsruher Tritium Neutrino Experiment) zum Ziel gesetzt. Dabei nutzt es eine, im Gegensatz zu neutrinolosem doppeltem Beta-Zerfall oder kosmologischen Betrachtungen, modellunabhängige Methode. Die Zerfallselektronen des Tritium werden mit Hilfe eines MAC-E Filters analysiert. Dieser parallelisiert die Impulse der Elektronen aus einer isotrop strahlenden Quelle, um sie dann durch ein elektromagnetisches Potential zu analysieren. Dazu ist ein raffiniertes System aus Supraleitern und normalleitenden Spulen nötig, die die Zerfallselektronen in einem magnetischen Flusschlauch von der Quelle zu einem Detektor führen. Betrachtet wird der Endpunkt des Spektrums, dessen Form von der Masse des Elektron-Neutrinos am stärksten beeinflusst wird. Das KATRIN Experiment wird diesen Endpunkt mit bisher unerreichter Genauigkeit darstellen. Es wird in der Lage sein, eine Neutrinomasse von $0.2 \text{ eV}/c^2$ bei 90 % C.L. zu messen und damit die Vorgängerexperimente von Mainz und Troisk um eine Größenordnung übertreffen. Um außerdem den Betrag des elektrischen Potentials genau verfolgen zu können, vermisst das Monitorspektrometer, an welchem im Rahmen dieser Arbeit ebenfalls Messungen durchgeführt wurden, Transmissionsfunktionen von β -Quellen bekannte Energie. Für einen solch präzisen Messaufbau sind die genaue Kenntnis aller Untergrundprozesse, die das Messergebnis verfälschen können, notwendig. Neben Elektronen aus Zerfällen im Innern der Messapparatur können solche auch extern induziert werden. Den relevanten Beitrag liefern hierbei Myonen aus kosmischen Luftschaubern, die durch Streuung an den Wänden des Tanks Elektronen aus dieses auslösen. Als Gegenmaßnahme sind im Innern des Spektrometertanks Elektroden installiert. Diese liegen auf einem negativeren Potenzial als die Tankwand und schirmen so den magnetischen Flusschlauch im Innern gegen die Untergrund-Elektronen ab. Hochenergetische Elektronen können jedoch noch immer in das sensitive Volumen eindringen. Außerdem bieten die Elektroden selbst sowie ihre Haltestrukturen wiederum eine, wenngleich weitaus kleinere, Angriffsfläche für Myonen.

Diese Arbeit beschäftigt sich mit dem Nachweis und der Simulation kosmischer Myonen sowie der Analyse der gewonnenen Daten. Dazu wurde in ihrem Rahmen zunächst das aus acht Szintillatormodulen und Ausleseelektronik bestehende Myon Detektionssystem des Hauptspektrometers fertiggestellt. Der gesamte Aufbau wurde strukturiert verkabelt, Hochspannungsgeräte wurden beschafft und installiert, die Erdung angebracht, Synchronisation mit dem Datennahmesystem des Detektors hergestellt. Parallel wurden erste Analysen vorläufiger Messungen zur Inbetriebnahme durchgeführt. Diese dienten weitestgehend dem Test und der Inbetriebnahme der Module. So wurden passende Software Gains und Thresholds gesetzt und Beschleunigungsspannungen eingestellt. Beim Test der Photomultiplier mithilfe einer Strontium Quelle wurde die Notwendigkeit der Erhöhung der Beschleunigungsspannungen zweier Modulseiten festgestellt. Um die kurzen Pulse (20 ns)

der Module zuverlässig zu identifizieren, wurden verschiedene Software Filter mit einem Funktionengenerator auf ihre Energieauflösung hin untersucht und optimiert. Aufgrund der räumlichen Nähe zum Low Field Compensation System (LFCS), das den magnetischen Flusschlauch formt, sind die Photomultiplier einem magnetischen Feld ausgesetzt, unter welchem sie nicht mehr zuverlässig funktionieren. Um dem entgegenzuwirken, wurden die Photomultiplier von einer Mu-Metallschicht umhüllt, die das Feld im innern aufgrund ihrer hohen magnetischen Permeabilität verringert. Das neue Setup wurde unter den höchsten zu erwartenden Feldern getestet und zeigte einen deutlich geringeren, akzeptablen Abfall der Rate. Eine Langzeitmessung zeigte, dass die Module weit stabiler sind, als der durch natürliche Fluktuationen der Atmosphäre Temperatur beeinflusste Myonfluss. Die Effizienz der Module wurde zu $(93.4 \pm 3.4)\%$ bestimmt. Zur Verifizierung experimentell bestimmter Daten wurde eine Geant4-Simulation erstellt. In dieser wurden die Raten der Myonmodule verifiziert und sie kann weiter zur Simulation von Myon-induziertem Untergrund genutzt werden.

Die Messungen am bereits installierten Myon Detektionssystem am Monitorspektrometer wurden wieder aufgenommen. Dabei sind Messungen mit asymmetrischem und nicht axialsymmetrischem Feld durchgeführt worden. Bei asymmetrischem Feld verbinden magnetische Feldlinien die Wand des Spektrometers mit dem Detektor - die Myon induzierten Elektronen werden magnetisch zum Detektor geführt. Bei nicht axialsymmetrischem Feld wird das Feld durch das Zuschalten einer Spule verformt, sodass die magnetische Reflexion, die den Untergrund sonst abschirmt, weniger gut wirkt. So können Elektronen den Detektor durch $E \times B$ drifts mit weit höherer Wahrscheinlichkeit erreichen. Zur Auswertung der Daten wurde auf das Myon Detektionssystem zugeschnittene Software geschrieben. Diese wurde für an Haupt- und Monitorspektrometer gewonnene Messungen genutzt. In den Messungen konnte gezeigt werden, dass die Myon induzierte Elektronen Rate am Detektor, die über zeitliche Korrelation zum Detektor-Event ($\approx 1.5\text{ }\mu\text{s}$ später) identifiziert wurde, mit der Symmetrisierung des Feldes abnimmt. Während der „SDS commissioning measurements“, einer ersten Messphase am Spektrometer und Detektor System wurden erste Untersuchungen des Myon induzierten Untergrundes am Hauptspektrometer durchgeführt. Diese Messungen zeigten trotz mehrfacher Anpassung des magnetischen Setups keine klaren zeitlichen Korrelationen zwischen Myon Detektionen und Detektor Events. Da in Simulationen gezeigt wurde, dass die Flugzeiten der Elektronen im Bereich der Rate der die vom Flusschlauch abgebildeten Fläche durchdringenden Myonen liegt, sollten zukünftige Messungen den Anspruch haben diese Fläche so klein wie möglich zu halten. Dazu bietet sich auch die Analyse einzelner Detektorpixel oder -ringe an, hier war die Analyse aufgrund der begrenzten Messdauer jedoch statistisch limitiert.

Mit dem Abschluss dieser Arbeit wird ein voll funktionsfähiges und intensiv getestetes System übergeben, mit welchem gezeigt werden konnte, wie wichtig die Kenntnis aller Magnetfelder und ihre Symmetrisierung sind. Zudem wurden Softwarepakete zur Simulation und Auswertung gewonnener Daten erstellt, die zukünftige Messungen erleichtern und Voraussagen zulassen.

1. Introduction

Ever since the beginning of the 19th century science in general but especially the field of physics has been undergoing an unbelievably quick and vast development. The possibilities arising from automated analysis through the use of advanced computation grids connected to the optimization of manufacturing processes for detectors leave the world - and even scientists - amazed. Nevertheless, with more and more phenomena well understood, the remaining tasks often require huge projects and large collaborations. One of these projects, aimed to determine the effective mass of the electron anti-neutrino, is the KATRIN experiment. Working on the project is a liaison of 15 universities and research facilities with over 150 coworkers aspiring to find the absolute neutrino mass scale.

This chapter will put the KATRIN experiment in the context of neutrino physics in general. At first, an introduction covering the postulation and discovery of the neutrino is given (section 1.1), followed by a discussion on different neutrino sources (section 1.2) and the role of neutrinos in the Standard Model (section 1.3) as well as latest results from research, most notably neutrino oscillations (section 1.4). The different methods to determine the neutrino mass scale are illustrated in sections 1.5 and 1.6. Finally, section 1.7 will be devoted to cosmic air showers, which are of importance in the context of this thesis.

1.1. Neutrinos - the early years

The neutrino was initially postulated by Wolfgang Pauli, then under the name “neutron”, as an explanation for the beta decay spectrum showing a continuous energy distribution which did not concur with the idea of a two body decay [1]:

$$p \rightarrow n + e^- . \quad (1.1)$$

The conservation laws of energy, momentum and angular momentum were apparently violated in the process. The problem could be solved by the addition of the neutrino, which carries a portion of the decay energy as kinetic energy, thus allowing for a continuous spectrum

$$p \rightarrow n + e^- + \bar{\nu}_e . \quad (1.2)$$

To comply with the conservation laws, the new particle needed to be of spin 1/2 and chargeless. The first experimental evidence for this particle was then given by Cowan and Reines [2] who observed the induced reaction of electron anti-neutrinos, produced in large quantities by a nearby nuclear reactor, with protons in a water-based detector:

$$\bar{\nu}_e + p \rightarrow e^+ + n . \quad (1.3)$$

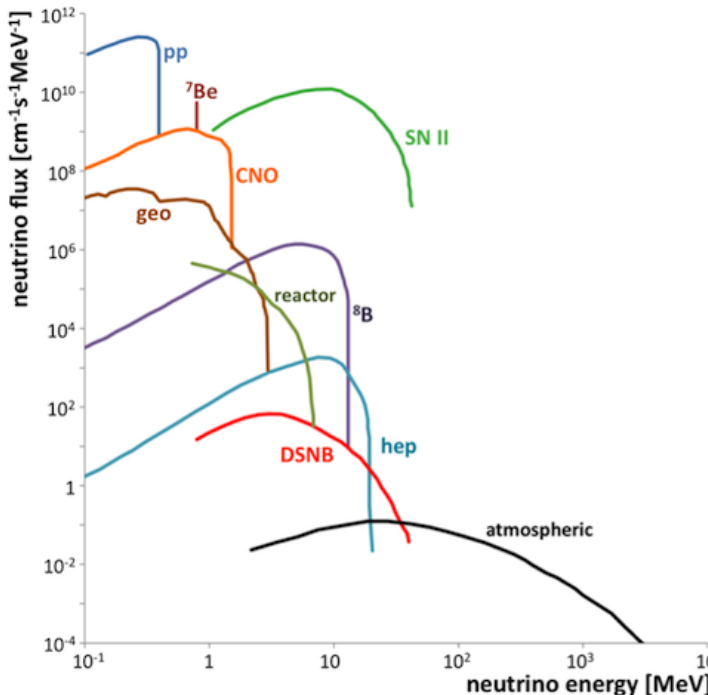


Figure 1.1.:

A graph summarizing different neutrino sources fluxes both natural and artificial. The sun is the most prominent neutrino source, contributing through various nuclear fusion chains (pp, ^{7}Be , CNO, ^{8}B , hep). The energy range between 1 and 100 MeV is dominated by supernovae type II. Further natural sources are geoneutrinos in the energy regime up to a few MeV, the diffuse supernovae background between 1 and 100 MeV and atmospheric neutrinos beyond 1 MeV. The only artificial source are nuclear reactors, producing neutrinos of energies between 1 and 10 MeV. Figure from [6].

The characteristic neutrino signal is composed of two coincident components: a pair of 511 keV photons from the immediate electron-positron annihilation followed by additional γ s from neutron capture some μs afterwards. Following the electron neutrino, both other known neutrino generations have been attested for in various experiments, the first ones to find evidence for ν_μ and ν_τ were to be Danby and Gaillard [3] and the DONUT experiment [4] respectively.

1.2. Neutrino sources

Neutrino properties are studied using a variety of natural and artificial neutrino sources, covering all energies. An overview of those natural sources which create the largest flux through the earth, as well as artificial sources is given in figure 1.1 and described below [5].

- **Primordial neutrinos**

Lingering around since the “Big Bang”, neutrinos with thermal energies at $T_\nu \approx 1.95\text{ K}$ form a cosmic neutrino background. These neutrinos decoupled shortly after the Big Bang when the weak interaction rate dropped below the expansion rate of the Universe. Due to this “freeze-out” of thermal equilibrium with the other particles, mainly protons, neutrons, and electrons, a relic neutrino density of 336 cm^{-3} is found nowadays.

- **Supernovae neutrinos**

Supernovae type II, which occur less often than the type I and only in stars with $M > 8M_\odot$, are known to produce large quantities of neutrinos. Inside the burned-out collapsing star, the electrons’ degeneracy pressure leads to de-leptonization of the core by electron capture:



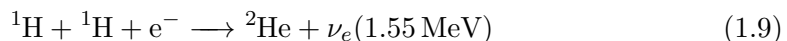
This process produces high energy neutrinos, which can leave the core and carry away energy in the process - and large quantities of that. About 99 % of the energy released during a type II supernova cooling phase is carried away by neutrinos.

- **Solar neutrinos**

The dominant energy production mechanism is the pp reaction chain 1.5, which produces neutrinos in a continuous energy range up to a maximum of 0.42 MeV. Additional subdominant fusion chains release neutrinos of higher energies:



Further on, electron capture processes add line spectra to the picture



where ${}^7\text{Be}$ emits at two energies: mostly at 0.86 MeV (90 %) and another, lower energy line at 0.38 MeV (10 %) [7].

These reactions are responsible for the largest part of the solar neutrino flux through the earth. Predictions on this flux are shown in figure 1.1 together with other model calculations on flux expectations. Solar neutrinos were essential for oscillation research thereby proving that neutrinos are in fact massive (see chapter 1.4).

- **Atmospheric neutrinos**

As described in section 1.7 cosmic rays, consisting mostly of protons, constantly impact onto the upper layers of the atmosphere. There, they create air showers, cascades of the initial high energy particles into thousands of particles of lower energies. In that process, muons are created which can significantly contribute to the background of KATRIN.

- **Reactor neutrinos**

Nuclear fission produces large quantities of neutrons that decay according to



A fission reactor, in which many of these reactions concur, is hence a strong source of neutrinos, depending on the reactor's size. On average, around 6 neutrinos per fission reaction emerge. These sources are used in many experiments, among other things to prove the existence of neutrino oscillations (see chapter 1.4). The Daya Bay experiment for example was able to attest the disappearance of $\bar{\nu}_e$, thereby determining the last mixing angle θ_{13} [8].

- **Neutrinos from β decays**

Very important for the KATRIN experiment are neutrinos from beta decays, more precisely the tritium beta decay. This is described in more detail in chapter 2.1.

1.3. Neutrinos in the standard model

In the second half of the 20th century, the Standard Model was developed, which describes nowadays particle physics most precisely. It contains six quarks and six leptons, each group divided into three particle generations. making up the matter as well as four types of gauge bosons. The latter are carriers of interactions via the exchange between the Standard

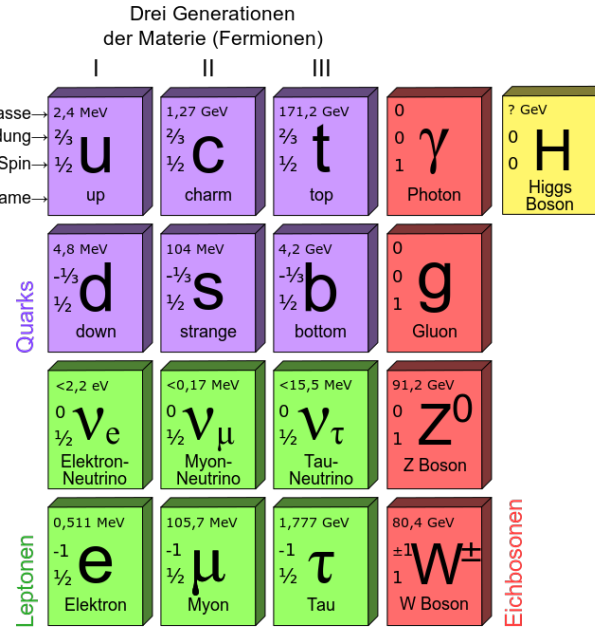


Figure 1.2.: Particle content of the standard model. Upper left, purple: Quarks, the building blocks of hadrons. Lower left, green: Leptons, which neutrinos belong to. Right, red: Bosonic force carriers. Upper right, yellow: Higgs particle. [11]

Table 1.1.: A comparison of the strength of the different interactions relative to the strong force and of their ranges [12].

Force	strong	electromagnetic	weak	gravitation
relative strength range	1 $\approx 1 \text{ fm}$	10^{-2} ∞	10^{-5} $\approx 10^{-3} \text{ fm}$	10^{-40} ∞

Model particles. Lately, proof for existence of the Higgs particle, a scalar boson, responsible for the generation of particle masses, was found at CERN [9, 10]. It was the last missing piece to complete the Standard Model. For our universe, gravity, mediated by the graviton, plays a major role for formation and stability of the larger structures. In particle physics investigations however, it can mostly be neglected. Here, only the strong and weak as well as the electromagnetic interaction contribute noticeably to phenomena observed. That is why, in the standard model, gravity as well as its carrier, the graviton, are disregarded.

Most of what we can experience in our daily life or in experiments at low energies is attributable to the electromagnetic force or gravity, however, strong and weak interaction do play a major role when it comes to high energy physics, where their limited reach is overcome by small distances between interacting particles. In case of the neutrino, its detection and thereby study of its characteristics is very difficult as it interacts only gravitationally and weakly. Although the weak interaction is a lot stronger compared to gravity, it is still weak compared to both electromagnetic and strong interactions. Therefore the neutrino is considered elusive, the detection efficiencies are low and only large scale detectors are able to detect statistically relevant amounts of neutrinos.

One method used quite frequently is the Cherenkov radiation emitted by particles traveling through matter faster than the matter-specific speed of light. The occurring cones of light, comparable to the supersonic cones caused by planes in air, can be detected by photomultiplier tubes. The challenges are the large target volumes and a maximization of the surface coverage with PMTs, which are required to determine the direction and energy

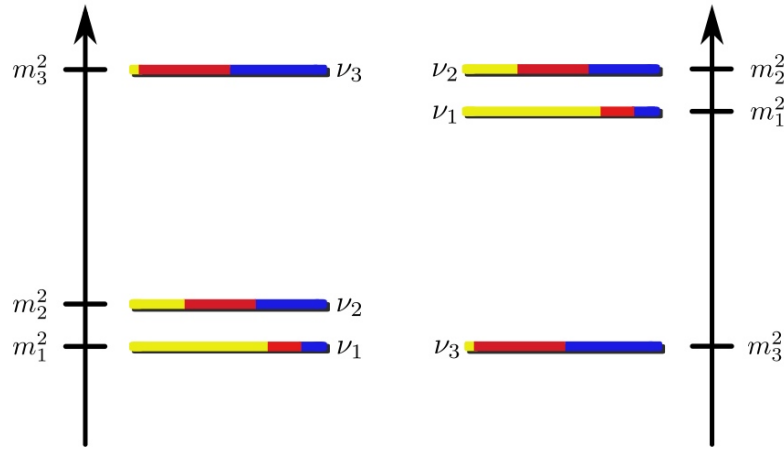


Figure 1.3.: The possible mass hierarchies for neutrinos. Left: normal scheme with $m_{\nu_1} < m_{\nu_2} < m_{\nu_3}$. Right: inverted scheme where $m_{\nu_1} < m_{\nu_2}$ is still true, though $m_{\nu_3} < m_{\nu_1}$. The colored bars represent the corresponding flavor content, i.e. the probability of measuring a specific flavor eigenstate when detecting a pure mass eigenstate. Yellow represents ν_e , red ν_μ and blue ν_τ [18].

of the incoming neutrino. This is why most experiments make use of “natural” detectors such as water, e.g. Super-Kamiokande and Antares, [13, 14] or ice [15]. Other approaches rely on the inverse beta decay of reactor neutrinos within the target material:



1.4. Neutrino Oscillations

In the Standard Model, neutrinos are considered to be massless. Many experiments such as Kamiokande [14], Daya Bay [16] or SNO [17] though have shown that neutrinos are indeed massive by observation of neutrino oscillations with both reactor neutrinos and solar neutrinos. Important for those experiments is the precise knowledge of the source distance to detector and the energy distribution of the neutrinos.

However, until now, only the mixing angles and the differences of the squared masses are known. While the mixing angles determine the flavor content of each mass eigenstate, see figure 1.3, the absolute mass scale is fixed by the lightest mass eigenstate m_{\min} , which is not known, see figure 1.4. Two mass schemes are possible: the normal and the inverted one. Normal means that the smallest number also describes the smallest mass state, i.e. $m_{\nu_1} < m_{\nu_2} < m_{\nu_3}$. In the inverted scheme, the squared mass difference of eigenstates two and three is not directed upwards, but pushes the m_{ν_3} mass below the other two.

If the neutrinos were massless, their mass eigenstates would equal their flavor eigenstates. First hints against this assumption occurred as inconsistencies between the measured and the calculated solar ν -flux occurred in experiments at the Homestake mines [19]. To explain the missing ν_e , the theory of neutrino oscillations emerged, where each flavor is made up of all three mass eigenstates. This mixture is described by the so called Pontecorvo-Maki-Nakagawa-Sakata matrix:

$$\begin{pmatrix} |\nu_e\rangle \\ |\nu_\mu\rangle \\ |\nu_\tau\rangle \end{pmatrix} = \begin{pmatrix} U_{e,1}^* & U_{e,2}^* & U_{e,3}^* \\ U_{\mu,1}^* & U_{\mu,2}^* & U_{\mu,3}^* \\ U_{\tau,1}^* & U_{\tau,2}^* & U_{\tau,3}^* \end{pmatrix} \begin{pmatrix} |\nu_1\rangle \\ |\nu_2\rangle \\ |\nu_3\rangle \end{pmatrix} \quad (1.12)$$

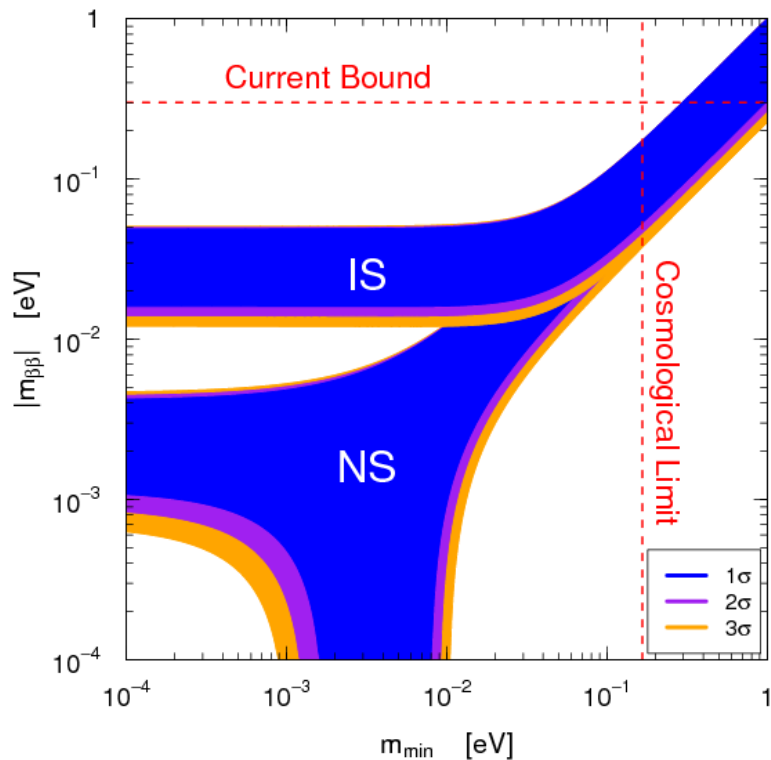


Figure 1.4.: The possible effective masses for neutrinos depending on the lightest neutrino mass m_{min} shown on the x-axis. Normal and inverted scheme are marked NS and IS. The current bound from $0\nu\beta\beta$ decay is displayed as well as cosmological limitations.

Table 1.2.: Given are the latest measurement results of the mixing angles and squared mass differences. For $\sin^2(2\Theta_{23})$, only the lower limit is given [20].

parameter	value
$\sin^2(2\Theta_{12})$	0.875 ± 0.024
Δm^2_{21}	$(7.50 \pm 0.20) \times 10^{-5} \text{ eV}^2$
$\sin^2(2\Theta_{23})$	>0.95
Δm^2_{32}	$(2.32 \pm 0.12) \text{ eV}^2$
$\sin^2(2\Theta_{13})$	0.095 ± 0.010

In this equation, the matrix U can be parametrized through a combination of three rotation matrices and a complex phase factor δ_D , the so called Dirac phase, as well as two complex Majorana phases δ_M

$$U = \begin{pmatrix} 1 & 0 & 0 \\ 0 & c_{23} & s_{23} \\ 0 & -s_{23} & c_{23} \end{pmatrix} \begin{pmatrix} c_{13} & 0 & s_{13}e^{-i\delta_D} \\ 0 & 1 & 0 \\ -s_{13}e^{-i\delta_D} & 0 & c_{13} \end{pmatrix} \cdot \begin{pmatrix} c_{12} & s_{12} & 0 \\ -s_{12} & c_{12} & 0 \\ 0 & 0 & 1 \end{pmatrix} \begin{pmatrix} e^{i\delta_{M1}} & 0 & 0 \\ 0 & e^{i\delta_{M2}} & 0 \\ 0 & 0 & 1 \end{pmatrix}. \quad (1.13)$$

where $c_{ij} = \cos \theta_{ij}$ and $s_{ij} = \sin \theta_{ij}$.

Initially, the neutrino is created in a pure flavor eigenstate $|\nu_\alpha\rangle$, which can be described by the three matrix elements and the corresponding mass eigenstates:

$$|\nu_\alpha(t=0)\rangle = U_{\alpha 1}^* |\nu_1\rangle + U_{\alpha 2}^* |\nu_2\rangle + U_{\alpha 3}^* |\nu_3\rangle. \quad (1.14)$$

The time evolution of this state now reveals the oscillatory behavior of the neutrino, as evolving states are no longer pure flavor eigenstates:

$$|\nu_\alpha(t>0)\rangle = U_{\alpha 1}^* e^{-iE_{\alpha 1}t} |\nu_1\rangle + U_{\alpha 2}^* e^{-iE_{\alpha 2}t} |\nu_2\rangle + U_{\alpha 3}^* e^{-iE_{\alpha 3}t} |\nu_3\rangle \neq |\nu_\alpha\rangle. \quad (1.15)$$

The time-dependent probability to find a certain flavor eigenstate $|\nu_\alpha\rangle$ is then given by

$$|\nu_\alpha(t)\rangle = \sum_{k=1,2,3} U_{\alpha k}^* \exp(-iE_k t) |\nu_k\rangle. \quad (1.16)$$

If the mass eigenstates in turn are expressed as a mixture of flavor eigenstates, one can extract the prefactor of the sum's components as the transition probability for each single flavor:

$$P(\nu_\alpha \rightarrow \nu_\beta) = |\langle \nu_\beta | \nu_\alpha(t) \rangle| = \left| \sum_{k=1,2,3} U_{\alpha k}^* \exp(-iE_k t) U_{\beta k} \right|^2 \quad (1.17)$$

Table 1.2 summarizes the experimental results for the mixing angles and squared mass differences. Though the mixing angles and mass differences have been determined, more precise measurements are required to determine the mass hierarchy and the CP-violating phase(s). For this purpose, new experiments such as LENA [21] are being built.

1.5. Indirect measurement of the neutrino mass

The absolute neutrino mass scale can be accessed indirectly, through data that is affected by a non-zero neutrino mass but where this mass itself is not a direct observable. The main approaches, namely the neutrinoless double beta-decay and cosmological observations, are shortly discussed in the following.

Neutrinoless double beta decay ($0\nu\beta\beta$)

The double beta decay process ($2\nu\beta\beta$) in which two neutrinos are emitted, only occurs if the single β decay to the $^{A}_{Z+1}X$ daughter nucleus is prohibited by energy conservation. Within the $2\nu\beta\beta$ decay



two neutrinos are emitted alongside two electrons. In contrast, no neutrinos are emitted within the $0\nu\beta\beta$ decay, which can exist only if the neutrino is its own anti-particle, a so called Majorana neutrino. Then, if a nucleus undergoes double beta decay, the neutrino from one vertex can be absorbed in the second vertex as an anti-neutrino with inverted helicity - or vice versa. As this change in helicity is only possible for a massive particle, the $0\nu\beta\beta$ decay would be further proof of a massive neutrino. Furthermore, as the probability for a helicity change depends on the particle mass, the decay rate, and consequently the half life $t_{1/2}$, depend on the effective Majorana neutrino mass [22]:

$$\Gamma_{0\nu\beta\beta} \propto \left| \sum_{i=1}^3 U_{ei}^2 m(\nu_i) \right|^2. \quad (1.19)$$

Cosmological observations

The problem can also be approached by calculations using astrophysical data.

For one, the formation of structures in the universe depends on the neutrino mass. Acting as hot dark matter, neutrinos wash out small scale structures. Consequently, small scale fluctuations in the matter power spectrum are suppressed by massive neutrinos. Using the spectroscopic data from galaxy surveys like SDSS [23] or studying the cosmic microwave background like WMAP [24] or Planck [25], an upper limit of $\sum_{\nu} m_{\nu} < 0.6$ eV can be obtained.

As these indirect methods for neutrino mass measurements strongly depend on model assumptions, the direct methods, which are discussed in the next section, play a key role in the determination of a model-independent value of the neutrino mass.

1.6. Direct measurement of the neutrino mass

Direct measurements of the neutrino mass rely on a precise determination of the electron energy spectrum of single β decay. The advantage of direct measurements is that they only rely on the relativistic energy-momentum-relation $E^2 = m^2 c^4 + p^2 c^2$, which makes the results mostly model independent. There are spectrometric as well as calorimetric approaches. To increase their sensitivity, current experiments have to be scaled up either in size (spectrometer) or in target mass (calorimeter). With the KATRIN experiment, the spectrometer approach has reached its technical limits. Although the calorimetric approach is further scalable, the necessity of ten thousands of single detectors is a big challenge. A big advantage of the KATRIN experiment is the ability to select only the spectral part close to the decay endpoint, which is relevant for the neutrino mass determination. Consequently, a high luminosity can be achieved without suffering from pile-up effects. Tritium was chosen as β -emitter for several reasons listed below.

- A high luminosity is ensured by the short half life of $t_{1/2} = 12.3$ a. Consequently, small amounts of the emitter are sufficient to ensure good statistical results.
- At the same time, the inverse of the cubic endpoint energy ($1/E_0^3$) defines the amount of electrons emitted in the endpoint region (up to 1 eV below the endpoint). Tritium's low endpoint energy of 18.6 keV, undercut only by one β emitter, rhenium, that has other disadvantages, ensures a high luminosity at the detector.

- As tritium beta decay is a superallowed process [26], the matrix element $|M_{had}|$ is energy independent, which significantly simplifies the analysis procedures.
- Another simplification compared to other β -emitters is the easily calculable electron shell configuration, which allows a determination of the spectrum of excited states.
- Concerning scattering of signal electrons on tritium atoms in the source volume, the low atomic number makes for small cross sections in inelastic scattering. This reduces energy smearing inside the source volume.

These reasons make tritium the element of choice for KATRIN.

The above mentioned rhenium is used in the calorimetric approach. Experiments like MARE [27] use rhenium in bolometers as both emitter and detector. The low endpoint energy of 2.47 keV results in a large fraction of electrons with energies near this endpoint. However, this is largely compensated by the much longer half life of $t_{1/2} = 4.32 \times 10^{10}$ a. Still, the mass of rhenium required to gain statistically relevant results remains below the tritium mass used in KATRIN. The MARE strategy is to split the radioactive material and use it in many small micro-bolometers. That is beneficial as readout is slow and the rate per bolometer is reduced by lowering the emitter mass. Thermistors then sample the temperature, catching peaks induced by electrons from β decays scattering inside the solid source. The experiment set up by the Milano collaboration has set an upper limit of

$$m_{\bar{\nu}_e} < 15 \text{ eV at 90 \% C.L..} \quad (1.20)$$

This limit shall be pushed to 0.2 eV according to [27].

1.7. Cosmic rays from the viewpoint of KATRIN

When high energy particles hit the upper atmosphere, a cascade of particles, generated from the interaction with atmospheric molecules and atoms, follows. Most primary particles are nucleons, most of which again are free protons (85%), i.e. hydrogen ions, followed by α particles (15%). The flux of helium nuclei is already about an order of magnitude below the hydrogen ones and higher mass number nuclei show even lower rates, see figure 1.5 [28]. A large number of secondary particles is created via electromagnetic, inelastic hadronic and nuclear interactions, which are detailed in the following [28, 5].

- **Nuclear fragmentation**

For very high energy primary particles above the separation energy E_s according to

$$E_s \simeq E_b(N, Z) - E_b(N_F, Z_F) - E_b(N - N_F, N - Z_F) - \frac{Z_F(Z - Z_F)}{(A - F)^{1/3}} \quad (1.21)$$

it is possible to fragment a nucleus. The first three terms describe the binding energies of the nuclei involved, the last term accounts for the Coulomb barrier. Especially for high-Z nuclei, more effects become relevant and one has to rely on empirical descriptions of the problem.

- **Inelastic hadronic interaction**

For high energies, quantum chromo dynamics describe the interactions of particles sufficiently well, while for energies below 1 TeV one has to rely on phenomenological descriptions. These interactions are prominent in the production of secondary particles like pions or kaons.

- **Electromagnetic interaction**

The electromagnetic component is the main interaction channel for lighter, charged

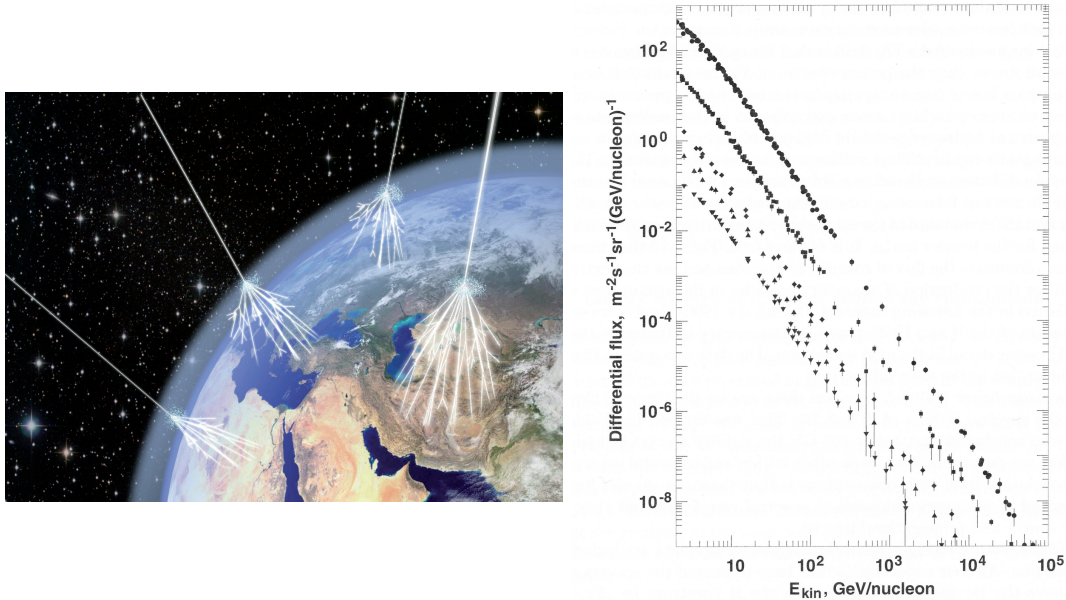


Figure 1.5.: Left, an artistic impression of various cosmic rays hitting the atmosphere [29]. Right, the measured composition for cosmic nuclei is shown: The lightest particle, the proton exhibits the largest flux, while heavier ions are suppressed by several orders of magnitude. Figure from [28].

particles like muons or electrons, but also for photons. As the propagation of muons is especially important in the context of this thesis, these interactions will be described in some more detail.

– Coulomb scattering

If one charged particle passes another, it is deflected by its electric field by the angle θ according to

$$\tan \frac{\theta}{2} = \frac{zZe^2}{Mv^2b} \quad (1.22)$$

where z and Z are the charge numbers of scatterer and scattering particle, e is the elementary charge, M the reduced mass and b the impact parameter.

– Ionization losses

Through ionization and excitation of molecules, incident particles loose energy in a medium, in this case the atmosphere, according to

$$\frac{dE}{dx} = -\frac{N_A Z}{A} \frac{2\pi (ze^2)^2}{M\nu^2} \left[\ln \frac{2Mv^2\gamma^2}{W} I^2 - 2\beta^2 \right], \quad (1.23)$$

where Z is the atomic and A the mass number of the medium, and I is the average ionization potential. N_a denotes Avogadro's number, ze the particle charge, v its velocity and M its mass. Furthermore, $\beta = v/c$, $\gamma = 1/\sqrt{1 - \beta^2}$ and W is the maximum energy deposit [30].

This effect is used for muon detection in the KATRIN experiment, see chapter 3.

– Compton scattering and inverse compton effect

Compton scattering is the photonic equivalent to ionization by charged particles. In the process, a photon interacts with bound electrons and excites or ionizes the corresponding atom. Doing so, the photon looses energy and is shifted towards longer wavelengths.

The inverse Compton effect, as the name suggests, describes a photon gaining energy from an atomic shell electron.

- **Bremsstrahlung and synchrotron radiation**

When charged particles are deflected by electric fields, photons are emitted and the particle loses energy. The same is applicable to magnetic fields, where the effect is called synchrotron radiation and a time dependent energy loss occurs. The total energy loss for electric fields can be described by

$$\frac{dE}{dx} = \frac{4N_A Z^2}{A} \alpha r_e^2 E \ln(183Z^{1/3}) = \frac{E}{X_0}, \quad (1.24)$$

where the radiation length X_0 has been introduced to describe the average matter necessary for a particular energy loss.

- **Electron-positron creation**

A photon of sufficient energy (>1 MeV) can create an electron-positron pair when scattering at an atomic nucleus. With higher energies, other particles can be created considering the known conservation laws. This process can be seen as the inverse bremsstrahlung, assuming the outgoing anti-particle to be its time inverted particle. The energy loss can be described similarly and scales linearly with the energy of the incident particle.

- **Cherenkov radiation**

Much smaller amounts of energy are emitted as Cherenkov light. The process is particularly important though due to its easily detectable particle indicators. Cherenkov radiation occurs when particles move through matter at speeds above the phase velocity of light c/n for a refractive index n . As the atmospheric refractive index is only slightly above 1, particles need to be super-relativistic to emit Cherenkov light.

After cascading mostly through multiple intermediate particles, at sea level about 80 % of the cosmic particles are muons. These are super-relativistic due to their small masses and, at the same time, high energies. Even at these high speeds, the muons' average decay time of about 2.2 μ s [31] is too small for many muons to reach the earth's surface from our reference frame's point of view. In the average production height of 2 km [32], the non relativistic time of flight for a particle traveling at 90% of the speed of light would be

$$t_{class} = 2 \text{ km} / 0.9 \cdot c = 7.4 \mu\text{s} \quad (1.25)$$

The fact that nevertheless, a rather large muon flux is observed at the Earth is explained by time dilation effects of special relativity:

$$t_{rel} = t_{class} / \sqrt{1 - 0.9^2} \quad (1.26)$$

which, from our reference frame, prolongs the muon lifetime by about a factor 5, thereby allowing muons to reach the Earth's surface from heights of 3 km. Most muons have even higher energies, enabling them to reach surface from greater heights and with a large angular distribution. These muons can cause background events via emission of secondary electrons in the stainless steel vessel of the KATRIN main spectrometer and hence pose a particular challenge. Shielding against muons is difficult as it requires thick layers of dense matter due to the muons high energies and the relatively low energy deposition in matter. The fluctuations in the energy deposition of a muon in matter can be described by the Landau distribution that is parametrized as follows [5]:

$$L(E) = \frac{1}{2\pi} \exp \left\{ -\frac{1}{2} \left(E - \hat{E} + \exp(-(E - \hat{E})) \right) \right\}. \quad (1.27)$$

Here, \hat{E} is the most probable energy deposition value. The analytic distribution is shown in figure 1.6. It will be shown in section 3.5, that this characteristic distribution can be reproduced by the muon detector system implemented in the course of this thesis.

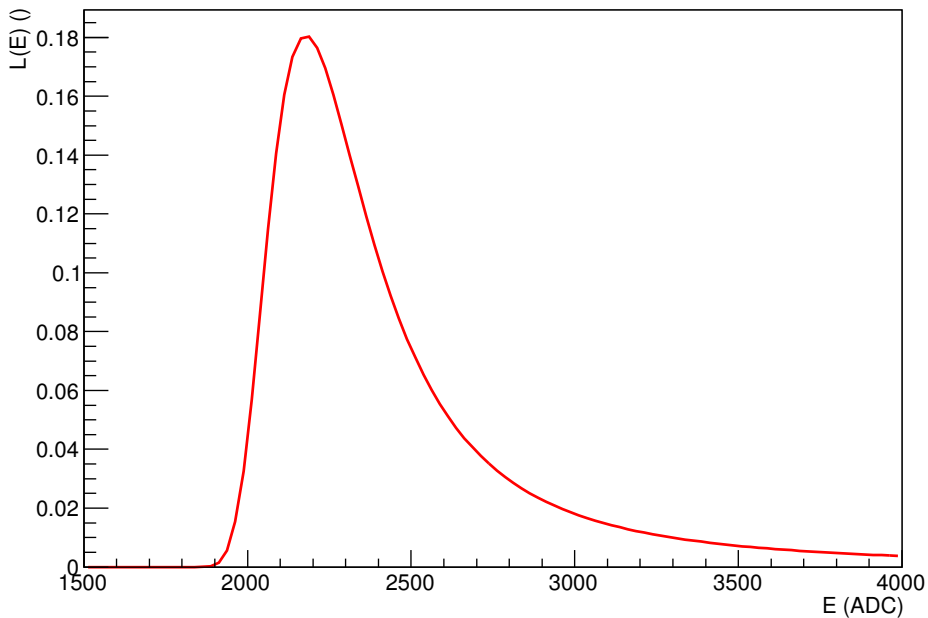


Figure 1.6.: Analyticcal Landau distribution as implemented in the ROOT software. \hat{E} was set to 1200.

2. KATRIN experiment

The KATRIN experiment is currently being assembled at the Karlsruhe Institute of Technology to determine the effective mass of the electron anti-neutrino with a sensitivity of $200 \text{ meV}/c^2$ at 90 % C.L., excelling the predecessor experiments at Mainz and Troisk by a factor of 10. Major challenges of the project are the required ultra high vacuum, the exact knowledge of all magnetic and electric fields as well as external influences on those, the required high luminosity of the tritium source and the classification and reduction of background sources. This chapter will give an overview of the measurement principle of KATRIN (section 2.1) and the experimental setup (section 2.2).

2.1. Measurement principle

The general idea of the KATRIN experiment is a high-precision measurement of the energy of electrons from tritium decay



and a comparison to the spectral shape as obtained for a massless neutrino [33]. As the decay energy is distributed between the rest mass of the decay products and the kinetic energies the neutrino and the electron respectively, the decay electrons show a continuous spectrum. The difference between the spectral shape calculated with Standard Model presumptions and the measured shape are used to determine the neutrino mass. As all three mass eigenstates contribute to the electron neutrino mass in any scenario (see figure 1.4), the difference will be a superposition of these. The kinks occurring for each individual mass eigenstate can not be resolved with the KATRIN spectrometer as the energy resolution is larger than the mass differences. As all three flavors contribute to the electron neutrino mass, what will be measured is the incoherent sum will be measured as described in section 1.3.

One of the major challenges is the exact determination of the electron energy with an energy resolution of 0.93 eV , required to achieve the design sensitivity [34]. While each component of the experimental setup by itself already exhausts the current technological limits, they also have to work in combination with each other. In the context of this thesis, it is important to notice that stringent requirements concerning the background contribution of each component have to be met to achieve the design goal.

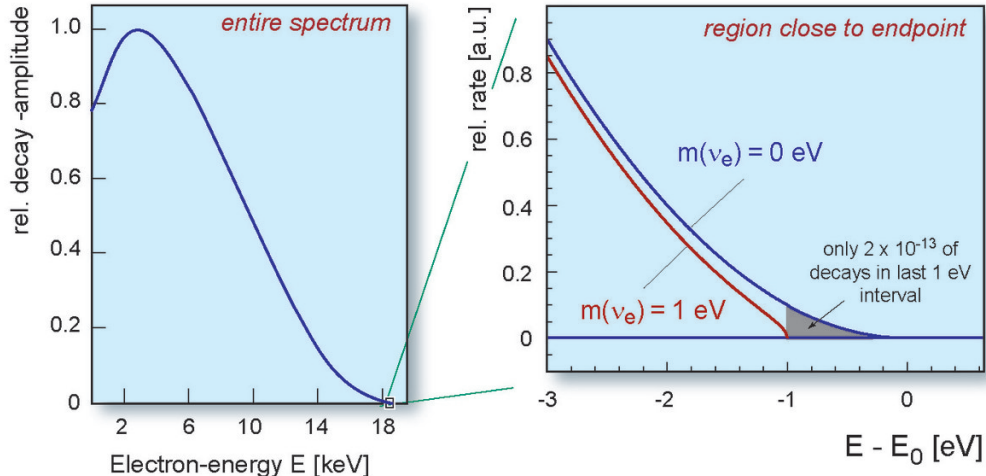


Figure 2.1.: Schematic energy spectrum for electrons from tritium beta decay. On the left, the entire spectrum peaking around 5 keV - can be seen. On the right, a zoom-in to the endpoint region shows the calculated spectra for a massless neutrino and a massive neutrino with $m=1\text{ eV}$ neutrino. As described in the graph, rates in this region are extremely low and sophisticated analysis tools have to be applied.

2.1.1. MAC-E Filter

To measure the energy of electrically charged decay electrons at high precision, an electrostatic filter is best suited. As the electrons are emitted isotropically, they will have momentum components both parallel and perpendicular to the source-detector axis (defined as the z-axis). To determine the total electron energy, the momentum direction needs to be well defined. In case of an electrostatic filter, only the parallel component can be analyzed. At the same time, a high luminosity is a major requirement for good statistics for the KATRIN experiment. To satisfy all these requirements, several techniques are combined in the MAC-E filter, the magnetic adiabatic collimation with electrostatic filter [36].

Magnetic field lines connect the source and the detector. Electrons from tritium decays are guided from the source to the detector, thereby performing cyclotron orbits around the magnetic field lines. Consequently, a maximal solid acceptance angle of 2π can be achieved, resulting in a high luminosity at the detector.

Adiabatic electron motion in the magnetic field is achieved if the magnetic field change is small within each cyclotron orbit. In this case, the magnetic momentum μ , which is correlated to E_{\perp} , the energy perpendicular to the magnetic field B , remains constant

$$\mu = \frac{E_{\perp}}{B} = \text{const} \propto \frac{p_{\perp}^2}{B}. \quad (2.2)$$

Collimation in a MAC-E filter is based on the above adiabacity. The magnetic field strength drops by four orders of magnitude from B_{max} at the superconducting solenoids to B_{min} in the analyzing plane (see figure 2.2). Following equation 2.2, this means that the energy perpendicular to the magnetic field has to drop accordingly for μ to remain constant. This leads to a parallelization of momentum vector and B-field direction.

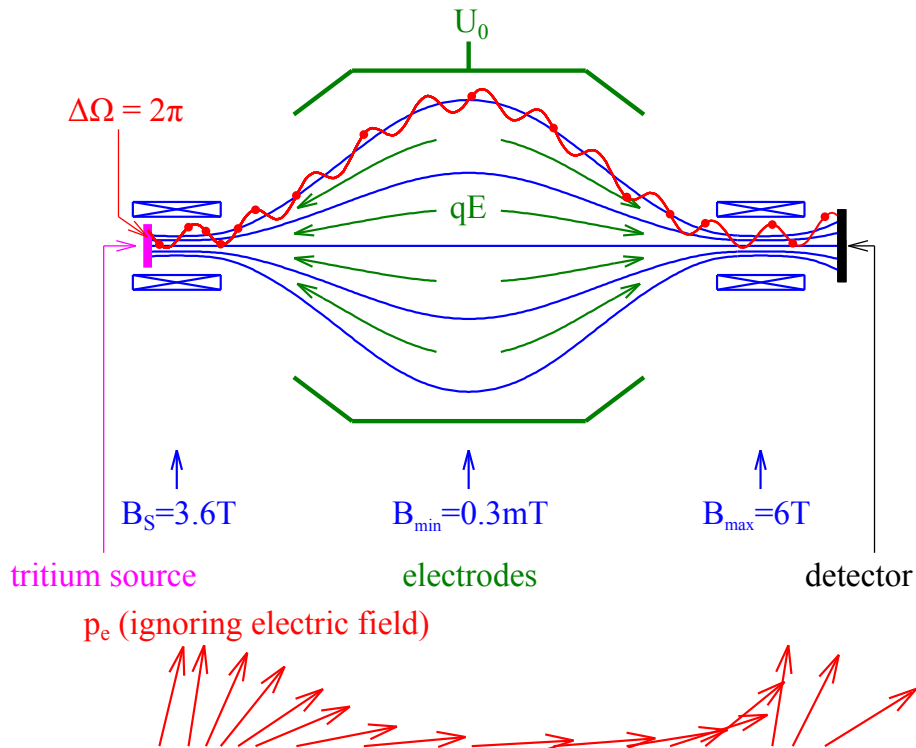


Figure 2.2.: Principle of a MAC E filter. In the upper part, magnetic field lines are plotted in blue together with the field values at the source (3.6 T) and inside the pinch solenoid (6 T). The accepted solid angle and an exemplary particle path are shown in red. The analyzing plane is defined by the area of minimum magnetic fields B_{\min} . Below, the momentum of an electron with a large starting angle with respect to the magnetic field lines is shown. It tips over as the field weakens. Meanwhile (not shown in this graph), the vessel voltage U_0 analyses the energy parallel to the electric field allowing only electrons with large enough energies to pass on to the detector [35].

Electrostatic filtering occurs exactly at the point of minimal energies E_{\perp} in the analyzing plane. Here, the momentum vector is aligned mostly parallel to the magnetic field $E_{||}$, which determines the parallel energy component. Setting the electrostatic filter to a fixed voltage U now reflects electrons with $E_{||} < U \cdot e$.

As electrons are emitted isotropically in the source, they exhibit an energy $E_{\perp} \neq 0$. Therefore, electrons in the analyzing plane have remaining energy E_{\perp} , which limits the filter resolution

$$\mu_{low} = \frac{E_{\perp_{min}}}{B_{min}} = \frac{E_{\perp_{max}}}{B_{max}} = \mu_{high} = \mu, \quad (2.3)$$

the relative sharpness is given by the maximum transversal energy $E_{\perp_{max}}$ that is still accepted by the filter:

$$\Delta E = E_{\perp_{max}} = E_0 \frac{B_{min}}{B_{max}} \quad (2.4)$$

Only in the unachievable case of $B = 0$ in the analysing plane, the momentum would be exactly parallel to the field and the resolution would not be limited. The main spectrometer reaches a resolution of 0.93 eV (see section 2.2.4 for more details). After passing the analysing plane, the electrons are reaccelerated by the electric field and guided and focused onto a detector by the magnetic field. To additionally dismiss electrons with large starting angles, the source field strengths are chosen to be smaller than the maximum field strength inside the pinch solenoid. This measure ensures that electrons with long paths that are consequently more likely to scatter off tritium molecules in the source will not be analyzed using the effect of magnetic mirroring [37]. With the chosen settings, this results in an angular acceptance of 50.77°.

2.2. Experimental Setup

The KATRIN experiment consists of different sections all fulfilling their own important purpose in the whole setup. Located at one end is the windowless gaseous tritium source “WGTS”. Here, tritium decays isotropically, thereby emitting electrons. These are guided magnetically through the differential and cryogenic pumping sections, “DPS” and “CPS”, removing hydrogen ions and other residual gases in the process. At the same time, at the other end of the WGTS, the rear section scans the activity of the source. For the electrons on their way to the detector, the path continues through the two spectrometers acting as a energetic high pass filters to the focal plane detector, “FPD”, registering them.

During the whole procedure, the electrons from the decay may not undergo energy changes as the exact knowledge of their kinetic energy is essential to the experiment. Consequently the guiding needs to be adiabatic, which is guaranteed by spatially slowly changing and temporally constant magnetic fields.

Figure 2.3 shows a schematic overview of the whole experimental setup. It follows a more detailed description of the individual components.

2.2.1. WGTS and Rear Section

A gaseous tritium source, shown in figure 2.4, is utilized to generate tritium decay electrons. Advantages of the employed principle are the absence of solid state effects and a high luminosity [38]. In a solid, like tritium films, most decay electrons from inside the solid would interact with the solid itself, which leads to energy losses imitating a non-zero neutrino mass. Additionally, not only the surface facing the detector emits electrons at the required spectrum, but the electrons from the whole volume covered by the magnetic flux tube hitting the detector can be analyzed. Furthermore, the emission of this kind of source is very homogeneous. However, new challenges arise when using gas instead of solids.

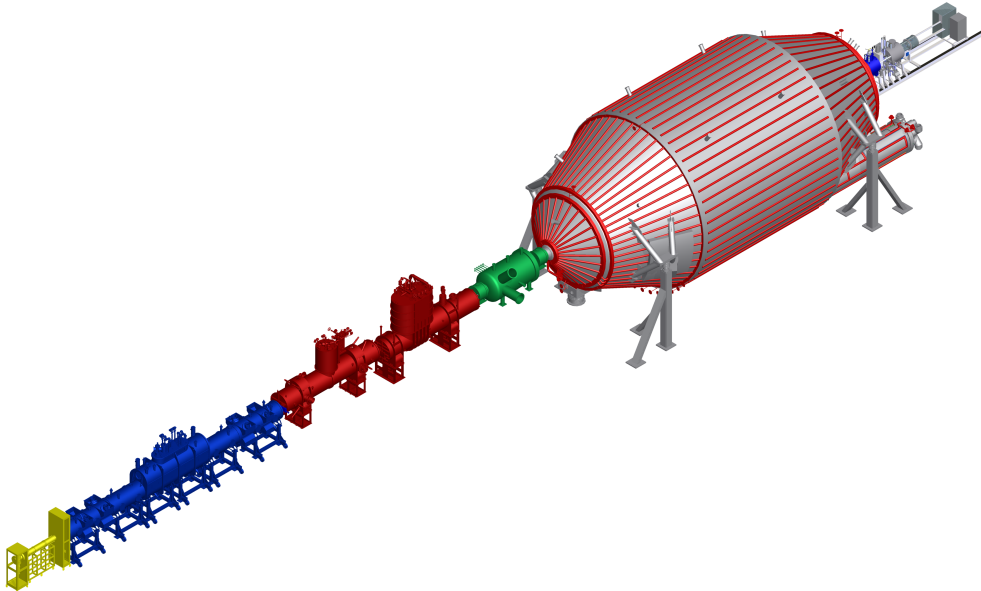


Figure 2.3.: The beam line of the KATRIN experiment with the different stages: Rear section (yellow) and WGTS (blue) on the very left, followed by the transport section (red) consisting of DPS and CPS. Energy analysis in pre- (green) and main spectrometer (grey-red) of the spectrometer section and electron detection at the detector section (grey-blue).

- The source temperature needs to be very stable with a maximum deviation of ± 0.03 K at 30 K, to guarantee a rate stability of ± 0.1 % for the decay electrons [39].
- The spectrometers further downstream require an ultra high vacuum - 10^{-11} mbar or better in case of the main spectrometer. With a tritium pressure is in the order of 10^{-3} mbar inside the windowless source the pressure must be reduced to a partial pressure of 10^{-19} mbar inside the main spectrometer without any physical barrier.
- The contribution of the individual hydrogen isotopologues of the gas has to be known precisely. For this purpose a laser-raman-system has been developed [40].
- All devices used in contact with tritium have to undergo excessive testing in tritium environment to guarantee failure safety under the harsh conditions.

2.2.2. Transport Section

Figure 2.5 shows the two sub-systems of the transport section, which are responsible for a reduction of the tritium flow by 12 orders of magnitude¹. In the differential pumping section (DPS), pressure is actively reduced by five orders of magnitude with the use of turbo molecular pumps. These as well need to be tested thoroughly to withstand the constant radiation by tritium decays [43] and the operation in strong magnetic fields. The tritium gas is then processed to be reused in the tritium cycle. Further downstream, the cryogenic pumping section (CPS) uses an ultra-cold inner surface of the tilted beam tube to freeze residual gas, while guiding the signal electrons around the chicanes by strong magnetic fields.

¹A suppression by an additional 2 orders of magnitude is achieved by active pumping at the front end of the WGTS.

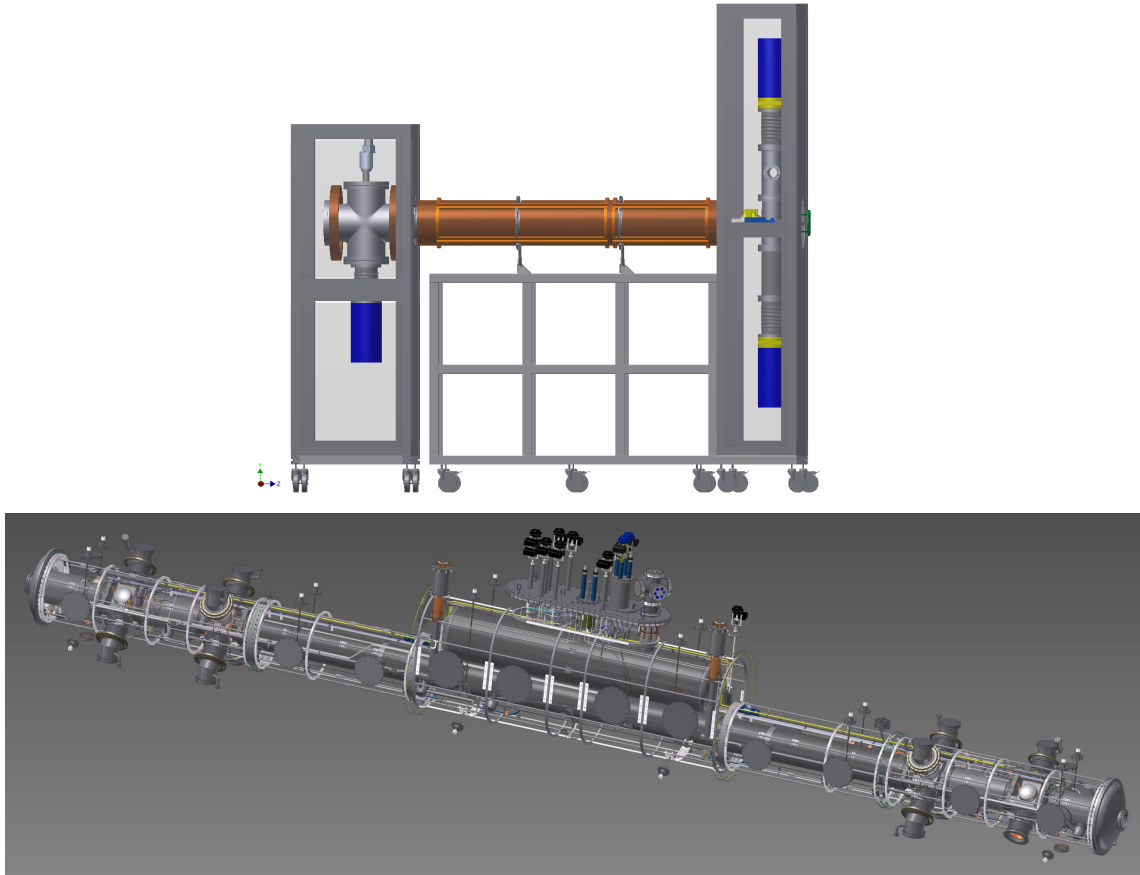


Figure 2.4.: Top: the rear section. In the model, there are two large attachments visible perpendicular to the beam direction. The right one is the e-gun for calibration purposes. The left one is the rear wall, which is responsible for monitoring of the source activity. Also visible are the gray second containment boxes required for redundancy in radiation security. Bottom: a model of the WGTS. The large number of pumping ports is clearly visible on the left and right end. Tritium is injected in the middle of the central tube from where it diffuses to both ends of the WGTS. Images from [41] and [42].

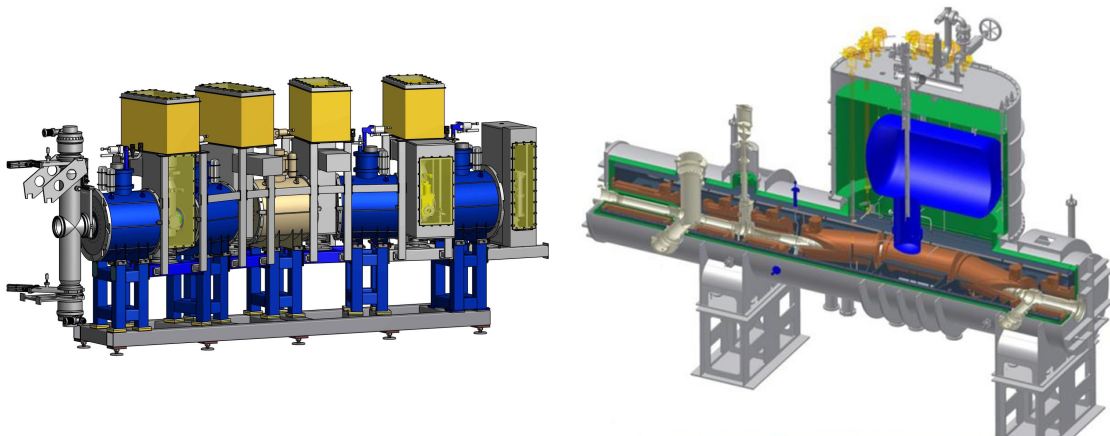


Figure 2.5.: The sub-systems of the transport section. Left: the DPS with four large pumping ports along the beam line between the superconducting magnets. All the ports are isolated against the surroundings (yellow boxes) to protect against potential radiation leaks [44]. Right: the CPS with its coolable wall structure to capture the remaining tritium-molecules [45].

2.2.3. Pre-Spectrometer

The pre-spectrometer was built to reduce the electron flux to the main spectrometer by up to 7 orders of magnitude [46]. It works according to the MAC-E filter principle from chapter 2.1.1. With a moderate, but sufficient, energy resolution of about 60 eV, its purpose is to cut off the spectrum below energies of 18.4 keV. Electrons above that limit will pass this pre-filter and can be further analyzed in the main spectrometer. Here, it is important that the momentum is restored after analysis which requires for a symmetric setup. To shield against externally induced electrons, the pre-spectrometer has a single layer of wires as a inner electrode. It can be set to negative voltages in comparison to the pre-spectrometer hull which then reflects electrons with energies up to U_e .

2.2.4. Main Spectrometer

The largest component in the experimental setup is the main spectrometer. With a diameter of 10 m and a length of over 23 m, its total volume amounts to about 1400 m³ that need to be evacuated to extremely high vacuum of $< 10^{-11}$ mbar. The main spectrometer, as the pre spectrometer, makes use of the MAC-E filtering technique described in section 2.1.1. To do so, it features a uniquely designed double-layer inner wire electrode and a sophisticated high voltage system [47]. A precision voltage divider was constructed to be able to read out the high voltage applied to the vessel with the highest precision voltmeters, which operate in the range of 10 V [48]. Additionally, the voltage is fed to the monitor spectrometer, detailed in section 2.2.5 to monitor its long term stability.

One of the major background sources are secondary electrons emitted from the spectrometer surface. The magnetic field in the main spectrometer acts as an intrinsic shield against this background component. However, due to imperfections in the axial symmetry of the magnetic field, some electrons can penetrate the sensitive flux tube volume, increasing the background beyond the required value. The vessel is equipped with two layers of electrodes on a comb-like structure. This setup reduces the number of secondary electrons from the spectrometer walls entering the flux tube's volume [49]. The inner wire layer features thinner wires and consequently shields the spectrometer volume from the outer layer with thicker wires as cosmic rays may unleash electrons there as well. The main spectrometer vessel is set to high voltage, which can be varied in the region below the endpoint at 18.6 kV. It constitutes the MAC-E filter from 2.1.1. The wire electrodes float on that voltage with an additional potential offset to shield against the above mentioned electron background.

2.2.5. Monitor spectrometer

The third MAC-E filter at KATRIN is the slightly modified Mainz spectrometer. It has been transported to Karlsruhe to work as a high voltage monitoring device. Here, electrons from ^{83m}Kr decays are detected and analyzed. The fact that the energy from these decays does not change over time (neglecting changes in the source material) can be used to detect shifts in the voltage of the MAC-E filter. For that purpose, the monitor spectrometer constantly measures transmission functions of this particular L-32 line. The monitor spectrometer additionally features two scintillation modules for muon detection that were used for a first inspection of muon induced background.

2.2.6. Focal Plane Detector System

The detector is located at the very north of the experiment. It consists of a silicon wafer whose back-side is divided into 148 pixels, as shown in figure 2.8, attached to the readout electronics by pin diode connectors. The pattern is dartboard-like where multiple pixels

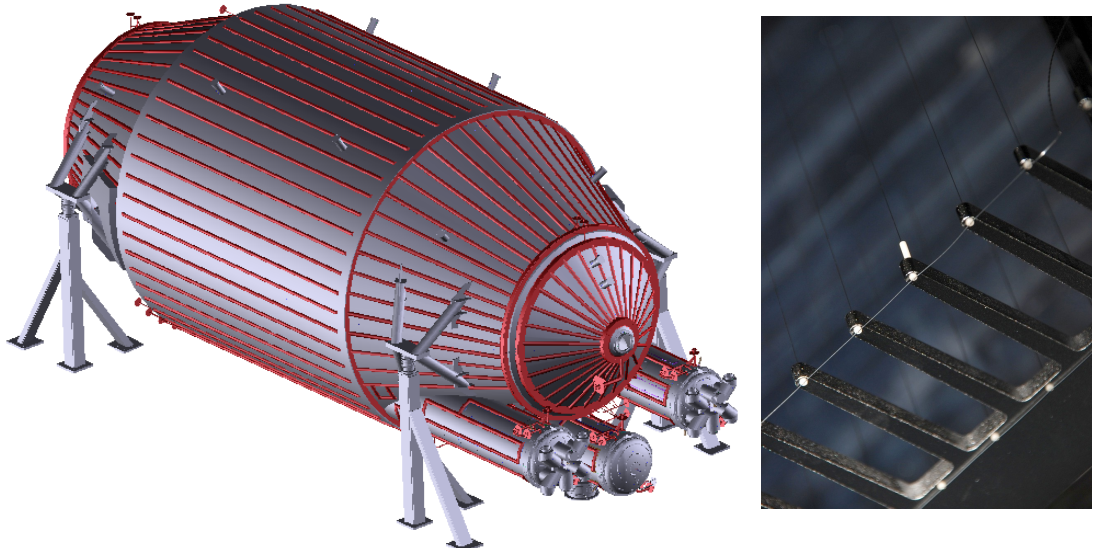


Figure 2.6.: Left: the main spectrometer of the KATRIN experiment [50]. It is divided into a central part with cylindric shape to which the flat cones, and furthermore the steep cones, are attached. Also visible in this image are the 3 large pump ports on the lower right and the three-legged holding structures. On the right an image of the comb structure of the inner electrodes with both layers of wires is visible. The white structures on both top and bottom of the combs are required to insulate the wires from the combs, which are held on different potentials [51].

with the same distance to the center form rings. Every pixel has the same surface area, making rates more easily comparable - given that the magnetic flux through the wafer is sufficiently homogeneous. The detector system is roughly divided into two chambers: one connected to the ultra high vacuum of the main spectrometer and one with a lower grade vacuum on the detector's readout side.

For background reduction, the detector system features both a passive shielding and an active veto system read out by the same data crate as the detector itself. It allows to discriminate against externally induced detector events. Due to the high magnetic fields from the detector- and pinch magnet, semiconductor readout electronics had to be used instead of conventional photomultiplier tubes. As it may be necessary to investigate electrons with energies below the detector threshold, especially for background investigations, a post acceleration electrode has been installed - also visible in 2.7- that can add to the electrons' energies through an electric field of known strength.

2.2.7. Solenoids, LFCS and EMCS system

To achieve magnetic guidance as explained in chapter 2.1, a sophisticated system of superconducting solenoids, the low field correction system LFCS and the earth magnetic field compensation system EMCS have been installed [53]. These make sure that the path of flight is kept away from the wall and can be considered adiabatic, that penning traps are avoided as far as possible, that the earth magnetic field is compensated for and, most importantly, that the field drop towards the analyzing plane is of the order of 10^{-4} such that the desired spectrometer resolution is achieved.

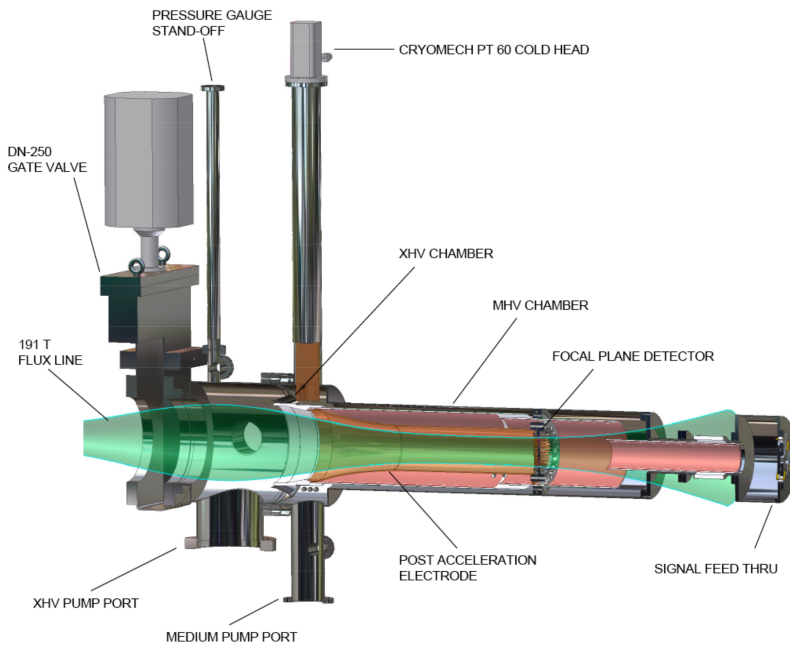


Figure 2.7.: The focal plane detector system including the flux tube (green). The different grade vacuum sections can be identified: extremely high vacuum (XHV) and medium high vacuum (MHV). The post acceleration electrode is visible to the left of the bronze colored actual detector and its signal feed trough on the very right. Multiple flanges and connectors are shown. Not included in this picture are the calibration source holders [52].



Figure 2.8.: The detector wafer as installed in the FPD system. Note the “dartboard pattern” with the four pixel bullseye in the center. This is the detectors back side to which the electronics are attached. The front is plaid making for high detection efficiencies.

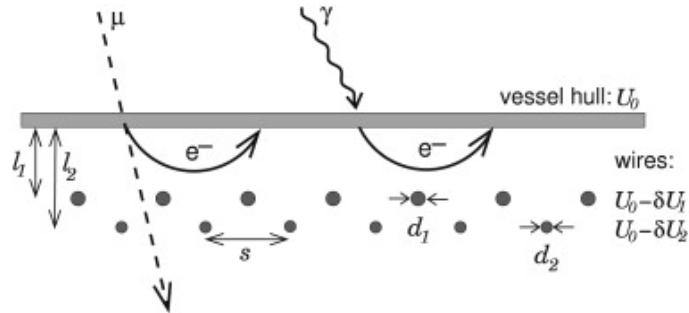


Figure 2.9.: A graph of the wire electrodes installed inside the main spectrometer. Both layers of electrodes with different distances to the spectrometer wall are visible, the inner being smaller in diameter than the outer one. High energy photons can induce electrons, though the main component is generated by cosmic muons [49].

2.2.8. Background sources

The KATRIN experiment has a stringent background requirement of less than 10^{-2} counts per second (cps). Different sources contribute to the background of electrons arriving at the detector. Stored electrons are expected to be the largest source of detector background [54]. Penning traps cause electrons with energies in a certain range to be caught in a potential cup. Discharges of those traps due to scattering processes with either residual gas or due to excessive filling of the trap can cause high-rate events at the detector. Such discharges were observed to produce rates on the order of 100 kcps, which can even harm the detector. Stored electrons can be created by external sources or originate from within the spectrometer. One large background source is radon, a noble gas enabling it to move freely inside the vessel. Radon alpha decays produce high energy shake-off-, conversion- and Auger electrons which cool down via ionization of residual gas molecules. The thereby produced secondary electrons can be guided to the detector from inside the flux tube [55, 56]. Another large background source that was already discussed above are cosmic rays interacting with the vessel hull thereby producing electrons. This background is reduced mainly by two factors, the symmetry of the magnetic field and the wire electrodes shielding the flux tube up to a certain threshold energy. If the fields, both electric and magnetic, were perfectly axially symmetric, only particles generated within the flux tube would be guided towards the detector. But through inhomogeneities and alignment errors, electrons may enter the flux tube through $E \times B$ drifts even if generated externally, e.g. at the spectrometer wall. To suppress this background component, the wire electrodes, were installed. They shield the flux tube against electrons with energies up to $E_e = eU_{wire}$ depending on the wire electrodes voltage U_{wire} .

3. Muon detection system

The need for low background rates at the FPD requires a good understanding of the background sources. Despite magnetic reflection and wire electrodes described in section 2.2.8, cosmic ray and particularly cosmic muon induced background may be an issue for the KATRIN experiment. To gather and assess muon related data, a muon detection system has been designed and set up at both the monitor spectrometer and the main spectrometer. Both are built on the same principle. Scintillator panels (section 3.3) are permeated by muons causing photon emissions in the material. The photons are detected by photomultipliers (section 3.4) and converted to measurable electrical signals. Readout is handled by a data acquisition crate “DAQ” (sec. 3.1) that is controlled via the Object-oriented Real-time Control and Acquisition[57] (ORCA) software on a Mac computer (section 3.2). While the monitor spectrometer is equipped with only two rather small modules of $A \approx 0.5 \text{ m}^2$, at the larger main spectrometer, 8 modules have been installed at different positions in three groups (figure 3.1). Their individual areas are about 2 m^2 . They enable the coverage of different regions of the vessel (see figure 3.1). To analyze different areas of the main spectrometer, the muon modules are mounted on three independently movable trolleys and can be individually selected. On the trolleys are not only the modules themselves, but also high voltage supplies and all readout electronics for a maximum of flexibility (figure 3.2). The modules have been connected to three FLT¹ cards of the DAQ and the high voltage supplies. For the connection scheme, see table B.2 in the appendix.

All connections from modules to DAQ are made from coaxial cables of equal length. As the DAQ is located on the east side of the main spectrometer, cable lengths of 30 m are necessary for readout of the west side modules. As timing is important and at that length, the cables introduce delays of $\approx 15 \text{ ns}$ at 50 ns time bins in the DAQ software, the error introduced by greatly differing lengths would be too large. Equal lengths ensure comparable timestamps which are assigned only after the analogue signals arrive at the DAQ. High voltage is provided by two supplies, one on each side of the main hall. The settings used for the supplies are shown in table B.1 in the appendix, figure 3.6 shows the front panel of the east side device. All devices of the muon detection system are connected to two multi-plugs that are both over-current protected and feature mains filters. These multi-plugs have been modified (figure 3.5) to connect to a ground other than the one of the power outlet. To ensure a common potential for all devices and the surrounding appliances this connection was made to the trough below the main vessel.

¹First level trigger

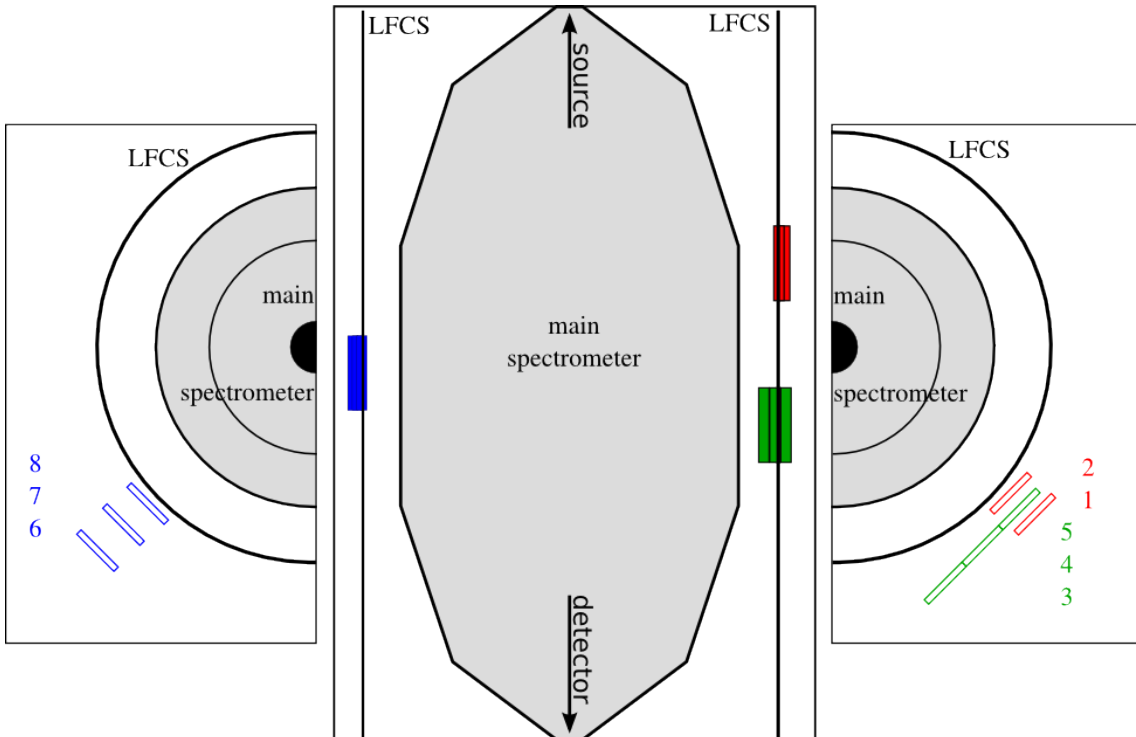


Figure 3.1.: The muon detection system as realized at the main spectrometer. In (blue), the east side modules shown in figure 3.2. On the west side, modules 1 and 2 (red, figure 6.13) and modules 3 to 5 (green, figure 3.3) are located. Note the closeness to the LFCS system in the references figures.

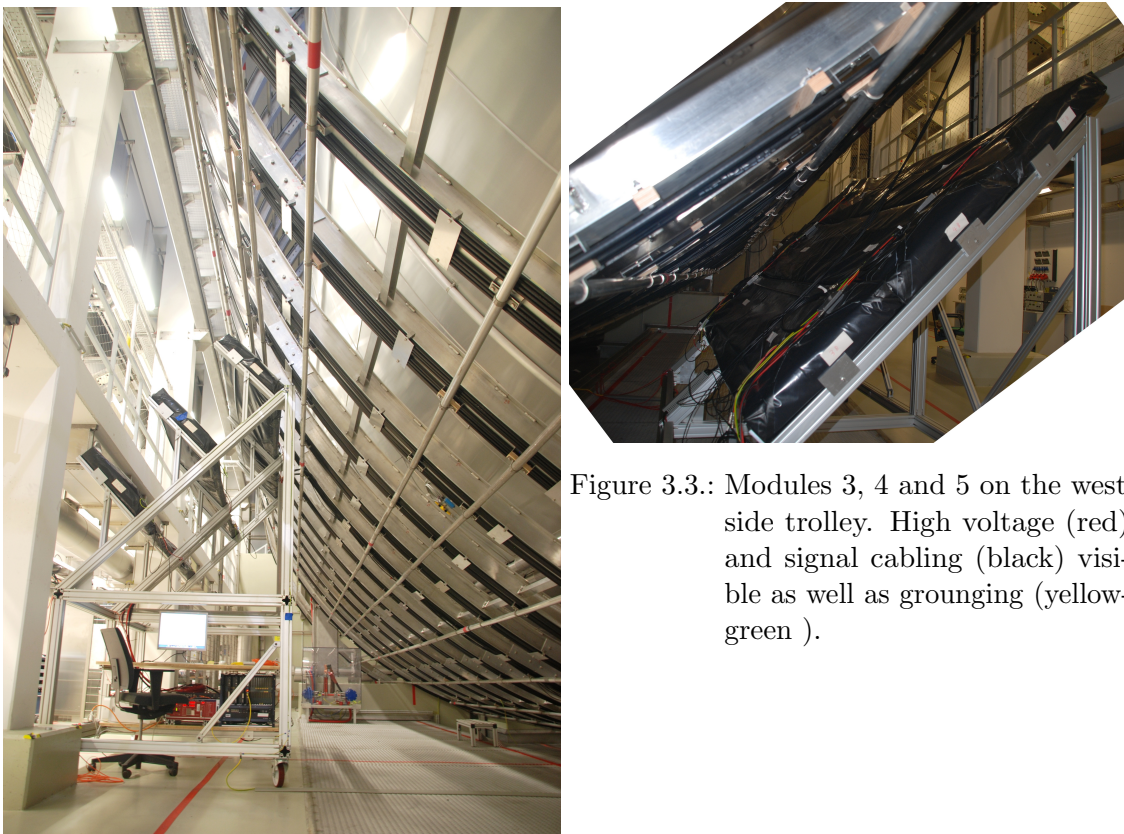


Figure 3.2.: Modules 6, 7 and 8 on the east side trolley. On the boards inside the trolley the DAQ system and the eastern high voltage-supply.



Figure 3.4.: The muon modules at the monitor spectrometer above the vessel. The area is smaller while the distance between the two is comparably large.

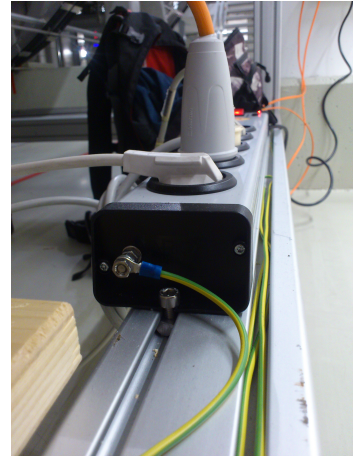


Figure 3.5.: One of the two multiplugs. In the foreground, the custom made ground outlet is visible that connects to the same potential the modules are connected to.

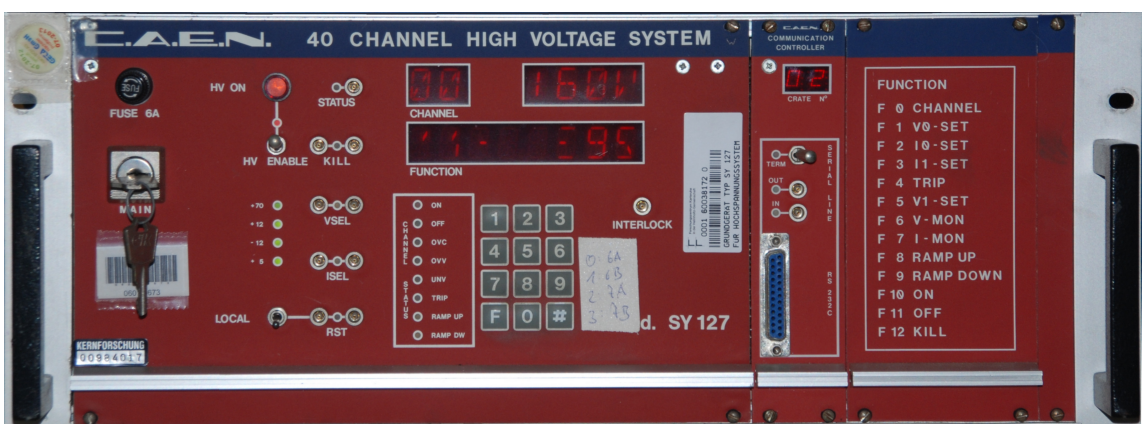


Figure 3.6.: One of the two high voltage supplies used to power the muon modules photomultipliers. On the right side, the codes sequence table for setup is visible, see table B.1 for the settings used.

The high voltage supplies first thought to be used for the main spectrometer modules but not available in large enough quantities were installed at the monitor spectrometer. Furthermore, one more FLT card (section 3.1.1) is used to read out the two monitor spectrometer modules. Channel configuration is the same as for modules one and two at the main spectrometer.

3.1. Data aquisition crate

The DAQ is the central part of event recording and by that the interface between hardware muon modules and software based ORCA machine. It was originally developed for the Pierre-Auger-Observatory, but is now used in many different experiments due to its large flexibility. There are two types of DAQs used in KATRIN: the standard model used at the main spectrometer and the mini DAQ used at the monitor spectrometer. The latter features only 4 FLT plus one SLT slot which is sufficient for the monitor spectrometer, but not for the main detector. Here, the larger model with up to 20 FLT cards is used. Both models feature first and second level trigger cards, the former with specific KATRIN firmware in version 4 that are described in detail in sections 3.1.1 and 3.1.2. The DAQ can be connected to and controlled by the ORCA software 3.2.

3.1.1. First level trigger cards

The first level trigger cards (FLTs) directly receive a signal output from the photomultiplier tubes via coaxial cables. An anti-aliasing filter with a sampling frequency of 10×10^{10} Hz enables the FLTs to find signal pulses of the length of 30 ns which the muon modules generate. Choosing the right filter settings is crucial for the detection efficiency (see section 6.1). The FLT cards do a simple part of data analysis to reduce data flow. By sending only events which occur simultaneously on both sides of any module, the rate reduces by a factor four to around 250 cps. The FLT cards are made up of a large main card and a smaller connector card entered at the back side. Every card has 24 channels. These are divided into three groups if the card is operated in veto mode. Then, every group consists of one sum channel that can be read out in coincidence with any other or multiple other channels from the group. In case of the muon modules, 1-fold coincidence is used; one side of each module is connected used as the sum channel, the other is assigned to an arbitrary channel in the respective group. Every event recorded features not only the timing information and the ADC-value, but also the card slot and the channel it was recorded on. That binds the event to a module.

3.1.2. Second level trigger cards

Only one second level trigger card is installed in each DAQ. All signals remaining after SLT analysis are stacked here and passed on to the the ORCA machine. Networking runs directly through the SLT card's front panel. The connection is established via ORCA's SLT dialogue. Other connections, such as USB, a display port, and especially the CAT 5 connectors for synchronization to a external clock (see section 6.7) can be attached to the back panel card.

3.2. Orca control

The ORCA software is the central software for data acquisition. It is able to control the different devices via various kinds of interfaces, with Ethernet connections being the most common. The ORCA software runs on iOS. It can be controlled locally as well as via screen share from the KATRIN control room. As the system is located in the restricted area for live high voltage on the vessel, this enables changes on the muon system during

high voltage measurements. The different objects used for the muon detection system are described in the following. For a more complete description, see [58].

- Run Control

All data taking is started and stopped through run control. Runs are the basic element of data storage. A run is created by the run control object every time data is recorded. A run can contain a number of subruns (there is at least one) that will in turn contain data classes such as “KaLi::KLVetoEvent”, the most used event class in case of the muon modules. On-line and off-line runs can be taken. The latter are not stored or uploaded for analysis but are available for direct reviewing. They are discarded as soon as another run is started.

- File handling

All online runs created are first saved to the local disc as ORCA specific “.orca” files. They are then uploaded to servers of the IPE, another institute at KIT CN. Scripts on the servers convert the files to the .root format. Using the KaLi software developed and sustained at KIT CN, data can be accessed and analyzed from anywhere in the world with an Internet connection.

- Software Gains and Thresholds

All data registered by the DAQ is amplified and cut off below certain software set values. These can be entered for the individual channels of each card separately. Gains can vary from 0 to 4095 (12 bit). Thresholds can be set to any value up to the maximum bin used. Depending on the filter settings, or more precisely with rising shaping length, bin values will be shifted towards higher absolute values (section 6.1). Scripting of the values is possible and reasonable for large numbers of readout channels such as at the FPD.

- Scripting

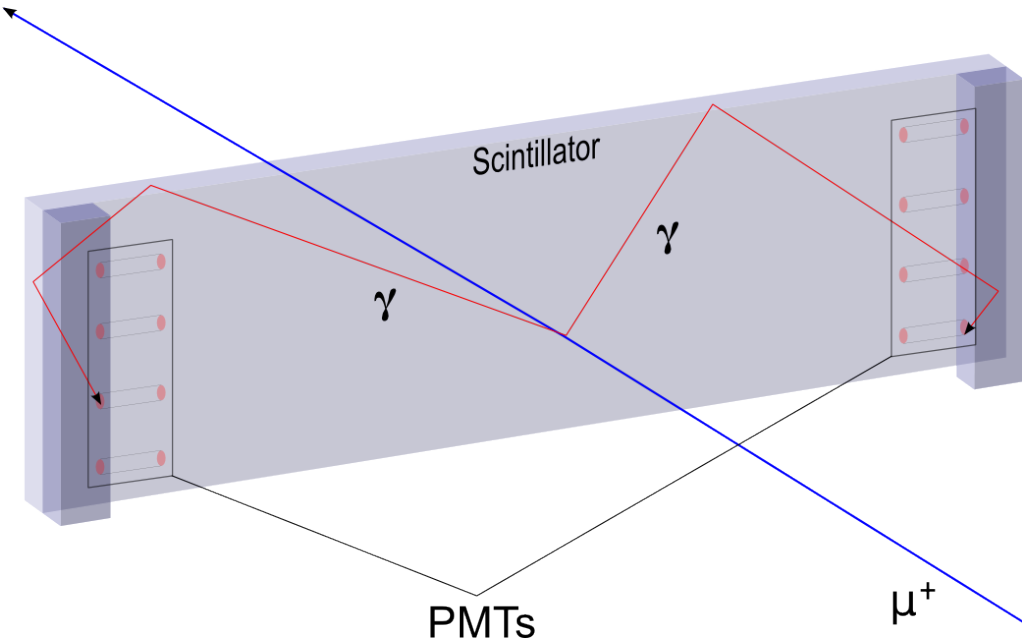
Scripts are useful for repetitive tasks or such that require short interaction only at certain points in time. One example for scripting is the ramping of LFCS (section 2.2.7) coils that has been used to check the rate dependence on the LFCS currents (section 6.3). In that case, the script sends the values to be set to the the so called ZEUS server, which passes them on to the controls of the power supplies. As this was supposed to be a stability measurement, every LFCS setting was kept constant for half an hour after which the script automatically changed the currents. Scripting makes it possible to take these 5 h runs without human interaction making it much more comfortable. Example code of the LFCS script can be found in appendix A. Of course, much more sophisticated tasks can be handled through scripts as well

- Orca Fit

The Orca Fit function uses external servers to fit data acquired by the DAQ in user defined ways. Besides linear or Gaussian fits, landau fitting (clause 1.7) can be used. The fit software was primarily used to get an impression of the figure of merit of the data. R^2 values are directly displayed which was used a first indicator to if the detected signals were muon induced.

3.3. Scintillator modules

The central part of the detection system are the eight scintillator modules. They are made of the synthetic material BC-412 which is utilized in applications requiring large area coverage [59]. The have been previously used at the KARMEN experiment [60]. Every scintillator cuboid is read out by two sets of four photomultiplier tubes located at the short ends of the scintillator material (section 3.4). Photons arriving at the short ends of the



module are guided to the photomultiplier tubes via non-scintillating material which, apart from the scintillating property, exhibits similar optical properties. To maximize detection efficiency, all other sides of the scintillator are covered in reflective foil. The whole system of scintillator and PMTs is wrapped in thick, black foil to prevent ambient light from being detected as signals. This kind of noise would show especially in the low energy areas, as has been discovered over a broken seal of one of the foils. High voltage, readout and grounding cabling is fed through the foil at two points.

Of the eight photomultiplier tubes per scintillator module installed, sets of four are read out via one FLT channel. The background of low energy events can be reduced significantly by recording only events occurring on both sides of the module at once. Only coincident signals should be recorded by the DAQ, though in some runs, quite a lot of single side signals occur. This seems to be a known bug in the ORCA software that could not be fixed yet. To account for the single side events for analysis every dataset was first analyzed by a search algorithm to filter them out (section 4.3).

3.4. Photomultipliers

Photomultipliers are based on two fundamental principles: photoemission and secondary emission. Each Photomultiplier tube is made of a layer of bialkali metal where photons from scintillation ionize the material via photoemission producing electrons with their initial energy reduced by the ionization energy:

$$E_{e^-} = E_{phot} - E_{ion}$$

. The electron is then accelerated and guided by the electric field from dynode to dynode (figure 3.7), cascading to more and more electrons through secondary emission, as each electron's energy rises by $e \cdot U_{acc}$ between each pair of dynodes [61]. This leads to an amplification of the electronic signal beyond a detectable threshold. Photomultipliers exhibit low noise and are very linear amplifiers which makes them feasible for single photon detection. Since the system is located close to the LFSC system, the PMTs have to work in magnetic fields, countermeasures had to be taken. A mu metal wrapping showed to provide enough shielding to make the detector work properly (section 6.3).

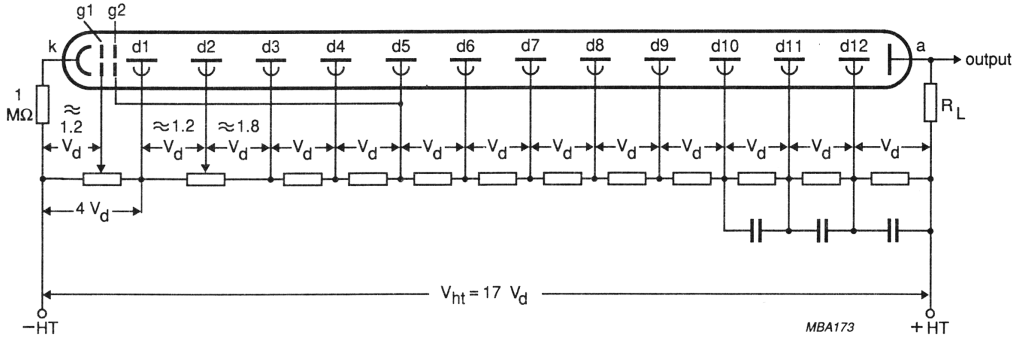


Fig. 2 Voltage divider type A.

Figure 3.7.: Schematic view of a photomultiplier tube including voltages and electric setup used in the muon detection system [61].

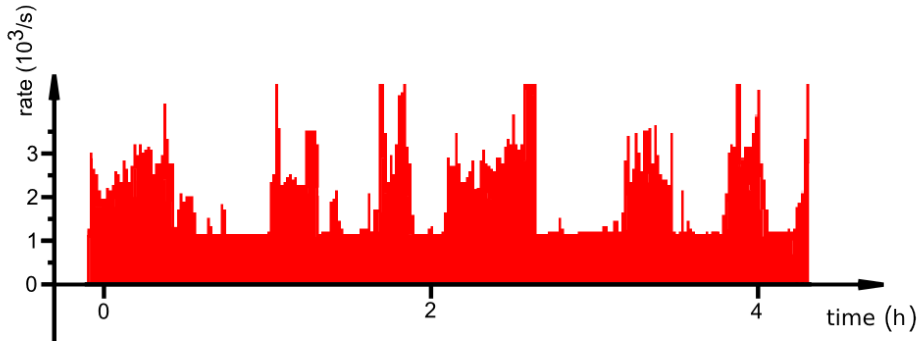


Figure 3.8.: Rate progression over the course of hours. The cumulative rate of all panels shows strong increases in certain intervals. In between it seems stable at around 1200 s^{-1} . Note that this data was taken before adaption of the acceleration voltages (see later in this section) which is why the single module shows rates of 150 s^{-1} only.

3.5. Gains, Thresholds and Acceleration Voltages

Due to manufacturing variances, the amplifications and threshold energies for electrons of every photomultiplier tube differ. To achieve the best possible event detection, the photomultipliers' acceleration voltages as well as the software gains and thresholds in ORCA had to be adjusted. The focus here was to obtain Landau peaks with equal height and width for all channels, as the rates throughout the modules can be considered equal over large time intervals. During some preliminary measurements, it became obvious that the panels' rates were peaking over short time intervals at some arbitrary frequency (figure 3.8). If the Landau distributions (section 1.7) were not identifiable due to prevalent electronic noise, the measurement was rendered useless (figure 3.9). That way, setting gains, thresholds and PMT voltages correctly was very difficult as one had to measure in a noise free period. Some kind of electronic pileup was suspected to cause this behaviour. As this issue did not occur for all the modules it was not noticed until later into the commissioning process.

As a countermeasure, potential equalization by a connection of the modules to the trough below the main spectrometer has been established. This showed to prevent the peaking. Thereby resolving the issue. Now, gains, thresholds and acceleration voltages could be set (figure 3.10).

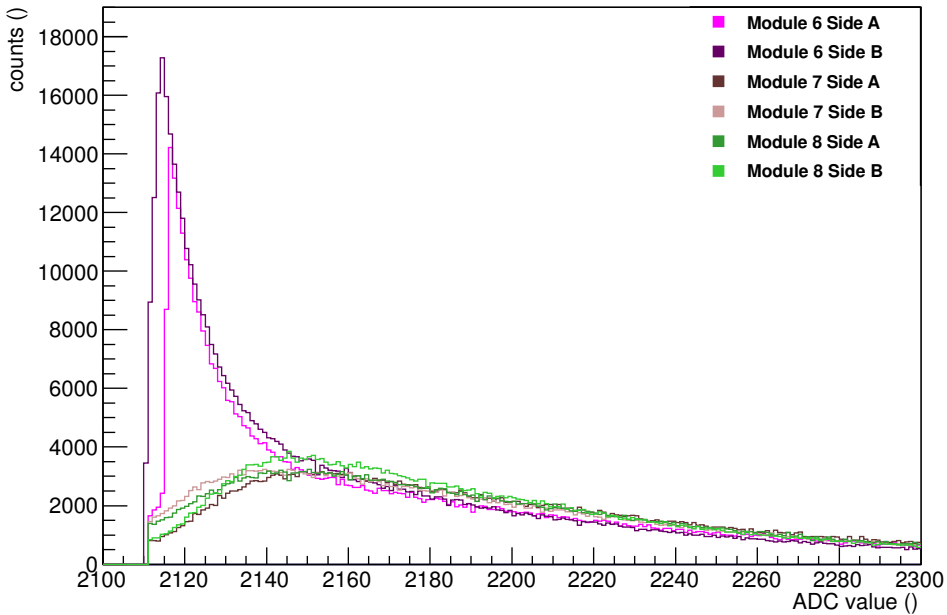


Figure 3.9.: Energy histogram of the six channels of modules 6 through 8. Displayed are counts over ADC-Value. Both sides of module 6 show a lot of noise at the low energy end of the histogram while the cards other channels are developing clear Landau peaks.

At first, the acceleration voltages were kept low to limit the signal peaks' heights to around 2 V. Carefully setting the mentioned parameters, one achieved the well aligned distributions from figure 3.10. A problem remaining at the time though was that the electronic noise set in pretty close to the peak position, only slightly shifted to lower energies. This made it not only very difficult to find suitable settings, but also meant that thresholds had to be set close to the peak bin loosing low energy events in the process (see figure 3.10). This showed in rates of around 150 cps that did not compare too well to literature values. The high energy region though could be well fit with landau distributions.

Later in the commissioning process, it turned out that the photomultiplier tubes had to be operated at acceleration voltages of 1.5 kV and above. This was found as the detection efficiencies for the modules, see section 6.5, were not as high as expected, assuming that the acceleration voltages set lower than denoted in the user manual leads to loss of data in the low energy range. Consequently, the acceleration voltages were raised to 1.5 kV except for two channels, those of modules 2B and 6A, that were even ramped to 1.6 kV to account for lower overall rates (section 6.6). Most of the tubes were limited to this minimal voltage to keep the signals' height as small as possible protecting the DAQ from taking damage. Following this procedure, the tubes seemed much more stable and rates more comparable, as all the gains and thresholds could now be set to the same values of 0 and 6450 respectively, while still showing well aligned peak positions 3.11. This is a huge improvement compared to the previous settings when gains varied by factors almost up to four, reducing potential non-linearities in amplification. Also, gains are left at lower values to begin with, leaving a larger part of the overall amplification to the photomultiplier tubes known for their linear behavior and relatively low noise.

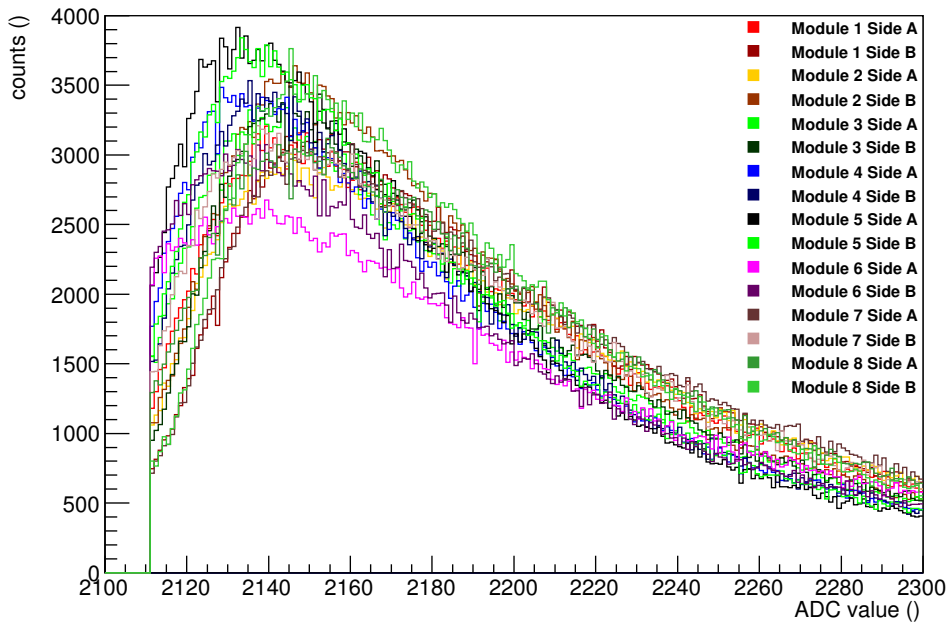


Figure 3.10.: The landau peaks at acceleration voltages about 1200 V. All channels show a comparable width and height. Note that the thresholds had to be set pretty close to the peak position as noise was a huge issue under the conditions of too low acceleration voltages.

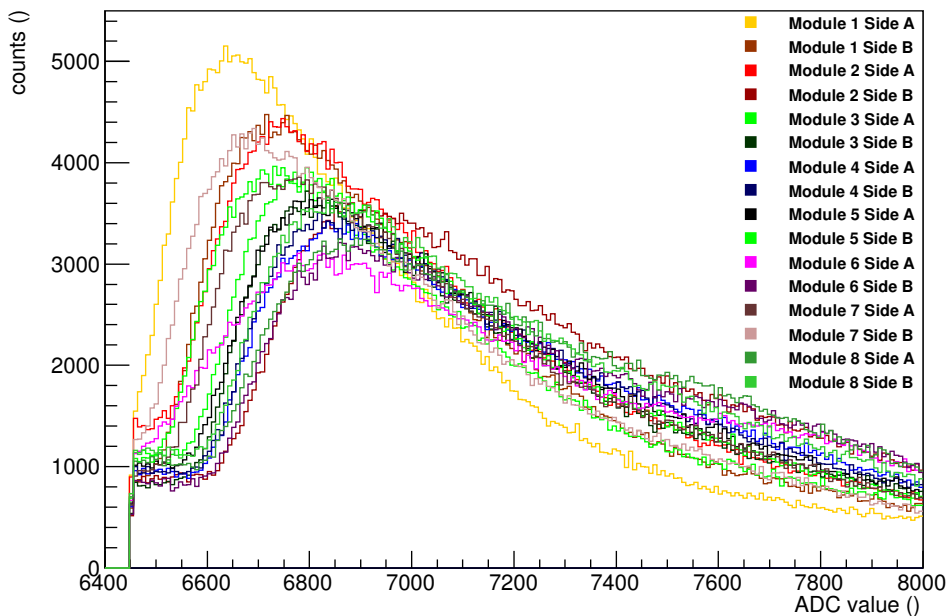


Figure 3.11.: Landau peaks after raising acceleration voltages to 1.5 kV (1.6 kV for 2B and 6B). Note that this pattern was achieved solely by raising two module's side's acceleration voltages to 1.6 kV leaving gains and thresholds at the same low level for all channels.

4. Analysis software

To analyze the data recorded by the DAQ and ORCA software, completely new data structures fit to the needs of muon detection and coincidence analysis were created. Methods were implemented to further investigate data stored inside those structures. A cmake file has been created making it possible to install the programs on any machine used for analysis. That way, programs can be modified for custom analysis that shall include muon data making it very modular. All the sources including the main programs are available on the svn repository.

4.1. Data structure

All data from the IPE-servers arrives converted from ORCA-specific formatting to .root files compatible with CERN’s analysis software ROOT [62]. Hence, ROOT Methods are used to extract data from these structures, while most of these methods are implemented as part of the KaLi package in the Kasper software which constitutes for a complete and closed data transfer protocol. The Kasper software is a simulation and analysis software tool developed and steadily extended by the KATRIN collaboration. Through those structures, data specified by the user will be cached locally and can be analyzed afterwards.

For analysis with the classes described here, all data is transferred from the cached files to runtime storage. Here, the newly written class **event** with the following members comes into play.

event private class members

- fADCValue
- fTimeSec
- fTimeSubSec
- fPanel
- fSide

For each member, corresponding set- and get-methods have been implemented making them accessible to the programmer. Furthermore, the operators "<", "<=", ">", ">=",

”==”, and ”-” have been overloaded to compare the timestamps of the event class. This was useful and since ADCValues are merely used for plausibility checking of the data but not for quantitative analysis, there was no need to compare energy values. Doing so, events and the classes derived can easily be compared and searching becomes cleaner and clearer. Derived from the base event class are two more storage classes:

panelEvent storing a second ADCValue

panelEvent additional member

- fADCValue2

and the common timestamp of events activating both panel sides and **coincidentEvent** storing ADCValues of simultaneous events in multiple modules and the number of modules involved:

coincidentEvent additional members

- std::vector fADCValues
- fnPanels

If a run file is downloaded, the constructor of the class **run** (section 4.3) stores the data of the .root files in vectors of events. Recorded events should already be filtered - only simultaneously occurring events on the two sides of the same module should be recorded. This is set in the FLT dialogue of the ORCA software (section 3.1.1). As, for unknown reasons, single sided events are wrongly recorded, a software workaround is needed. All events of one side of each module are scanned to find whether a corresponding event with the same time stamp exists on the other side . If so, a coincidentEvent is created and pushed back into the run’s vector of coincident events corresponding to the module it occurred in. With the setPanels() function, the modules for analysis can be chosen. This can be done sequentially for multiple sets of modules without repeatedly reading the run’s data, as all the primary data is stored inside the event and coincident event vectors.

run class members

- std::vector events
- std::vector detectorEvents
- std::vector eventsByPanels
- std::vector coincidentEvents
- std::vector selectedPanels

4.2. Search Algorithms

To analyze data, at various points searches for events with a particular time stamp have to be performed. The recorded events are time sorted. A first implementation to search for

coincident events was based on of an average frequency and its standard deviation. This algorithm proved to be fast and stable, though well applicable only for two sets of timed events. That is why an advanced incremental method has been created. The number of modules is now unlimited and the speed is even higher.

4.2.1. Frequency Search

As this algorithm was built to run on only two sets of data, it simply walks through one set incrementally and looks for corresponding data in the other. The latter is not done in the simplest way by incrementing through the second set as well, but by calculating the average frequency of events inside the set and performing an intelligent guess on that basis. If the guessed event has a different time stamp, the algorithm will keep going forward or backward in time in steps of the frequency's standard deviation until the time stamp searched for is in between two step points (figure 4.1). In a last step, simple incrementation is used to find out whether an event at the desired point in time exists or not.

4.2.2. Incremental Search

While the frequency search increments solely one dataset, the incremental search steps through all the event trees, incrementing the one with the smallest time stamp (figure 4.2). It then compares all events to each other, writes out the coincident ones, if any, and goes on incrementing the next smallest stamp. This assures the finding of all coincident events while keeping the speed very high.

4.3. Member Functions of the class **run**

Constructor `run()`

Whenever a new instance of "run" is created, the constructor is called. Arguments to be passed are a `KaLi::KLRIdentifier`, basically a string distinctively naming the run to be analyzed, such as "myo00000001", an instance of `KaLi::KLDataManger`, a class handling the download of the Files form IPE-servers and a toggle variable telling the constructor which data to read via the member function `getRun()` and what member functions to call afterwards.

Toggle Choices

- **0:** Data is downloaded and both muon data and detector data are stored
- **1:** Data is downloaded and only detector data is stored
- **2:** Data is downloaded and only muon data is stored
- **3:** Data is read from local file system, only muon data is stored
- **10:** Monitor spectrometer data is read. Different card and channel configurations are used.

Destructor `run()`

The destructor deletes all the contents of the vectors of events and inherited classes and clears them afterwards before deleting the member `RUN` which in fact frees all the memory reserved by the `KaLi` classes.

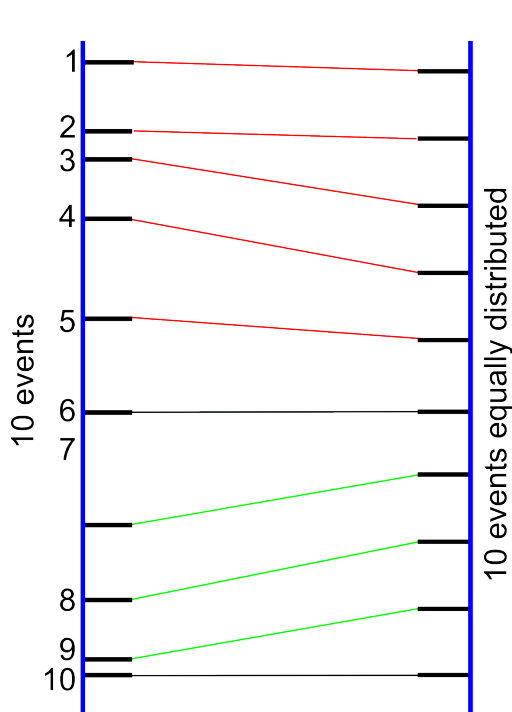


Figure 4.1.: An illustration of the frequency search algorithm. On the right, the events distributed with the average event frequency are shown. On the left, an arbitrary event distribution is given as it might occur in a measurement. The color of the connections shows if the guess was too late and a backward search is started (red) or too early and a forward search is initiated (green). Grey connections are for direct hits.

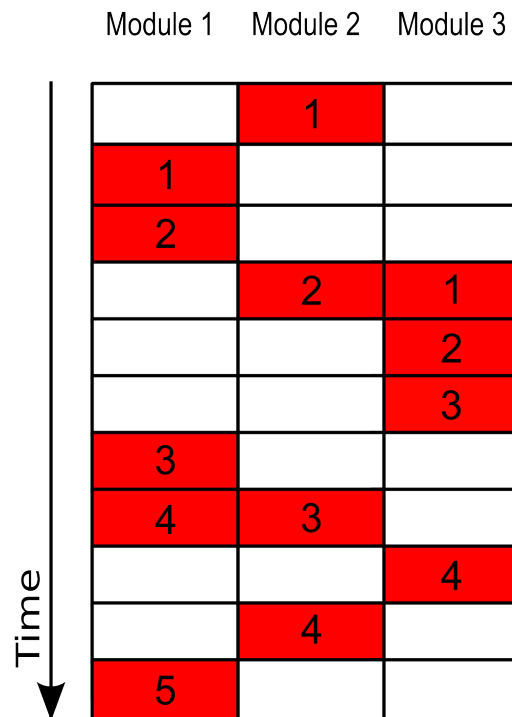


Figure 4.2.: An illustration of the incremental search algorithm. Every column represents a vector of events for one module. Time increases downwards. Red cells are events inside a vector, the numbers define the point of storage. Two double hits are shown - modules 2/2 + 3/1 and 1/4 + 2/3.

getRun()

The getRun function sets the member `KaLi::KLRun` through the `KaLi::KLDataManager` and then returns `KaLi::KLRunEvents`. This means that here, the actual readout of data from the servers is happening. After the getRun function was called, the data is stored in the RAM for analysis. The returned `KaLi::KLRunEvents` includes all recorded events meaning also both the relevant `KaLi::KLEnergyEvents` and `KaLi::KLVetoEvents`. The former is used to store events at the detector, it contains timing information and ADC value of the event as well as information about the pixel where it was recorded. The latter is used at the muon modules. Additionally to the data stored in a `KaLi::KLEnergyEvent`, this class stores information on one or more events in coincidence with the first. In our case this is always the other side of the module. The `getRun()` function is used in the constructor for example to read the run's data.

getLocalRun()

It is not always possible to read data from the file servers, for example in case the files are too big, leading to timeouts at least in older KaLi versions. That is why the `getLocalRun()` function was introduced reading data from the local filesystem via the `KaLi::KLRunIdentifier`. The path to the files can be adapted in the source code. Additionally an environment variable called "MUONLOCALPATH" can be set to change directories without recompiling.

detectCoincidences()

The `detectCoincidences` function calls the member function `channelCoincidences()` and `panelCoincidences(nPanels)` sequentially. It then returns the output of `panelCoincidences(nPanels)` where `nPanels` defines, how many modules have to show coincidences for the counter to increment the number of panel coincidences. At the same time, this empties and refills the vectors of `panelEvents` and `coincidentEvents` according to the latest choice of `selectedPanels`. That makes it easy to call the function multiple times, especially since the analysis is fast compared to the downloading time.

channelCoincidences()

This always clears the vector `eventsByPanels` before filling it according to the current `selectedPanels` settings. To do so, it loops over all entries of `selectedPanels`, calling `loopOverSides()` of the current module.

loopOverSides()

`LoopOverSides` analyzes one of the modules for coincident events between the two sides. The function runs through all the events of one panel side using the operators "`<`" and "`==`" overloaded for the class `run` to compare event times. For the search itself, the "A" side's index is incremented step by step while the "B" side's index is pushed up as long as its event time is smaller than A's. Every time that condition changes, it checks whether the events occurred at the same time - pushing back a `coincidentEvent` with both the events' ADC values and their time stamps into the vector for the corresponding module if so - and then going on incrementing module A's index.

panelCoincidences()

As mentioned in the chapter 4's introduction, the first algorithm to search for coincidences between different panels was based on the average event frequency and its standard deviation, soon being replaced by a simpler, more efficient incremental algorithm: This new algorithm

features a storage for the smallest timestamp in a group of events. It is initially set to the timestamp of the first event of all the modules analysed. Now, all the events are compared to find the smallest. This has the advantage, that one does not need to cross check every event with every other one but can simply compare every event to the smallest in a linear way. If simultaneous events are found, they are pushed back into the coincidentEvents vector together with the timestamp and their ADC values while nPanels is risen by one. Subsequently, the index of the smallest event stored is incremented and the new smallest event in the changed pool is searched for via the member function findSmallest(). This is repeated until all the event storages have reached their last entry. The return value is the number of events fulfilling the requirement passed through nPanels to panelCoincidences: if it is zero, every coincident event with two or more modules involved is counted, for every other number, only the number of event with exactly this number of modules is counted.

findSmallest()

This function returns the smallest panelEvent's time stamp through references as both a second and a subsecond count have to be returned. The findSmallest function accepts panelEvent-indices of the different modules and returns the one with the smallest time stamp.

TOFHist()

Setting the modules to be analysed to one and two, this function was designed to analyze monitor spectrometer data. This also reflects in the fact, that both muon data and detector data are expected to be stored within the same mosxxxxxxxx run file. The function then runs channelCoincidences() and panelCoincidences() before shifting through all the muon events searching for coincident detector events in a certain time interval. The time interval is chosen on function call. Time differences are stored in a vector of events passed by reference to the function.

TOFMuonDet()

In contrast to the TOFHist function, this one reads muon and detector data from different files as it is designed for the needs of main spectrometer analysis. Here, two DAQs record muon and electron detections to myo... and fpd... files, respectively. That is why the function reads a muon run and requires a guess as to where corresponding detector data is located. It then searches the given detector and moves on as long as no change of sign in the time difference occurs. To do so, it might also read new detector runs. If the time difference sign changes, the function searches for a detector event within the time window passed on call and pushes it back into a vector of events of time difference. A histogram can now be filled with the data acquired to inspect it for cumulation of time difference events at particular times.

determineEfficiency

Efficiencies of modules can be determined through three of them located coextensively in front of each other. Then, all events recognized by both the uppermost and the lowest module have to - ignoring geometrical inaccuracies - pass the middle module as well. By comparing the counts one can determine an efficiency for the middle module. Usually, the modules used are 6, 7 and 8 though for testing purposes also modules 3, 4 and 5 have been analyzed.

$$\%_{eff} = \frac{\wedge_{68}}{\wedge_{678}} \quad (4.1)$$

To do so, the function reads a muon run, selects three modules and runs the channelCoincidences() and panelCoincidences(3) functions. The returned number of events detected

in all three of the modules is stored. Then, only the outer modules are selected and panelCoincidences(2) is called. The ratio of the two panelCoincidences calls is the return value of the function.

getSize()

The getSize() function returns the size of one of the vectors storing events or one of the inherited classes depending on the passed integers “what”, “module” and “side”.

“What” can be used to choose from:

- **1:** Size of events returned
- **2:** Size of eventsByPanels returned
- **3:** Size of coincidentEvents returned
- **4:** Size of detectorEvents returned

If one, two or three are chosen, the module number (and side in case of one, 0 being A and 1 being B) can be passed to choose the size of which vector to return. By default, module module 1 (side A) is returned.

readVetoEventData(), readDetectorData() and readMOSDetectorData()

Depending on the toggle choice in the constructor, either one of the three or two of the functions are called. The readDetectorData() function reads all recorded KaLi::KLEnergyEvents which are only recorded by the FPD and the monitor spectrometer. The readVetoEventData() function reads all the KaLi::KLVetoEvents from the cards in slots three, six and nine. This can never interfere with veto data recorded at the FPD for the active veto for the detector signals, as cards 15 and 16 are used here. For analysis of monitor spectrometer data, a function readMOSDetectorData() has been implemented reading all energy events of card one independent of channel, while of course single channels can easily be excluded. The pulser usually active at the monitor spectrometer creating KaLi::KLEnergyEvents at constant frequency is by default excluded from analysis. Inside the readVetoEventData function, an additional readout from card 4 has been integrated for monitor spectrometer veto signals. This slot is unused at the main spectrometer meaning the events can be easily distinguished in analysis. All the member functions reading data require the passage of an instance of the KaLi::KLRunEvents, usually the member of the same class set in the getRun() function.

5. Simulation of Background Inducing Muons

To compare the data acquired to theoretically expected values, a Geant4 [63] simulation of cosmic showers has been set up including the geometry of the main spectrometer as well as the muon modules. Using this software, incident muons can be simulated and the effect on the main spectrometer and the muon modules can be evaluated. It was especially relevant to achieve estimations on how many of the muons penetrating the main spectrometer are actually registered by the muon modules. From this simulation, the overall rate of muon impacts on the main spectrometer can be obtained. Comparing this overall rate to detector rates for asymmetric fields enables a determination of the probability of a muon hitting the main spectrometer inducing an electron.

5.1. Geant4

The Geant4 package is a powerful tool for simulation of particles. It has many particle interactions already included making it easy for the user to set up and run simulations. To start a run, a geometry, one or multiple detectors and interactions have to be defined. Each run may consist of one or more events. During a single run, a loop of processes is called:

1. Primary Generator Action
2. Run action
3. Event action
4. Stacking action
5. Tracking action
6. Stepping action

Each run usually contains many event actions and every event action multiple tracking actions. For each item above, classes with the addition ‘user’ to the base classes name can be called before or after the standard action class. These are used to extract the required data. In this simulation for every event in which a muon module has been hit, its copy number is pushed back to a vector of event data. The visualization of the simulated data is controlled via a “.mac” file, by default the “vis.mac” file. Different parameters can be changed and simple visualisation settings like viewing angles and zooms can be chosen. An example is given in appendix G.

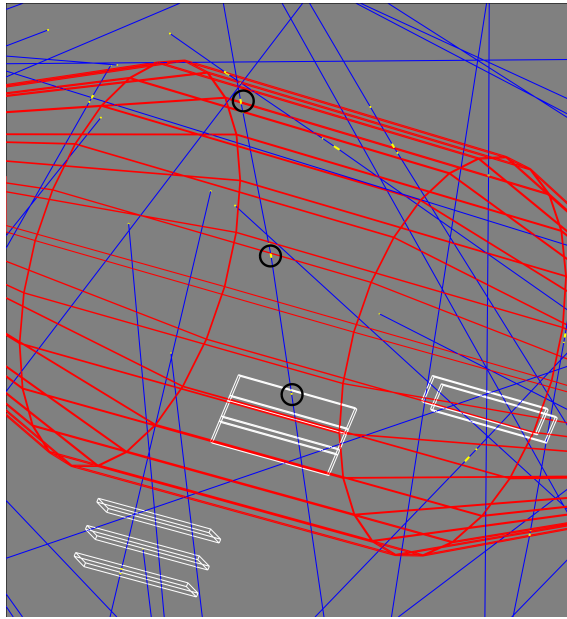


Figure 5.1.: Screenshot of the geometry setup and muon paths in the OpenGL viewer. The view is upwards through the main spectrometer when standing on its west side. The three groups of muon modules (white) are visible right below the large main spectrometer structure (red). A variety of incident muons is shown (blue). Hits are marked (yellow) by the Geant4 viewer. The hits of a particular muon are marked with black circles. Both entry and exit point into and out of the main spectrometer and the detection point are visible.

5.2. Geometry Setup

To set up a geometry, the class `G4VUserDetectorConstruction` is used. `B1DetectorConstruction` inherits from that as a base class and additionally contains all of the geometrical parameters needed for the setup such as radii of the main spectrometer cones or positions and extent of the muon modules. Every shape generated is made up of both a logical volume `G4LogicalVolume` and a physical volume `G4PhysicalVolume`. The logical volume describes the intrinsic properties of the geometric object added: its shape, its size and its material. The physical volume accepts a logical volume as input providing position and alignment of the previously defined. Inside the detector construction class, all of the materials used in the simulation need to be defined as well. These are the components of the air outside and inside the spectrometer including pressures and constitution, the stainless steel of the spectrometer wall and the scintillator material of the muon modules. The main spectrometer geometry was already existent (see [64]), but had to be modified as many border volumes were implemented. These were very flat volumes covering any area of the main spectrometer not needed for this simulation. Additionally, the muon modules were added as sensitive volume, while keeping in mind that one wants to not only distinguish whether a module has been hit, but also which one. That is why the logical volume for every module is the same whereas the physical volume is a copy of the first at different world coordinates making them identifiable via their individual copy number. A screenshot of the visualized geometry setup including a hit of one of the modules is shown in figure 5.1.

5.3. Muon Generator

The muon generation was realized through the primary generator action. The angular distribution suggested by Henrik Arlinghaus [65] was implemented. The angular rate

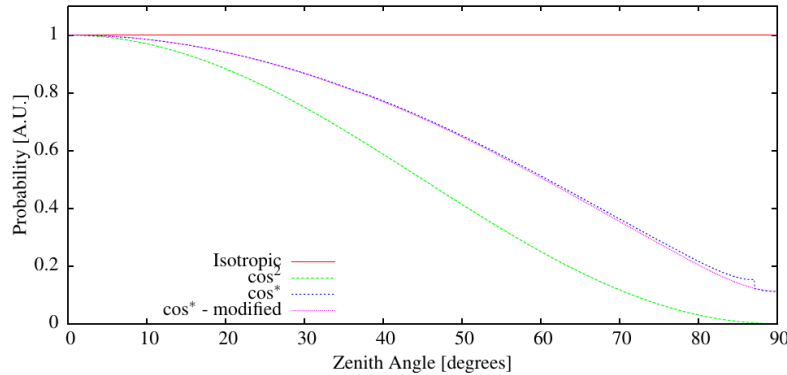


Figure 5.2.: Angular distributions. Isotropic and \cos^2 distributions are shown opposed to the \cos^* distribution. The latter is plotted with and without a wrongly published parameter from the original publication [66].

Table 5.1.: Coefficients required for equation 5.3. Every set of coefficients is applicable to a certain angular region indicated in the first column. The last column shows the largest occurring relative error in each region.

$\cos(\theta)$	c_0	c_1	c_2	c_3	c_4	max. rel. error
0 - 0.002	0.11137	0	0	0	0	0.004
0.002 - 0.2	0.11148	-0.03427	5.2053	-14.1971	6.138	0.3
0.2 - 0.8	0.06714	0.71578	0.42377	-0.19634	-0.021145	0.7

dependence is shown in 5.2. The energy was set to 1 GeV disregarding the actual energy distribution as this was mainly about flight paths that are not strongly dependent on energy at high energies. Starting positions were spherically distributed, with the direction towards the origin, which is in the center of the main spectrometer. Starting positions were then randomly moved in a volume surrounding the spectrometer to account for the non-point like structure of the detection system as a whole, while the distribution describes a single point in space. The distribution used is the \cos^* distribution.

$$\cos^*(\theta) = S(\Theta) \cos^{**}(\theta), \quad (5.1)$$

with

$$S(\theta) = 0.986 + 0.0007 \sec \theta \quad (5.2)$$

and $S(\theta)$ described by a polynomial

$$\cos^{**} = \sum_{i=0}^4 c_i \cos^i \theta. \quad (5.3)$$

The coefficients are defined differently for different angular ranges shown in table 5.1.

5.4. Hit Counter

To compare moun measurements and simulations, events with at least one module hit were counted. This enabled a comparison of the rates of single modules, showing that the generator works fine. Furthermore, it allowed for an estimation of the number of muons hitting the modules compared to the total of inciding muons. Table 5.2 shows the result of a simulation generating 10^6 particles and compares it to measured data. Of the particles generated, the single modules were hit 506 ± 44 times. In the same period, the main

Table 5.2.: Comparison of the simulation to measured data, showing an agreement >90 %.

module	1	2	3	4
simulation	550	534	499	410
data	495 ± 23	544 ± 24	497 ± 23	483 ± 22
module	5	6	7	8
simulation	508	543	506	496
data	490 ± 23	498 ± 23	510 ± 23	532 ± 24
modules	1+2	6+7	7+8	6+7
simulation	204	135	130	66
data	191 ± 14	136 ± 12	146 ± 12	65 ± 8
	6+7+8			
simulation	66			
data	62 ± 8			

Table 5.3.: The ratio of a multi-module event is compared to the average rate of the single modules. Simulation and real data show comparable values.

ratio	N_{12}/\bar{N}_{single}	N_{67}/\bar{N}_{single}	N_{78}/\bar{N}_{single}	N_{68}/\bar{N}_{single}	N_{678}/\bar{N}_{single}
simulation	0.40	0.13	0.27	0.13	0.26
data	0.38	0.27	0.29	0.13	0.12

spectrometer was hit almost 6×10^4 times. This clearly shows that the detection system is by no means a veto system to discriminate muon induced events, but merely for background studies. To compare simulation to real data, a time scale had to be introduced. The number of events simulated for a single module corresponds very well to 2 s of measurement time. Consequently, the simulation has been compared to the 2 s average of a half hour run. Especially important is that the ratio of multi-module events to single module events is comparable. This can be used as a direct validation of the simulation's angular distribution. The different distances between the single modules are responsible for the difference in counts for multi-module events. The ratios are shown in table 5.3.

The simulation data can be used to estimate the probability of a muon inducing an electron at the detector after taking long term measurements with high statistics. Furthermore, by saving entry and exit points into and out of the main spectrometer, a heatmap of the main spectrometer can be made. Particle tracking from these points with the already available Kassiopeia software will provide more information on and improve the understanding of the background process.

6. Comissioning measurements and analysis

While the muon detection system was still under construction at the beginning of this thesis, first measurements were taken at the time with similar, already commissioned modules under preliminary conditions to investigate their general behavior. Step by step, the system was completed and is now up and running. In the building phase, several measurements and tests have been conducted to ensure the capabilities of the system meet the requirements for the KATRIN experiment. Initially, the acceleration voltages, gains and thresholds had to be set up. Using data acquired by the muon modules and the detector, as well as data from other subsystems, the muon induced background rates as well as both spatial and energy distribution can be obtained. Before actual measurements were done, the modules had to be set up and calibrated, meaning high voltage and signal cabling needed to be installed and high voltage power supplies had to be acquired.

6.1. Finding the best filter settings

As the PMT tubes are directly, without any pre-amplifiers, connected to the DAQ, the signal lengths arriving at the latter are in the order of 20 ns. This poses a problem for filters as the sampling rates need to be high and anti-aliasing is inevitable. To find the best settings, a function generator has been set up to create events at known frequency and peak height. The function generator's signal form was chosen as closely to the actual shape as possible, which is the "pin diode" form (figures 6.2, 6.1).

In order to evaluate filter's figure of merit, the width of the resulting energy histogram, which should, assuming perfect pulser signals and perfect filters, be mono-energetic, was analyzed for each filter setting. For analysis, the width of the contributing ADC bins and their absolute position as well as the pulse height and the filter settings were noted.

On average, the boxcar filter at shaping lengths of 150 ns shows the most promising results, i.e. the sharpest energy resolutions for any signal height. This concurs with the settings chosen for the active FPD veto; here slightly longer (around 30 ns) but comparable signals enter the DAQ's FLT cards showing best results at the same filter settings[67]. That is why, for any measurements after myo00000830, the new filter settings were used, bringing up the need for new threshold and gain adaptions 3.5.

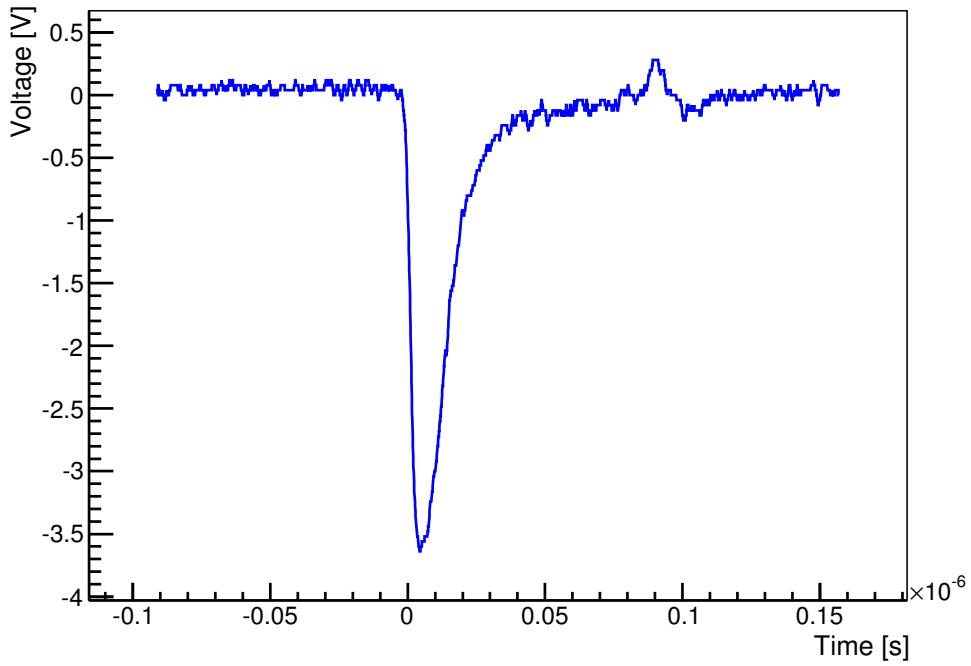


Figure 6.1.: A signal as recorded by the muon modules with an oscilloscope.

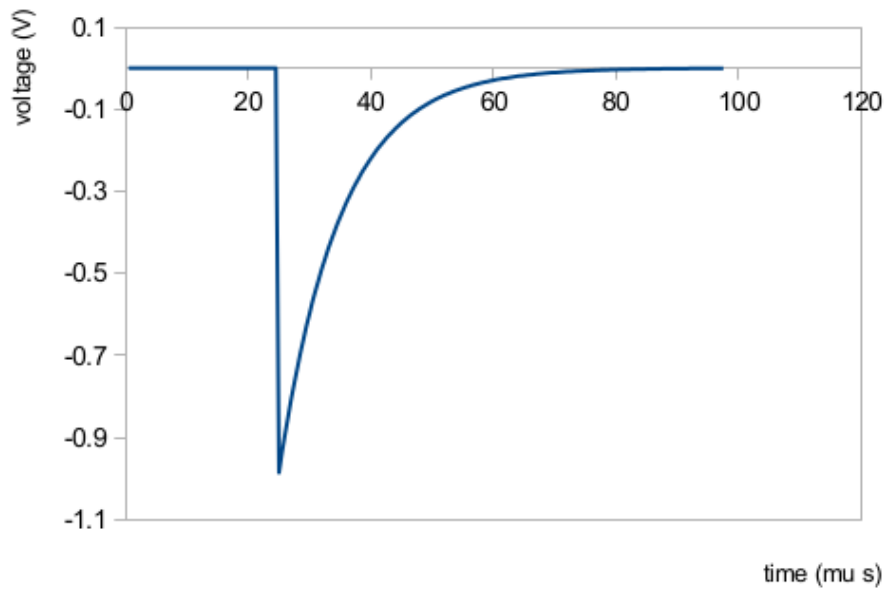


Figure 6.2.: The arbitrary pulse form used for testing purposes. Different voltages were tested. Here, the peak height of 1 V is shown.

Table 6.1.: Energy resolution at different filter settings. A function generator was used to simulate pulses from the muon modules.

Voltage[V]	Boxcar length [ns]	width	position	threshold
1	50	33	2160	2100
	100	37	2140	4200
	150	13	2140	6300
	200	21	2141	8400
2	50	25	2160	2100
	100	63	2140	4200
	150	22	2140	6300
	200	77	2141	8400
3	50	28	2160	2100
	100	37	2140	4200
	150	24	2140	6300
	200	42	2141	8400
4	50	19	2160	2100
	100	31	2140	4200
	150	16	2140	6300
	200	25	2141	8400
5	50	25	2160	2100
	100	33	2140	4200
	150	21	2140	6300
	200	41	2141	8400

6.2. Rates of single muon modules

A simple first check into the data was possible by comparing the measured rates to literature values, where a flux of around 1 muon per min and cm^2 through an area parallel to the ground is stated [68]. The rates measured by a single module are in the order of 250 Hz. The muon modules' area amounts to

$$315 \text{ cm} \cdot 65 \text{ cm} = 2.05 \text{ m}^2. \quad (6.1)$$

When considering the 45° tilt of the modules towards the horizontal, this area reduces to an effective area of

$$A_{\text{eff}} = \sin(45^\circ) A_{\text{real}} = 1.45 \text{ m}^2. \quad (6.2)$$

Further taking into account detection efficiencies η discussed in section 6.5, we receive an estimation of effective rate of

$$\Phi_{\text{est}} = \eta \frac{1}{\text{cm}^2 60 \text{ s}} A_{\text{eff}} = 225 \text{ cps} \quad (6.3)$$

This compares well to measured rates of (241 ± 33) cps.

6.3. Operation in high magnetic fields

Photomultiplier tubes can not be operated high magnetic fields. As mentioned before, they use electrons cascading in electric fields to generate amplified signals. Additional magnetic fields can prevent the electrons from reaching the dynodes, stopping the cascade and thus keeping single events from being registered. As there is the need to position the muon modules as close to the spectrometer tank as possible to register mostly muons that indeed went through the vessel, they are aligned closely to the LFCS system where

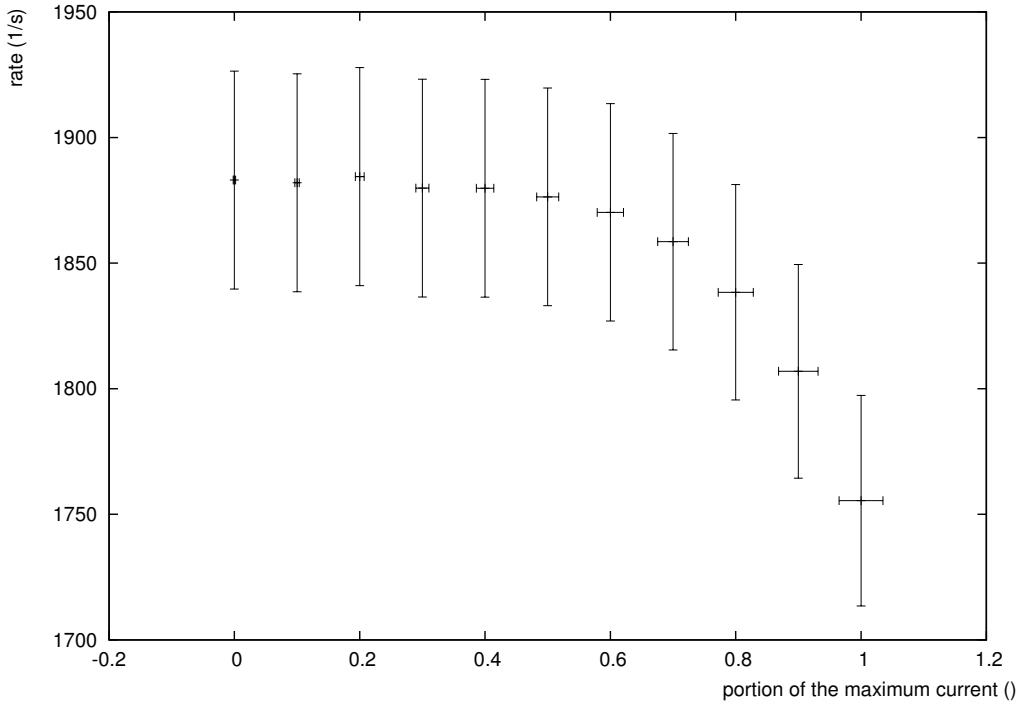


Figure 6.3.: Summed rate of all modules over air coil currents. Currents are displayed as parts of the maximum current. A clear decrease in rate is recognizable from 60 % of the maximum current upwards.

fields of up to 10^{-3} T prevail. As rate decreases strongly - up to a complete breakdown of the signal[69] - under these conditions, a solution needed to be found. As a simple, yet efficient passive counter measurement, a cylindrical layer of mu-metal was wrapped around the photomultiplier tubes. Mu-metal is a magnetically highly permeable material (μ_r on the order of 10×10^5 [70]) that guides the magnetic field lines inside itself. In doing so, the remaining flux inside a mu-metal surrounded volume, and with it the field strengths, drastically reduces. For a sphere with inner radius a and outer radius b , the shielding factor F is given by

$$F/B_0 = 9 / (2\mu [1 - (a/b)^3]), \quad (6.4)$$

where B_0 is the initial magnetic field strength and μ the magnetic permeability of the material [71]. Though the shape used is not spherical, the reduction factor with layers of the used thickness of 0.8 mm indicates a relative decrease in fields of three orders of magnitude. Even if, due to the deviant shape, this factor reduces slightly, the shielding should be sufficient for the prevailing fields.

To test the improvement achieved by the mu metal coverage, measurements with rising aircoil currents have been performed. Steps in the size of tenths of the maximum current were used to record rates over half an hour at each value. For most of the LFCs coils this were 100 A, in some cases (LFCs 1,2 and 14) only 70 A. During the first run, due to a slow control problem, the current was not raised between two steps. Although displaying the expected behavior - rates dropped much less than before - the measurement was repeated with the correct currents at every steppoint. Measurements show that the rate still drops at currents close to the maximum, though only to around 90 % of initial values, (figure 6.3). As, under normal measurement conditions, the LFCs currents are mostly around half the maximum value or less, the problem was solved. In that region, the reduction in rate is within the errors' order.

Coil #	1	2	3	4	5	6	7	EMCS h
Current [A]	10	10	14	25	42	39	54	50
Coil #	8	9	10	11	12	13	14	EMCS v
Current [A]	54	21	36	30	21	20	56	15

Table 6.2.: Runtime settings for air coils as used for the commissioning measurements.
These were kept static over the two weeks end 2012/beginning 2013.

6.4. Module Stability

If consistent factual statements on muon induced background are to be made, the modules need to work stable over the course of days, as rates are supposed to be comparable. For this reason, over the Christmas time 2012, a two-weekly measurement of half hourly runs was taken, see table 6.2 for air coil settings used. Runs myo00000051 to myo00000675 contain the data of this measurement. The time slot was chosen because of the less frequently accessed spectrometer hall, thereby minimizing external impacts on the measurement. During data taking, the LFCS coils were active. They generated magnetic fields in which the PMT tubes had to work throughout the measurement. The LFCS settings are found in 6.2. For analysis, a simple program to count events in variable time bins was written, creating a count histogram for all the runs in the measurement period. The result can be seen in figure 6.5. A fluctuation of 5 % of the average value is observable. This variation can be ascribed to fluctuations in atmospheric density, i.e. pressure Δp and temperature ΔT and in muon production height Δh . The change in relative intensity is described by

$$\frac{\Delta I}{I} = -(\alpha_\mu \Delta p + \beta \Delta h - \gamma \Delta T), \quad (6.5)$$

where α is a barometric coefficient in $0.215\% \text{ mmHg}^{-1}$, β a decay coefficient in $5\%/10 \times 10^3 \text{ m}$ and γ a temperature coefficient in $0.1\% \text{ K}^{-1}$ [72]. Looking at weather data from [73] available on a daily basis, the fluctuations resulting from equation 6.5 do not fit the data very well. Both highest and lowest value for pressure and temperature were used to calculate daily maxima and minima in intensity. The relative change was projected onto the average rate in figure 6.5. Although the order of magnitude does not differ vastly, even the rate development does not always compare to the ones visible in the data of the stability measurements. Several reasons may contribute to this. It has to be kept in mind that the weather data was obtained from a weather station in Rheinstetten, about 20 km south of KIT campus north. Furthermore, the station only records data from the lowest atmospheric layer while muons are generated mostly in the upper layers of the atmosphere. Additionally, and this is probably the largest factor here, the muon production height was not included in the analysis as no data was available for this. As all of the fluctuations are in a window of around $\pm 5\%$, the modules' intrinsic stability does not overcome the weather induced fluctuations in muon flux. For further information on these variations, see [74].

6.5. Module Efficiency

The runs used for stability measurements, as well as any other run including three modules coaligned in front of each other, can be used to check the middle module for efficiency. For tests on other modules, the geometry would need to be changed so that the one to be checked is in between at least two other modules. For analysis, the function `determineEfficiency()` in 4.3 has been written. The principle is the following: considering the small change in

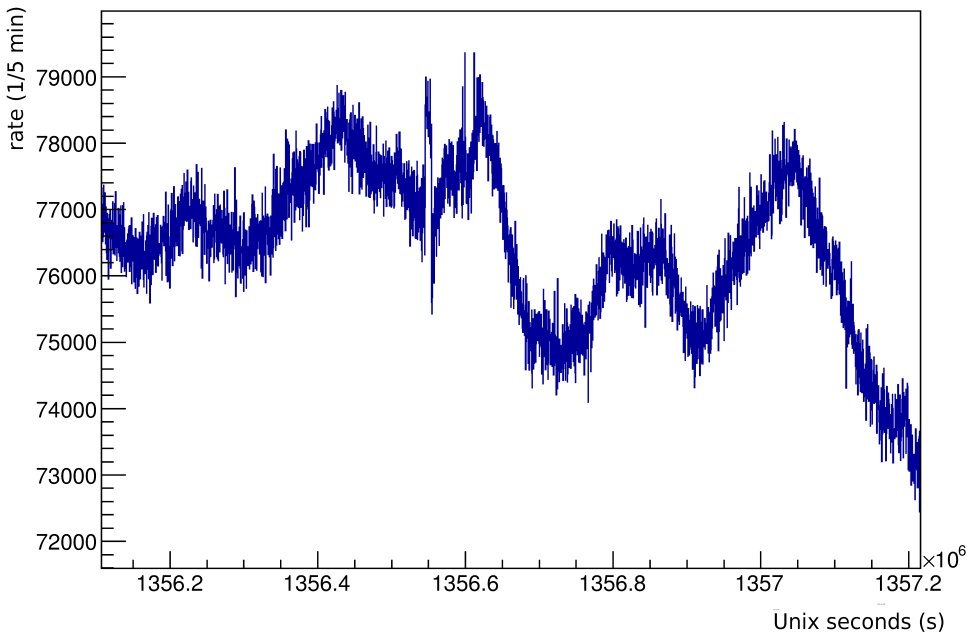


Figure 6.4.: Counts per five minutes over the course of about two weeks (21-12-2012 to 03-01-2013). The rate deviates 5 % from the average.

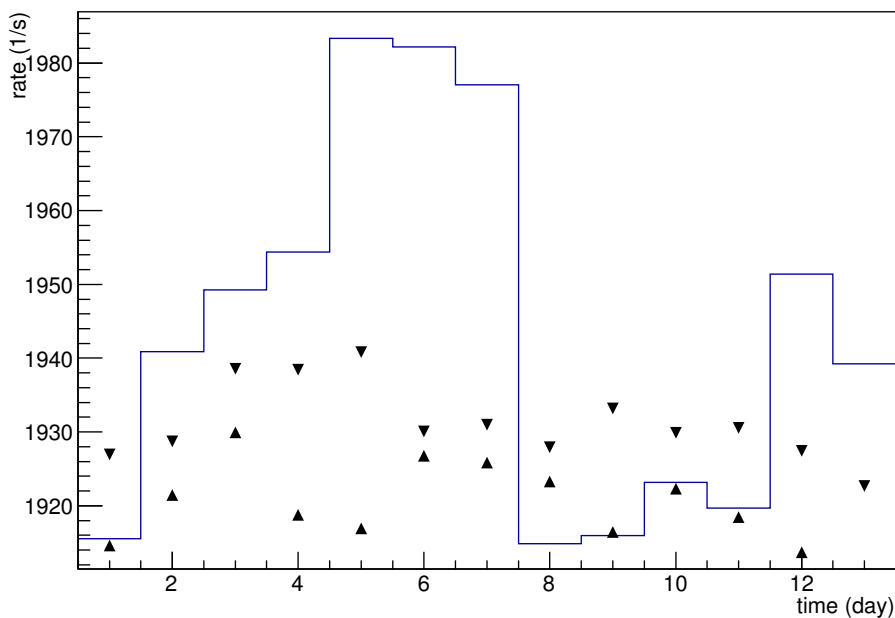


Figure 6.5.: Atmospheric density as a function of time over the course of the two weeks during which the muon measurements took place. Rate is displayed as a daily average. The black triangles show the maximum and minimum deviation off the average rate calculated with 6.5

momentum direction which high energy muons achieve through interaction with matter, one can assume straight-lined paths. From that follows, that if two parallel planes, used to describe the scintillating volumes, are hit, any other, also parallel plane, in between those two will be hit as well. Keeping this in mind, one can analyze data for events registered in both modules 6 and 8 and cross check whether an event has been detected in module 7 as well. The quota of events in all three modules compared to those detected in 6 and 8 - including the triple events - shows the efficiency of module 7. It shows that during the measurement period end of 2012, the efficiencies were at $(92.8 \pm 3.8)\%$ which is less than one would expect at a scintillator thickness of 5 cm. For that reason, the filter settings were checked and changed to the boxcar filter with a gap of 150 ns from the before used trapezoidal filter. However, the expected efficiency increase was not observable. The average efficiencies were now at $(93.4 \pm 3.4)\%$, well within the margin of error of the previous measurement. To examine the problem further, modules 3, 4 and 5, that are located next to each other, were used for efficiency measurements as well considering they are stacked in an upright way. Using the program on those three modules resulted in even lower efficiencies of $(50.0 \pm 3.2)\%$. This raises the question whether this is not an effect of signal filtering, but a previously not considered physics effect. One thing coming to mind is deviation of the muon track from linear forms. This feature would comply with the seemingly lower efficiency at the upright stacked modules, where, at equal bending radii, the ratio of muons traveling around the middle module is higher due to the lower total area in stacking direction. This hypothesis should be tested via simulation of the cosmic muons including magnetic fields and empirically via variation of the distance between the single modules. The latter is difficult not only because the modules are heavy and not made for lifting (no designated carrying structures), but also because movement always means potential danger to the photomultiplier tubes and their connection to the scintillators. Furthermore, if all coils and solenoids were to be turned off simultaneously at some point, one could collect data then and see how efficiencies change during that (there have been runs taken when that was still the case, but only few modules were working properly at that point). If the dependence on module distance turns out to be true, but the efficiencies are still below expected values at the lowest possible distances, a possible improvement would be to use pre-amplifiers before signals arrive at the DAQ. These would widen the signals time-wise leading to a more easily detectable signal for the filters.

6.6. Photo Multiplier Tube Test with ^{90}Sr source

With sets of four photomultiplier tubes being read out over one cable, and, consequently, via one channel, the test of individual PMTs is not trivial. Nevertheless, a method using a MBq ^{90}Sr source to trigger events was used to check functionality. Of course, all tubes were able to detect the source's β -electrons at any position but rates were expected to rise with decreasing distance to one of the tubes. A source holder was constructed from acrylic glass to shield the user from radiation and to attach the source to the modules, as a large dependence of rate on the position was found when the source was simply duct taped to the modules. As the foil mantling of the modules absorbs a large part of the radiation emitted from the source, it had to be ensured that the number of layers was equal for all measurements. This was given only below the modules as the foil has been folded around them at the ends in a gift wrapping way. Thus, the source was pretty far away from the photomultiplier tubes making it more difficult to distinguish between them. A first measurement was to check for exactly this distinguishability.

The first approach for a clear identification of the single PMT positions had to be dropped as all of the PMTs seemed to detect too much of the source's decays at any position (figure 6.8). This behaviour got worse moving away from the photomultiplier tubes as the distances to the individual tubes equalized. At the same time, the closer the source was

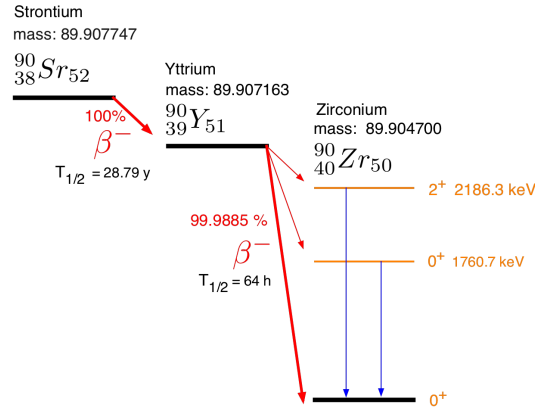


Figure 6.6.: Decay scheme of ^{90}Sr : first a lower energetic decay to ^{90}Y emitting 544 keV/c² electrons, from that most probably a higher energetic decay to ^{90}Zr ground state (2.29 MeV/c² electrons) or, with low probability, to one of two of its excited states.

moved towards the PMT tubes, the larger the position dependence, making it difficult to compare results (figure 6.7). Therefore, it was decided to measure at the four points the PMTs were located at and compare both the behavior of the rates and their overall value. The tube positions were used as measurement positions. For each side, a run has been taken containing five minute subruns for every position. Figures 6.9 to 6.11 show the result of these measurements. One can see that the general shapes compare well to the others. Exceptions are modules 2B and 6B that show lower rates than the others. This has been compensated for by an adaption of acceleration voltages.

6.7. Synchronization of muon detection system and FPD DAQs

Measuring time differences between detector signals and muon events on a μs scale requires exact synchronization of the two different DAQs. For this purpose, a clock has been designed sending signals at two frequencies: one at 1 Hz and one at 10^6 Hz internally converted to a $2 \times 10^6\text{ Hz}$ signal by the DAQ. Those signals can be synchronized to the timestamps of GPS satellites if a GPS antenna is connected. This has not yet been done as relative synchronization between the two crates is sufficient for the purposes of finding correlations between muon and detector events. For this synchronization to work, it must be ensured that in the SLT dialogue, in the “seconds” section, the radio buttons “Host time” and “Use for FLT cards” are clicked. Additionally, in the FLT dialogue in section “Init event time with”, the dropdown menu must be set to “SLT seconds”. As the cable length for signal transmission is pretty extensive - around 50 m - it was decided to use optical fibers instead of CAT 5 cabling. As two signals need to be transmitted, paired ST connector, multi-mode fibers for 850 nm wavelength were used. The clock itself has optical outputs, the DAQ though needs converters from optical to electrical signals and a modified SLT back panel card to receive the converted signals via Cat5 cabling. To test the setup, the muon DAQ was moved to the detector platform. Both crates were fed by a pulser signal. Runs at different frequencies were recorded to test both the synchronization and the detection of events. At first, manually triggered signals were used in minute runs to check the timestamps equality. Several runs were taken, all showing that the events were shifted by several μs . In close cooperation with the IPE it was found that this was merely a problem of firmware versioning as well as software settings in ORCA resolving the problem quickly. After installing the latest firmware, more runs were taken now displaying the desired behavior. Following the manually triggered events, runs with fixed frequency events were recorded, raising the frequency up to 10 kHz. In doing so, different recording

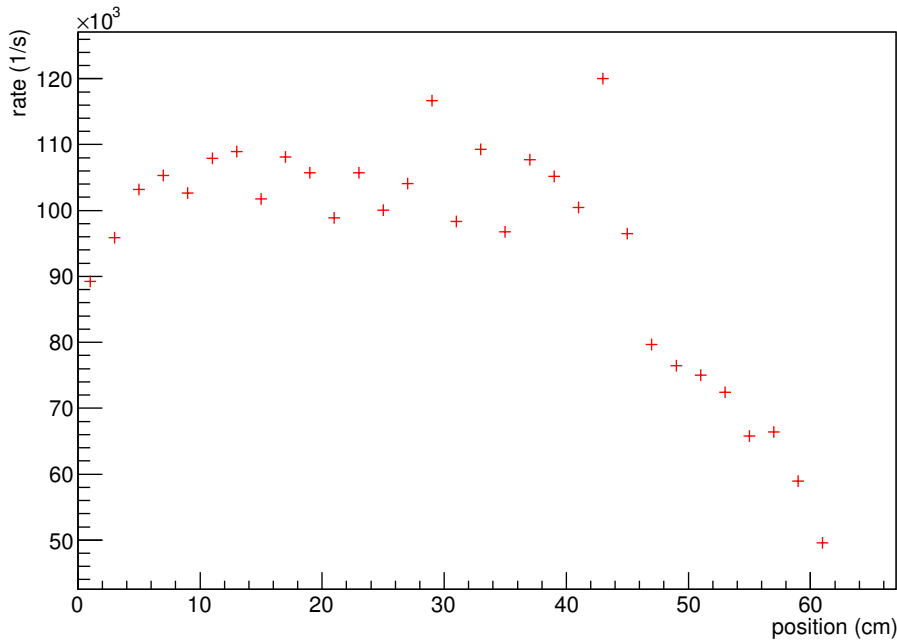


Figure 6.7.: One of multiple scans taken showing that individual PMT tube positions can not be resolved. The rate at different positions along a line parallel to the PMT alignment is plotted. Only the peripheral areas show drops in rate as the angular coverage of the source gets smaller there.

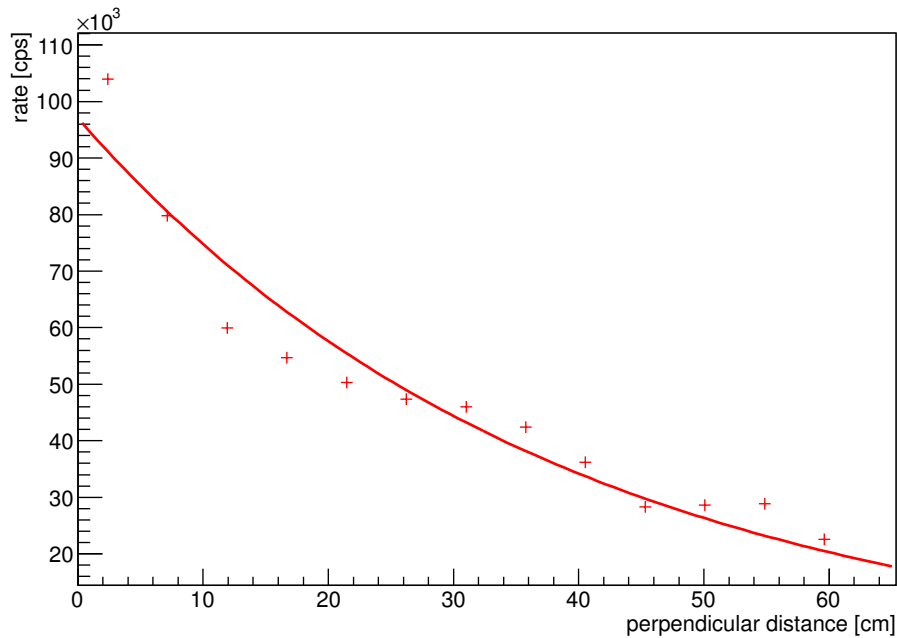


Figure 6.8.: A position scan along a line perpendicular to the PMT alignment. The rate decreases strongly as the distance gets larger.

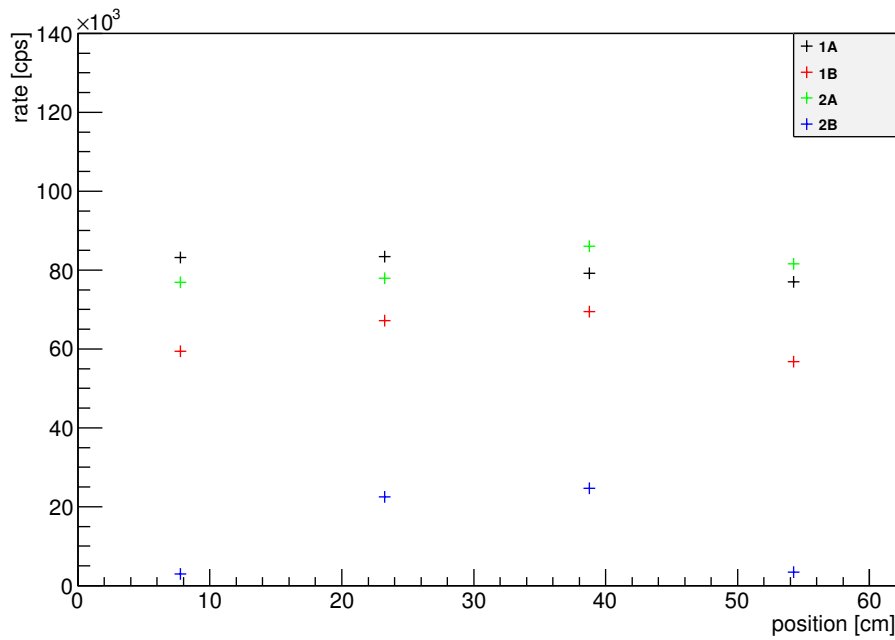


Figure 6.9.: Measurements with the source at four different positions. Both sides of modules 1 and 2. Noticeable are the much lower rates for module 2B which is one of the two that was later set to 1.6 kV acceleration voltage.

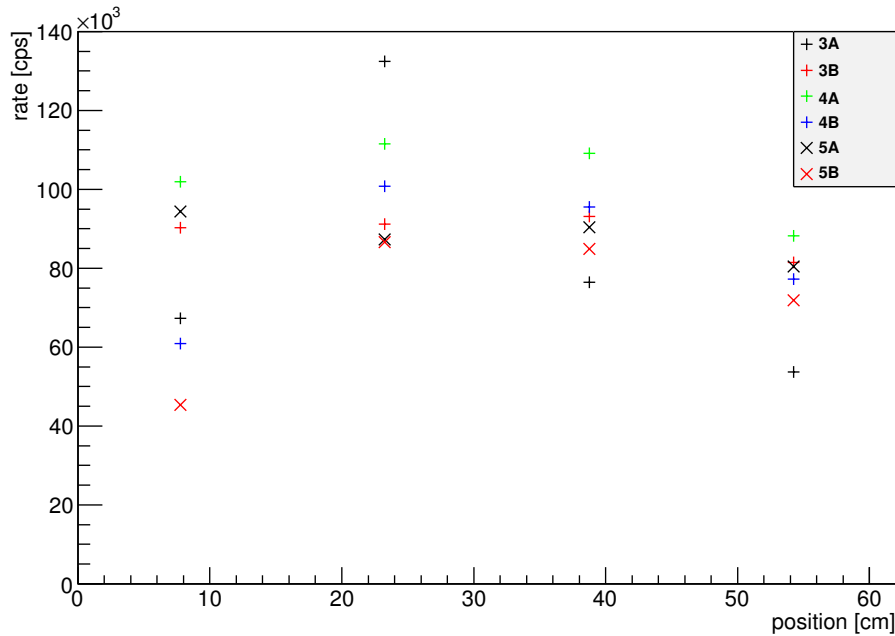


Figure 6.10.: Measurements with the source at four different positions. Both sides of modules 3 to 5 are shown. Except for single measurement points that are standing out, the different sides show similar rates.

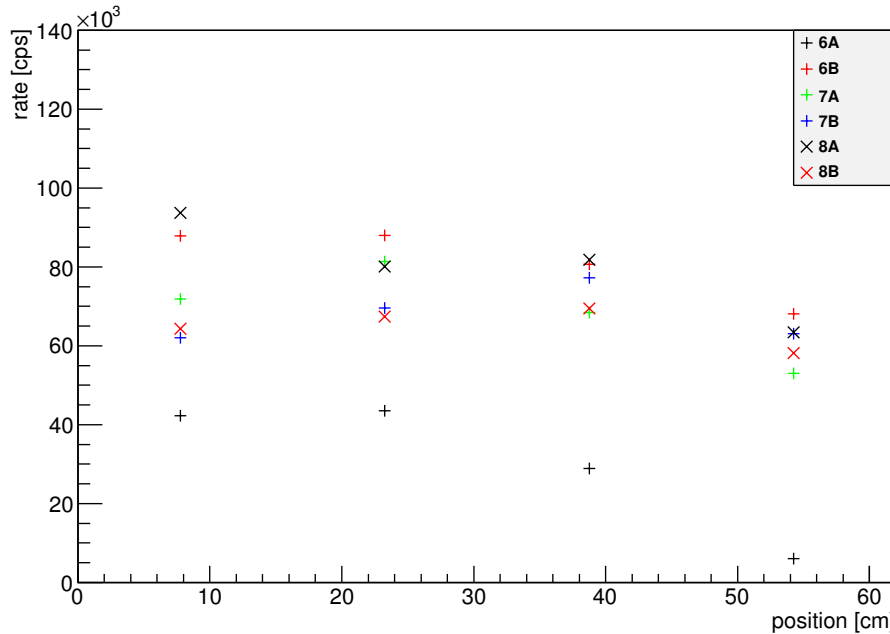


Figure 6.11.: Measurements with the source at four different positions. Both sides of modules 6 to 8. Noticeable are the lower rates for module 6B which again is one of the two that was later set to 1.6 kV acceleration voltage.

modes and filter settings were applied - see table 6.3. All the tests worked fine including starting one DAQ's run way ahead of the other or mixed filter settings. Those events recorded in both run files were always synchronized.

Afterwards, the muon DAQ was moved back to its original position and the optical fibers were stored in wire-ways guiding it from the detector platform down to the basement where the muon detection system is located. Another problem occurred here, as signal transmission was impaired by a kink at one of the turns, but was quickly resolved by smooth rewiring. Concluding, it can be said that the clock runs continuously without any problems throughout all the measurements - including main spectrometer commissioning measurements.

6.8. Coincidence Search between Muon- and Detector Events

If one wants to actually detect background induced by muonic events detected by the muon modules, those events need to be correlated to detector events time wise. For this purpose, the analysis code's class run was extended by the member functions TOFHist (section 4.3) and TOFMuonDet (section 4.3), where the former is used for monitor spectrometer analysis and the latter for the main spectrometer. The biggest difference is that, for the main spectrometer, runs by two DAQs leading to different starting times and different lengths are created that need to be compared. Here, the necessity for synchronization from chapter 6.7 becomes clear. Different magnetic field configurations were used that can be split into two generalized groups.

Asymmetric magnetic fields are configurations in which the magnetic field lines do not fit into the the spectrometer vessel, but are widened to hit the spectrometer wall. This way, muon induced secondary electrons are guided to the detector on cyclotron tracks around those field lines.

In non-axially symmetric configurations, the fieldlines show no rotational symmetry around

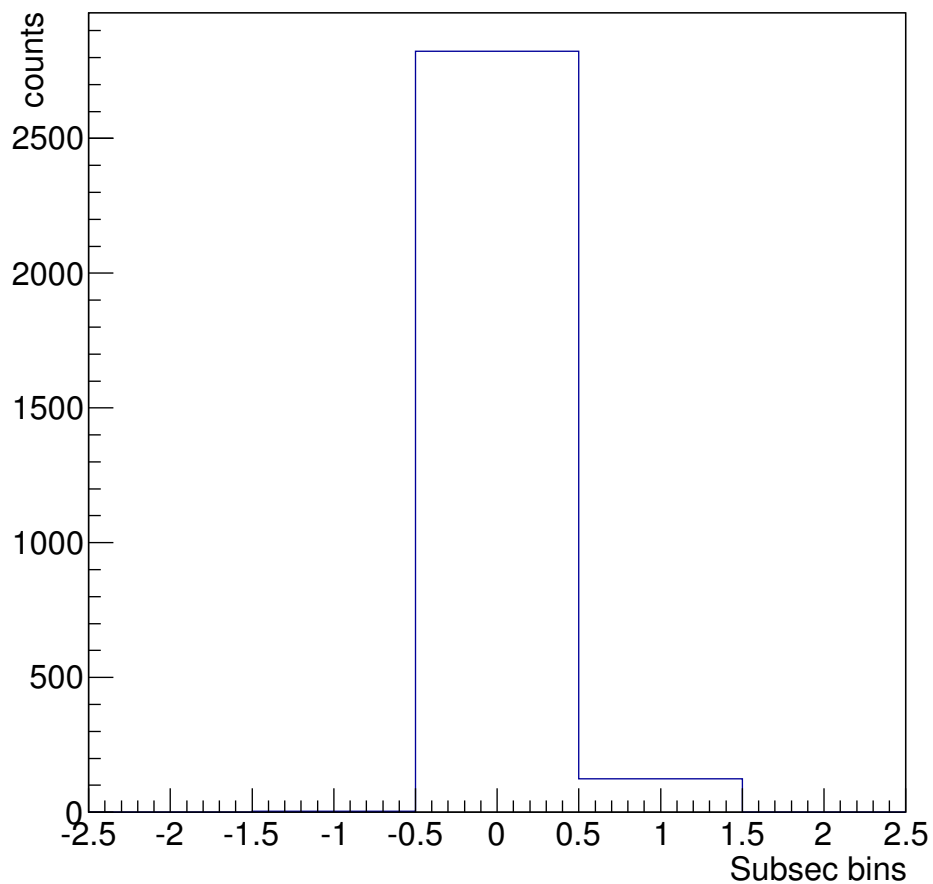


Figure 6.12.: Time differences between events after firmware upgrades. The difference in subsecond counts, i.e multiples of 50 ns is displayed. Differences between the event times are within one bin.

Settings	fpd run	myo run
Pulser voltage 250mV, freq (sampling) 100000, waveform: needle negative		
as before, but 300sec runs	4174	710
as before, but 300sec runs and energy+trace mode (sync)	4175	711
5 random pulses within 60sec run	4176	712
pulser frequency: 1 Hz, 60sec run	4177	713
pulser frequency: 10 Hz, 60sec run	4178	714
pulser frequency: 100 Hz, 60sec run	4180	715
pulser frequency: 1 kHz, 60sec run	4181	716
pulser frequency: 10 kHz, 60sec run	4182	717
Pulser:		
Pulser voltage 150mV, Freq (sampling) 1000, waveform: Pin diode negative		
5 random pulses within 60sec run	4184	719
increased thresholds from 500 to 1000 (both) pulser frequency: 1 Hz, 60sec run	4185	720
pulser frequency: 10 Hz, 60sec run	4186	721
pulser frequency: 10 Hz, 300sec run	4187	722
pulser frequency: 100 Hz, 300sec run	4188	723
pulser frequency: 10 Hz, 300sec run	4189	724
Removing Cat5 cables from synchronization clock and installing fiber optic cables + converter boxes		
pulser frequency: 0.2 Hz, 60sec run	4190	725
5 random pulses within 60sec run, both energy mode	4191	726
pulser frequency: 1 Hz, both energy mode, 60sec run	4192	727
pulser frequency: 10 Hz, both energy mode, 60sec run	4193	728
pulser frequency: 10 Hz, both energy mode, 300sec run	4194	729
pulser frequency: 100 Hz, both energy mode, 300sec run	4195	730
pulser frequency: 10 Hz, both energy+trace (sync) mode, 300sec run	4196	731

Table 6.3.: All settings including run numbers tested with the two DAQs from the detector system and the muon modules. In the leftmost column, pulser settings and run lengths are described. In front of the different parts, the pulser settings, which were kept constant for the following measurements, are described.

the z-axis. This change in fields is achieved by an additional coil on top of the monitor spectrometer vessel. At the main spectrometer, it would only be possible using the EMCS coils 2.2.7 but no measurements of that kind have been taken until now.

6.8.1. Monitor Spectrometer

Measurements at the monitor spectrometer have the advantage of a fast accessibility of all the components and the collection of data in a single run-file through the mini-crate. For measurements, high voltage supplies have been added to the monitor spectrometer rack and the muon modules were connected to a newly added second FLT-card. Readout was handled by the mini-DAQ , the new FLT card was operated in veto-mode. Gains and thresholds were easily set as only four sides had to be adjusted - compared to the 16 main spectrometer channels. The PMT tubes were operated at 1.5 kV. The detector gain and threshold settings for the 5 pixel detector have been kept at standard monitor spectrometer operation settings. The detector position though was shifted to the position at which the center pixel exhibited maximum rate and the pairs of east-west and top-bottom pixels showed comparable count rates. Furthermore, the recording mode was switched from histogram-mode to energy-mode as the timestamps for every single event were needed for analysis. Several hourly runs were taken using different magnetic field settings. Both asymmetric magnetic field (see table 6.4 and non-axially-symmetric field (see table 6.5 configurations were investigated.

The TOFHist function (chapter 4.3) has been used to analyze the data, as well as “Beans” code [75]. Both tools browse through all the muon-events detected and finds any detector event in a definable timespan after (or before) the muon-event. This can be more than one detector-event per muon-event. In all of the settings, a peak is visible at around 2 μ s. Count rates are a lot higher in the asymmetric magnetic field setup as secondary electrons are guided from their point of origin to the detector instead of mostly being magnetically shielded. In this setup, only the reflection through the rise in magnetic field on the electrons’ paths takes its toll on the rate (see section 2.1.1). As data with a lot of

Run	solenoid source	solenoid detector	inner aircoil	outer central aircoil	outer aircoil	emcs x	emcs y
mos00159395	0	25	0	-4	-4	2	-19.5
mos00159396-							
mos00159398	0	50	0	-8	-8	2	-19.5
mos00159399	0	50	0	-7	-7	2	-19.5
mos00159400	0	50	0	-6	-6	2	-19.5
mos00160713-							
mos00160717	0.1	12.5	0	-2	-2	0	0
mos00160718-							
mos00160730	0.1	12.5	0	-2	-2	0	0
mos00161105-							
mos00161107	0.1	12.5	0	-2	-2	0	0
mos00161108-							
mos00161110	0.1	25	0	-2	-2	0	0
mos00161108-							
mos00161110	0.1	25	0	-2	-2	0	0

Table 6.4.: Measurements at asymmetric magnetic fields. The source side magnet was turned off for all measurements such that the field lines directly connected the detector with the spectrometer walls.

Run mos00...	2 Horizontal loops	solenoid source	solenoid detector	inner aircoil	outer aircoil	outer cent. aircoil	EMCS x	EMCS y
161111-161125	0	25	25	6.8	-7	5	0	-14
161126-161129	+50	12.5	12.5	3.5	-3.5	2.5	0	0
161130-161133	+25	12.5	12.5	1.75	-1.75	1.25	0	0
161134-161149	-25	12.5	12.5	1.75	-1.75	1.25	0	0
161150-161155	-50	12.5	12.5	3.5	-3.5	2.5	0	0
161156-161158	0	12.5	12.5	3.5	-3.5	2.5	0	0

Table 6.5.: Measurements in energy mode at non axially symmetric magnetic field. Both solenoid and air coil currents have been changed, though always by a multiplication factor for all of them so that the ration remained the same.

different field configurations was analyzed, the major part of setups and analysis can be found in appendix E. The asymmetric magnetic field measurements show the expected behavior. With high field strengths at the wall, i.e. dense field lines, the angular acceptance is high and the peak is clearly distinguishable (see appendix E.5 and E.4). As the field strengths decrease, the peak height falls in correlation to the surrounding noise until it is indistinguishable (appendix E.2 to E.9).

Non axially symmetric setups also generally showed more muon induced counts the more deformed the field was (appendix E.10 to appendix E.21). One exception is the setup in appendix E.14 showing only few events (appendix E.15). A possible explanation here is the flux tube moving off center making electrons within the flux tube miss the detector. All in all, the mechanism of muon inducing secondary electrons that are then being guided to the detector was confirmed. And, even more importantly, the very good shielding of the symmetrical flux tube was demonstrated. Once again, the necessity of well known symmetric fields was demonstrated.

6.8.2. Main Spectrometer

The monitor-spectrometer results suggested that the time of flight was well measurable, even if on bigger scale, at the main spectrometer. So, during commissioning measurements, already parallel to first measurements “M1”, some runs with asymmetric magnetic field have been taken with switched polarity or turned off pre spectrometer magnets compared to standard setup. The data was analysed for each single ring of the FPD. Search parameters were the time slot from 0 s to 10 μ s. Data remained inconclusive at the time. The failure to find a clear runtime for electrons induced by muonic events might have been due to the combination of muon module position and the magnetic field setup. In the first measurements, the wall area covered by the flux tubes and the volume surveilled by the muon modules did not overlap very much. Furthermore, due to the very low magnetic field at the wall compared to the volume inside the detector and pinch magnet, most of the induced electrons are magnetically reflected as the maximum polar angle towards magnetic field lines θ_{max} is defined by

$$\frac{B_{min}}{B_{max}} \approx \frac{3 \times 10^{-4} \text{ T}}{4 \text{ T}} = \sin^2(\theta_{max}) \quad (6.6)$$

meaning only angles below

$$\theta < \arcsin \sqrt{\frac{B_{min}}{B_{max}}} = \arcsin \sqrt{\frac{3 \times 10^{-4} \text{ T}}{4 \text{ T}}} = 0.004^\circ \quad (6.7)$$

will be able to reach the detector. All others will be reflected and fly back to the wall to be absorbed in the conducting wall material. As a result, compared to the monitor spectrometer, where the ratio is more favorable, a smaller number of muon induced electrons arrive at the detector making long measurements a requirement for good statistics. This leads to detector rates of only around 2 cps, depending on the inner electrode voltages. At high inner electrode voltages, the rate increases strongly to 150 cps which is probably due to field emission from the electrodes. Here, the rate of events actually analyzed can be reduced by using energy cuts and excluding pixels with either known problems - for example the two defective pixels - or such covered by the misaligned flapper valve. The energies were cut below 25.6 keV and above 30.6 keV, accounting for the PAE voltage of 10 kV.

Analysis for every single pixel was not possible due to limited statistics, though it might be more conclusive as less different path lengths can contribute to a single pixel. On the other hand, after the non-central alignment of the detector has been fixed using different



Figure 6.13.: A photograph of modules 1 and 2 after being moved into a position observing the steep cone rather than the central spectrometer part.

settings for the LFCS-system, the fields should be rotationally symmetric around the z-axis disregarding small deviations. Under this assumption, the path lengths for every pixel of one ring should be very comparable.

In the anticipation of better results, different field configurations were used. One widened the flux tube so the coverages of the volume surveilled by the muon detectors and the flux tube got larger (see figure 6.15). The second configuration also increased the field line density in the area of the muon modules. This again raised the probability to see electrons from detected muons at the FPD, but also raised the angular acceptance by increasing the magnetic field at the walls by a factor of two (see figure 6.16). All in all, three different magnetic field configurations were used, which are shown in figures 6.14, 6.15, 6.16 and described in tables 6.7 and 6.6.

To raise the overall acceptance of the muon induced events, these measurements were repeated with the main vessel on high voltage of -18.6 kV accelerating all the electrons towards the FPD. This was done for measurements “C” (table 6.6). The setup was changed as the flux tube was returned to its initial setting (figure 6.14) but the muon modules were moved towards the steep cone now surveilling exactly the region of interest (figure 6.13).

None of the settings showed time peaks as clear as the monitor spectrometer. Simulations of single events show that the fastest particles arrive after times comparable to the ones of the monitor spectrometer, i.e. at $1.5\text{ }\mu\text{s}$ (figure 6.17). This already poses a problem. The anticipated rate of muons through the area of the main spectrometer covered by the flux tube is

$$r_\mu A_{MS} = 1/\text{cm}^2 \cdot 66 \text{ m}^2 = 660\,000 \text{ s}^{-1} \quad (6.8)$$

where the area covered by the flux tube is taken from [77]. This means that the average time between muon events of $1/660\,000 \text{ s} \approx 1.5\text{ }\mu\text{s}$ is of equal size as the time of flight for a single electron. This of course makes it difficult to distinguish between the different events. The measurements with field setting “C” were not as promising as previously thought despite the larger acceptance angle. The ones on high voltage showed a lot higher rates,

Table 6.6.: Main spectrometer runs taken for the search of muon induced background events. The runs are split into groups of identical magnetic field settings. The individual settings are listed in table 6.7. All group members have different inner electrode voltages, refer to appendix for those as well.

measurement setting	myo		fpd	
	start	end	start	end
A1	5159	5164	939	949
	5166	5172	950	977
B	5255	5256	1052	1055
A2	6306	6307	1090	1096
	6308	6311	1097	1104
	6312	6315	1105	1112
	6316	6321	1113	1124
	6322	6327	1125	1136
	6328	6333	1137	1148
C	6401	6404	1226	1229
	6405	6408	1230	1233
	6409	6412	1234	1237
A3	7111	7134	1301	1325

Table 6.7.: Magnetic field settings for the individual groups from table 6.6.

Measurement setting	IE[V]	PS I [T]	PS II [T]	Pinch [T]	Det [T]	LFCs [A]	EMCS h [A]	EMCS v [A]
A1, A2, A3	-700	0	0	5	3.5	#1 - #13: 100 A; #14: 0 A	50	9
B	0	0	0	5	3.5	#1 - #3: 0 A; #4: 50 A; #5 - #13: 100 A; #14: 0 A	50	9
C	-600	0	0	5	3.5	#1 & #2: -50 A; #3: 0 A; #4 - #13: 100 A #14: 70 A	40	9

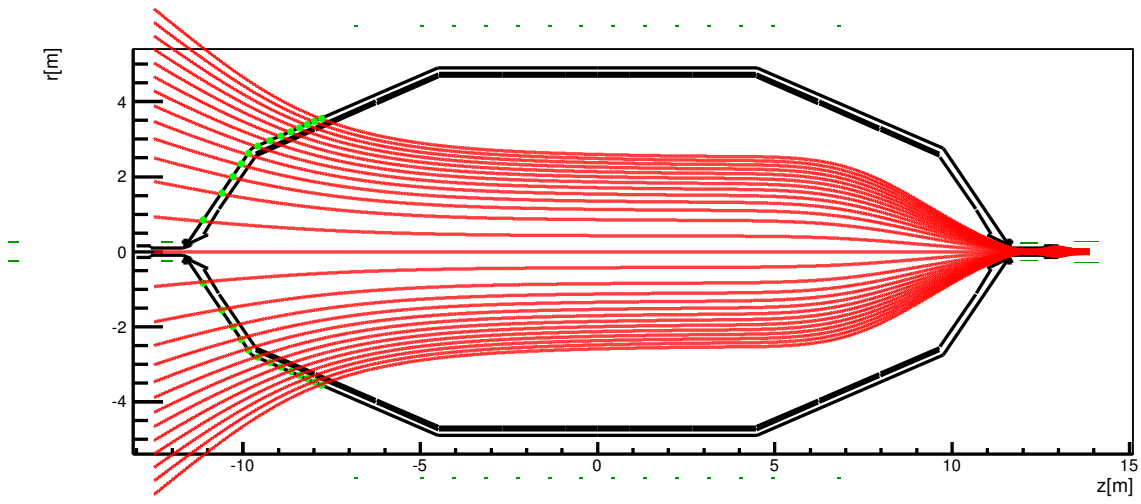


Figure 6.14.: First used magnetic field setup. Note that the largest part of the flux tube is in the area of the steep cone. With the initial positions of the muon modules, the probability of the detected muons having caused secondary electrons inside the flux tube was too low.

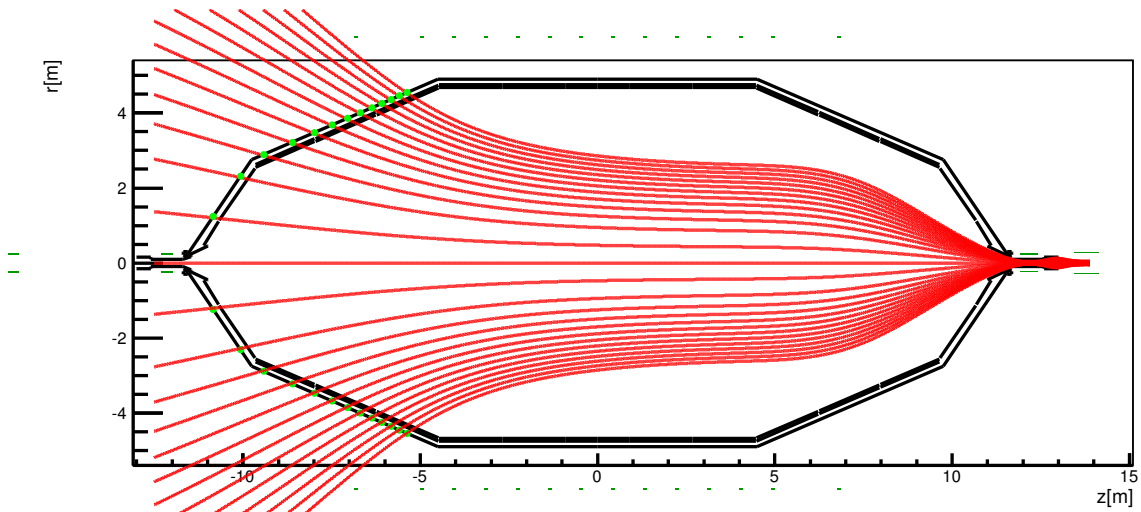


Figure 6.15.: Widened magnetic flux tube for better coverage by the muon modules. The flat cone is now almost completely covered.

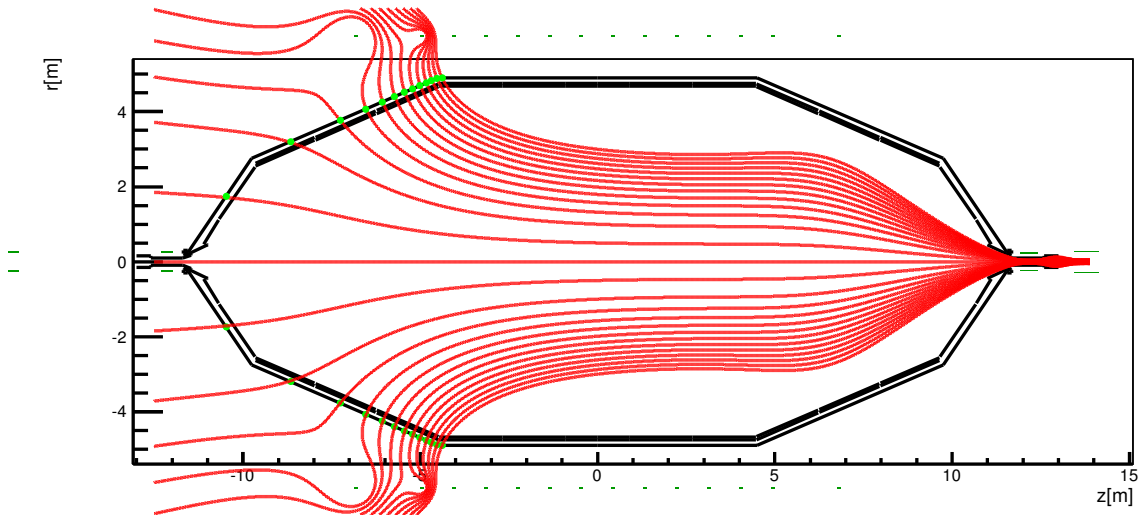


Figure 6.16.: Flux tube as proposed in [76]. Here, two LFCS coils on the source side were operated with switched polarity. This creates a denser flux tube in the region of interest.

though a lot of this effect may be attributed to field emission. There are runs in which one could identify peaks at the position of the simulation, though all of these are small compared to ambient signals. The most prominent one is displayed in figure 6.18. It could be interpreted as a signal peak with a exponential tail. This remains very speculative at the moment. Further measurements with magnetic field setups reducing the overall area of the flux tube covered might shed more light on this. Sadly, as the time of the commissioning measurements was limited, these have to be taken at a later date.

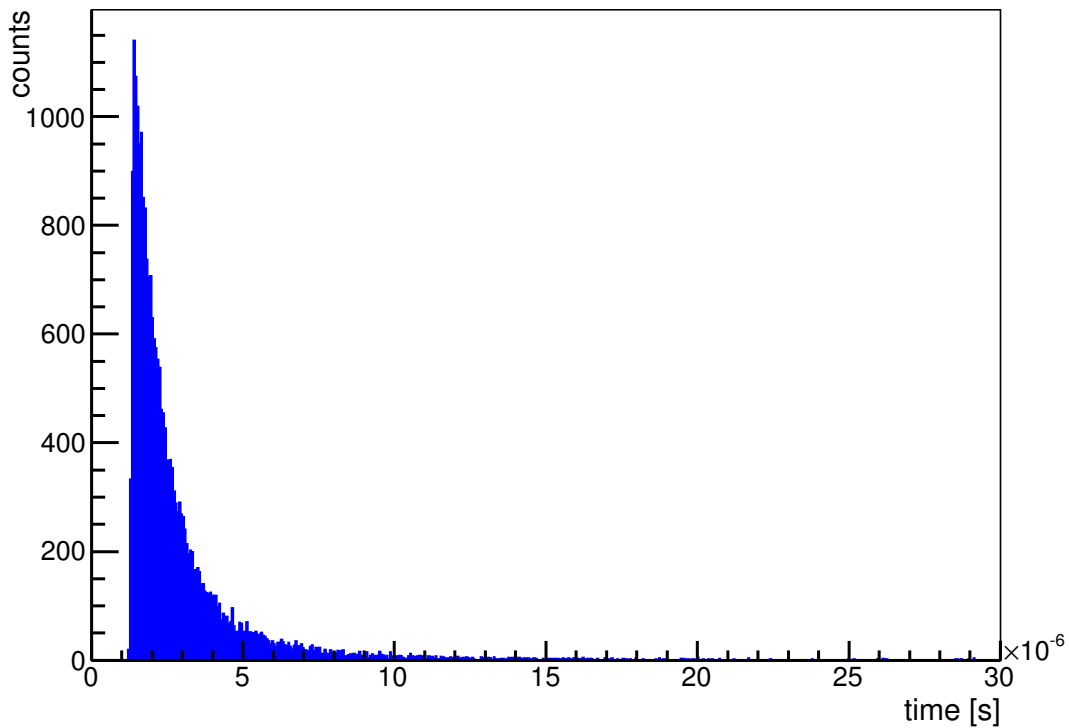


Figure 6.17.: Time of flight for simulated electrons starting at the spectrometer wall. The “fastest” electron arrives at $1.5 \mu\text{s}$. The distribution has an exponential character.

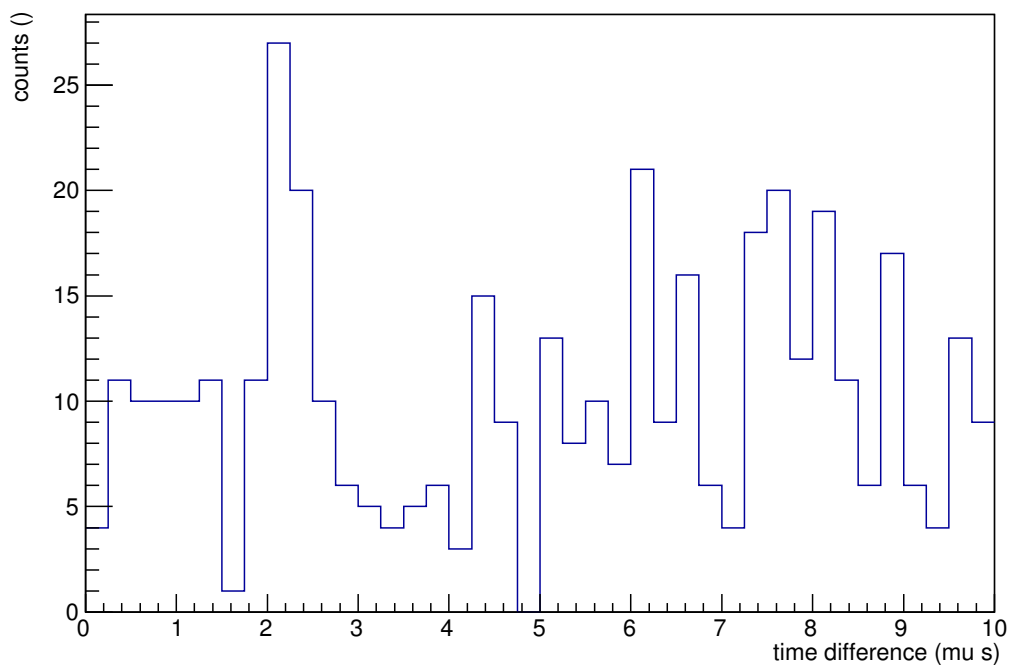


Figure 6.18.: The mos promising result so far for the main spectrometer. The peak at around $2 \mu\text{s}$ resembles the simulation with its exponential tail. The counts before after might already be other muon induced events.

7. Conclusion & Outlook

The KATRIN experiment is progressing on its journey to determine the absolute neutrino mass scale - and another part contributing to the whole experiment has been completed with the muon detection system operational and taking data. At the main spectrometer, set up has been completed. The monitor spectrometer system was readopted. Both systems are able to take data at rates that compare well to literature values and simulations. Many settings had to be adjusted for the detection system to realize its full potential. High voltage supplies were installed, software settings within the ORCA software were adapted to the system's needs and synchronization with the FPD was set up. In the commissioning phase for the muon detection system, different tests were performed to ensure a smoothly working system. The single PMTs were tested with a Sr source revealing two sides showing lower rates than the rest. This was compensated for by raising acceleration voltages for the affected sides. The stability of the system was investigated. It was found that natural atmospheric fluctuations cause much larger rate fluctuations than the module electronics. The efficiency of the single modules was examined and found to be $(93.4 \pm 3.4)\%$. The module's rates compare very well to literature values.

It was shown that the muon induced electron rate at a spectrometer of the MAC-E filter type is well shielded by axially symmetric magnetic fields and that, under different conditions, this rate increases strongly. This proved that the great efforts invested to achieve accurate field knowledge and settings are necessary and will be rewarded with low background measurements. Analysis with both asymmetric and non axially symmetric fields were very successful showing that all induced events show similar times of flight from the vessel wall to the detector. At the main spectrometer, the setup still needs to be optimized. Due to the limited measurement time in the now completed first SDS commissioning measurement phase, further investigations were not possible but will be performed in the future.

Bibliography

- [1] E. Fermi. Versuch einer theorie der β strahlen. 1934. [Online, accessed 06-09-2013].
- [2] C. L. Cowan, F. Reines, F. B. Harrison, H. W. Kruse, and A. D. McGuire. Detection of the free neutrino: a confirmation. *Science*, 124(3211):103–104, 1956. [Online, accessed 06-09-2013].
- [3] G. Danby, J-M. Gaillard, K. Goulian, et al. Observation of high-energy neutrino reactions and the existence of two kinds of neutrinos. *Phys. Rev. Lett.*, 9:36–44, Jul 1962.
- [4] K. Kodama, N. Ushida, C. Andreopoulos, et al. Observation of tau neutrino interactions. *Physics Letters B*, 504(3):218 – 224, 2001.
- [5] Claus Grupen. *Astroparticle Physics*. Springer, Berlin [u.a.], 1. ed. edition, 2005.
- [6] F. M. Fraenkle. Background investigations of the katrin pre-spectrometer. <http://digbib.ubka.uni-karlsruhe.de/volltexte/1000019392>, 2010.
- [7] Bethge and Walter. *Kernphysik*. Springer, 2006.
- [8] F.P. An et al. Observation of electron-antineutrino disappearance at daya bay. *Phys. Rev. Lett.* 108, 108, 2012.
- [9] S. Chatrchyan, V. Khachatryan, A.M. Sirunyan, et al. Observation of a new boson at a mass of 125 gev with the {CMS} experiment at the {LHC}. *Physics Letters B*, 716(1):30 – 61, 2012.
- [10] G. Aad, T. Abajyan, B. Abbott, et al. Observation of a new particle in the search for the standard model higgs boson with the atlas detector at the lhc. *Physics Letters B*, 716(1):1 – 29, 2012.
- [11] W. Rodejohann. standard model elementary particles. http://www.mpi-hd.mpg.de/manitop/StandardModel/pics/standard_model_elementary_particles.png, 2013. [Online, accessed 05-09-2013].
- [12] Bogdan Povh, Klaus Rith, Christoph Scholz, and Frank Zetsche, editors. *Teilchen und Kerne : Eine Einfuehrung in die physikalischen Konzepte*. Springer-LehrbuchSpringerLink : BÄcher. Springer Berlin Heidelberg, Berlin, Heidelberg, 8 edition, 2009.
- [13] M. Ageron et al. ANTARES: the first undersea neutrino telescope. *Nucl.Instrum.Meth.*, A656:11–38, 2011.
- [14] K. et al Abe. Evidence for the appearance of atmospheric tau neutrinos in super-kamiokande. *Phys. Rev. Lett.*, 110:181802, May 2013.
- [15] M.G. Aartsen et al. Measurement of the Atmospheric ν_e flux in IceCube. *Phys.Rev.Lett.*, 110:151105, 2013.

- [16] Zhou Bin, Ruan Xi-Chao, Nie Yang-Bo, Zhou Zu-Ying, et al. A study of antineutrino spectra from spent nuclear fuel at daya bay. *Chinese Physics C*, 36(1):1, 2012.
- [17] M. Maltoni, T. Schwetz, M. A. Tórtola, and J. W. F. Valle. Status of three-neutrino oscillations after the sno-salt data. *Phys. Rev. D*, 68:113010, Dec 2003.
- [18] scienceblogs.com. Neutino mass hierarchy. <http://scienceblogs.com/startswithabang/files/2012/01/mass-hierarchy.jpg>, 2012. [Online; accessed 21-08-2013].
- [19] R. Davis. A review of the Homestake solar neutrino experiment. *Prog.Part.Nucl.Phys.*, 32:13–32, 1994.
- [20] J. Beringer et al. 2012 review of particle physics. *Phys. Rev. D86*, 010001, 2012.
- [21] Michael Wurm et al. The next-generation liquid-scintillator neutrino observatory LENA. *Astropart.Phys.*, 35:685–732, 2012.
- [22] G. Drexlin, V. Hannen, S. Mertens, and C. Weinheimer. Current Direct Neutrino Mass Experiments. *ArXiv e-prints*, June 2013.
- [23] Beth A. Reid et al. Cosmological Constraints from the Clustering of the Sloan Digital Sky Survey DR7 Luminous Red Galaxies. *Mon.Not.Roy.Astron.Soc.*, 404:60–85, 2010.
- [24] E. Komatsu, Smith, et al. Seven-year Wilkinson Microwave Anisotropy Probe (WMAP) Observations: Cosmological Interpretation. *apjs*, 192:18, February 2011.
- [25] P.A.R. Ade et al. Planck 2013 results. XVI. Cosmological parameters. 2013.
- [26] D. A. Knapp R. G. H. Robertson. Direct measurements of neutrino mass. *Annual Review of Nuclear Science*, 1988.
- [27] E. Andreotti, C. Arnaboldi, et al. Mare, microcalorimeter arrays for a rhenium experiment: A detector overview. *Nuclear Instruments and Methods in Physics Research Section A: Accelerators, Spectrometers, Detectors and Associated Equipment*, 572(1):208 – 210, 2007. Frontier Detectors for Frontier Physics - Proceedings of the 10th Pisa Meeting on Advanced Detectors.
- [28] Todor Stanev. *High energy cosmic rays : with 19 tab.* Springer-Praxis books in astrophysics and astronomy. Springer, Berlin, 2. ed. edition, 2004. 2010 nochmals eine 2. ed. erschienen.
- [29] Anais Schaeffer. http://cds.cern.ch/record/1345733/files/Cosmic_image.jpg, 2013. [Online; accessed 01-09-2013].
- [30] S. Hayakawa. *Cosmic ray physics. Nuclear and astrophysical aspects.* 1969.
- [31] T. P. Gorringe. MuLan Measurement of the Positive Muon Lifetime and Determination of the Fermi Constant. *ArXiv e-prints*, January 2013.
- [32] P. Doll, W. D. Apel, J. C. Arteaga, and et al. Muon Production Height in the Air-Shower Experiment KASCADE-Grande. In *International Cosmic Ray Conference*, volume 4 of *International Cosmic Ray Conference*, pages 115–118, 2008.
- [33] E.W. Otten and C. Weinheimer. Neutrino mass limit from tritium beta decay. *Rept.Prog.Phys.*, 71:086201, 2008.
- [34] J. Wolf. The katrin neutrino mass experiment. *Nuclear Instruments and Methods in Physics Research Section A: Accelerators, Spectrometers, Detectors and Associated Equipment*, 623(1):442 – 444, 2010.

- [35] KATRIN. Mac e filter. http://www.katrin.kit.edu/img/mace_electrodes_rdx_1200x1200.gif, 2006.
- [36] Markus Steidl. <http://www.katrin.kit.edu/79.php>, 2011. [Online, accesse 18-09-2013].
- [37] Lyndsay. http://www.astro.gla.ac.uk/users/lyndsay/TEACHING/NLPII/Lecture4_06.pdf, 2006. [Online, accesse 18-09-2013].
- [38] A. Osipowicza, H. Blueumer, G. Drexlin, K. Eitel, et al. Katrin: A next generation tritium beta decay experimentwith sub-ev sensitivity for the electron neutrino mass. 2002. [Online, accessed 16-09-2013].
- [39] S. Grohmann, T. Bode, M. HÄtzel, et al. The thermal behaviour of the tritium source in {KATRIN}. *Cryogenics*, 55â56(0):5 – 11, 2013.
- [40] Magnus Schlässer, Simone Rupp, Hendrik Seitz, Sebastian Fischer, et al. Accurate calibration of the laser raman system for the karlsruhe tritium neutrino experiment. *Journal of Molecular Structure*, 1044(0):61 – 66, 2013. <ce:title>EUCMOS XXXI</ce:title> <ce:subtitle>EUCMOS XXXI</ce:subtitle>.
- [41] M. Babutzka. 24th katrin collaboration meeting - status of the rearsection. <http://fuzzy.fzk.de/bscw/bscw.cgi/d847077/95-TRP-5401-S1-MBabutzka.pptx>, 2013. [Online; accessed 01-09-2013].
- [42] G. Drexlin. Wgts. <http://fuzzy.fzk.de/bscw/bscw.cgi/d736434/95-TRP-5205-S2-GDrexlin.pptx>, 2012.
- [43] F. Priester. 24th katrin collaboration meeting - tritium test experiments. <http://fuzzy.fzk.de/bscw/bscw.cgi/d774076/95-TRP-5403-S1-FPriester.pptx>, 2013. [Online; accessed 01-09-2013].
- [44] L. Bornschein. 24th katrin collaboration meeting - status of dps. <http://fuzzy.fzk.de/bscw/bscw.cgi/d774094/95-TRP-5405-S2-LBornstein.ppt>, 2013. [Online; accessed 01-09-2013].
- [45] W. Gil. 24th katrin collaboration meeting - status of cryogenic pumping section. <http://fuzzy.fzk.de/bscw/bscw.cgi/d774107/95-TRP-5406-S2-WGIL.pptx>, 2013. [Online; accessed 01-09-2013].
- [46] Joachim Wolf. Status of the pre-spectrometer of the katrin experiment. http://www.katrin.kit.edu/publikationen/talk_DPG-2004-03-11-prespec.pdf, 2004. [Online, accessed 17-09-2013].
- [47] K. Valerius. Electromagnetic design and inner electrode for the katrin main spectrometer. *Progress in Particle and Nuclear Physics*, 57(1):58 – 60, 2006.
- [48] Th Thümmler, R Marx, and Ch Weinheimer. Precision high voltage divider for the katrin experiment. *New Journal of Physics*, 11(10):103007, 2009.
- [49] K. Valerius. The wire electrode system for the {KATRIN} main spectrometer. *Progress in Particle and Nuclear Physics*, 64(2):291 – 293, 2010.
- [50] T. Thümmler. 24th katrin collaboration meeting - sds status & spectrometer bake-out. <http://fuzzy.fzk.de/bscw/bscw.cgi/d774576/95-TRP-5409-S3-TThuemmler.pdf>, 2013. [Online; accessed 01-09-2013].
- [51] M. Zacher. 20th katrin collaboration meeting - wire electrode system installation status. <http://fuzzy.fzk.de/bscw/bscw.cgi/d694360/95-TRP-5006-S2-MZacher.pdf>, 2011. [Online; accessed 01-09-2013].

- [52] J. Schwarz. 24th katrin collaboration meeting - the focal-plane detector system. <http://fuzzy.fzk.de/bscw/bscw.cgi/d774296/95-TRP-5414-S4-JSchwarz.pdf>, 2013. [Online; accessed 01-09-2013].
- [53] F. Glück et al. Air coil system & magnetic field sensor system. <http://fuzzy.fzk.de/bscw/bscw.cgi/d530439/Air%20Coil%20System%20and%20Magnetic%20Field%20Sensor%20System.pdf>, 2009. [Online; accessed 24-08-2013].
- [54] S. Mertens, G. Drexlin, F.M. Fränkle, et al. Background due to stored electrons following nuclear decays in the {KATRIN} spectrometers and its impact on the neutrino mass sensitivity. *Astroparticle Physics*, 41(0):52 – 62, 2013.
- [55] S. Görhardt. Reduktion der durch radon induzierten untergrundprozesse in den katrin spektrometern. <http://www.katrin.kit.edu/publikationen/dth-goerhardt.pdf>, 2010. [Online; accessed 27-08-2013].
- [56] F.M. Fränkle, L. Bornschein, G. Drexlin, et al. Radon induced background processes in the katrin pre-spectrometer. *Astroparticle Physics*, 35(3):128 – 134, 2011.
- [57] Howe, M. A. et al. Tunl progress report. *TUNL Progress Report*, XLVIII:179, 2009.
- [58] Norman Haussmann. <http://www.katrin.kit.edu/publikationen/dth-Haussmann.pdf>, 2013.
- [59] Saint-Gobain Crystals. Premium plastic scintillators. http://www.detectors.saint-gobain.com/uploadedFiles/SGdetectors/Documents/Product_Data_Sheets/BC400-404-408-412-416-Data-Sheet.pdf, 2005. [Online; accessed 11-07-2013].
- [60] J. Reichenbacher, 1997.
- [61] Philips Components. *photomultiplier tubes - principles and application*. 1990.
- [62] I. Antcheva, M. Ballintijn, B. Bellenot, et al. {ROOT} à a c++ framework for petabyte data storage, statistical analysis and visualization. *Computer Physics Communications*, 180(12):2499 – 2512, 2009. <ce:title>40 {YEARS} {OF} CPC: A celebratory issue focused on quality software for high performance, grid and novel computing architectures</ce:title>.
- [63] S. Agostinelli, J. Allison, K. Amako, et al. Geant4 - a simulation toolkit. *Nuclear Instruments and Methods in Physics Research Section A: Accelerators, Spectrometers, Detectors and Associated Equipment*, 506(3):250 – 303, 2003.
- [64] Benjamin Jung. Simulation des myon-induzierten untergrundes und dessen speicherwahrscheinlichkeit am katrin hauptspektrometer, 2011.
- [65] Henrik Arlinghaus. Investigation of the muon-induced secondary electron background in the katrin experiment. http://www.uni-muenster.de/Physik.KP/AGWeinheimer/Files/theses/Diplom_Henrik_Arlinghaus.pdf, 2009. [Online; accessed 21-08-2013].
- [66] S.I. Klimushin, E.V. Bugaev, and Igor A. Sokalski. On the parametrization of atmospheric muon angular flux underwater. *Phys.Rev.*, D64:014016, 2001.
- [67] Kevin Wierman. personal conversation, 2013.
- [68] W.-M. Yao et al. Review of particle physics. *J. Phys. G* 33, 2006.
- [69] Nancy Wandkowsky. Study of background and transmission properties of the katrin spectrometers. <http://fuzzy.fzk.de/bscw/bscw.cgi/d847562/phd-wandkowsky.pdf>.

- [70] Myer Kutz. *Eshbach's Handbook of Engineering Fundamanetals*. Wiley, 2009.
- [71] T. Tsang. *Classical Electrodynamics*. Advanced Series on Theoretical Physical Sciences. World Scientific, 1997.
- [72] O.C. Allkofer. *Introduction to cosmic radiation*. Karl Thiemig, 1975.
- [73] Manfred Kleemann. pressure and temperature data from wetter.com. http://www.wetter.com/wetter_aktuell/rueckblick/?id=DE0005309, 2012.
- [74] N. Ramesh, M. Hawron, C. Martin, and A. Bachri. Flux Variation of Cosmic Muons. *ArXiv e-prints*, March 2012.
- [75] Near-time / real-time analysis tools for the detector system. <http://fuzzy.fzk.de/bscw/bscw.cgi/d751550/95-TRP-5364-S6-SEnomotoanshiro.pdf>, 2012.
- [76] M. Asda. Katrin sds measurements - proposal m12. <http://www.katrin.kit.edu>, 2013.
- [77] T. J. Corona, F.M. Fraenkle, B. Leiber, et al. M6 - secondary emission at zero electric tank potential. https://nuserv.uni-muenster.de/svn/katrin/SDS_commissioning/CommissioningDocument/M6/.
- [78] Andreas Kosmider. Tritium retention techniques in the katrin transport section and commissioning of its dps2-f cryostat. <http://digbib.ubka.uni-karlsruhe.de/volltexte/1000028959>, 2012. [Online, accessed 26-09-2013].

Annex

A. ORCA air coil script

```
// import functions for SDS hardware access

#import "~/katrin/ORCARunControl/libs/SDS_RunControl.lib"

#import "~/katrin/ORCARunControl/libs/SDS_AirCoils.lib"

function main(){

//ramp through tenths of the maximum air coil values

for(a=0;a<11; a++){

max=70;

//queue coils 1, 13 and 14 (70A max)

queueAirCoilCurrent_A(1,a*max/10);

queueAirCoilCurrent_A(13,a*max/10);

queueAirCoilCurrent_A(14,a*max/10);

max=100;

//queue coils 2 - 12 (100A max)

for(i=2;i<13;i++){

queueAirCoilCurrent_A(i, a*max/10);

}

//set queued values

sendQueue();

//wait till set
```

```
sleep(300);

//output of values

print readAllAirCoilCurrents_A();

sleep(1500);

}

// send the queue of all set points

}

\label{}
```

B. Connection scheme DAQ & high voltage settings

V0	I0	I1	V1	Ramp Up	Ramp Down
1.5 kV or 1.6 kV	2000 mA			50 V	100 V

Table B.1.: High voltage settings as used for the muon modules. Modules XX and XX are set to 1.6 kV.

Module	1A	1B	2A	2B	3A	3B	4A	4B
Card	3	3	3	3	6	6	6	6
Channel	0	14	3	7	0	14	3	7
HV	W0	W1	W2	W3	W4	W5	W6	W7
Module	5A	5B	6A	6B	7A	7B	8A	8B
Card	6	6	8	8	8	8	8	8
Channel	9	23	0	14	3	7	9	23
HV	W8	W9	E0	E1	E2	E3	E4	E5

Table B.2.: Assignment of main spectrometer module sides to FLT cards and their channels.

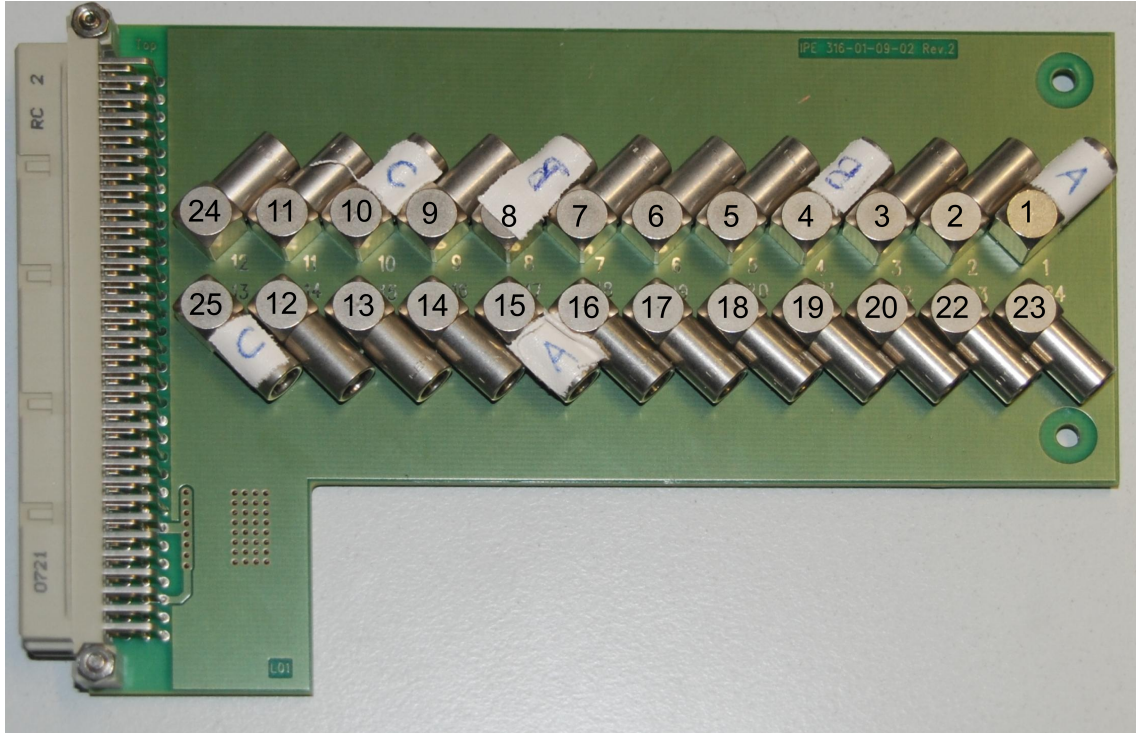


Figure B.1.: One of the connector cards used at the muon DAQ. The overlaid numbers correspond to the channels accessed via the corresponding connector. Note the non trivial behaviour on the left end. The white labels A, B and C mark the channels used for connecting the muon modules.

C. Weather data Christmas 2012

Date	T _{low} [K]	T _{high} [K]	p _{low} [kPa]	p _{high} [kPa]	p _l / T _l	p _h / T _h
21.12.12	274.95	281.25	1010.10	1018.20	3.67	3.62
22.12.12	278.55	282.15	1009.50	1020.60	3.62	3.62
23.12.12	282.85	287.25	1009.50	1013.70	3.57	3.53
24.12.12	277.05	287.15	1007.40	1013.50	3.64	3.53
25.12.12	276.05	288.35	1004.00	1010.30	3.64	3.50
26.12.12	281.25	282.85	1010.40	1016.40	3.59	3.59
27.12.12	280.75	283.25	1004.80	1014.70	3.58	3.58
28.12.12	279.65	281.85	1016.20	1029.50	3.63	3.65
29.12.12	276.05	284.55	1014.90	1026.00	3.68	3.61
30.12.12	279.05	282.85	1015.90	1024.60	3.64	3.62
31.12.12	277.05	283.15	1011.60	1024.40	3.65	3.62
01.01.13	274.45	281.45	1008.10	1016.90	3.67	3.61
02.01.13	272.25	279.15	1017.50	1033.00	3.74	3.70
03.01.13	273.65	280.45	1033.10	1038.30	3.78	3.70

Table C.3.: Temperature and pressure data from the weather station in Rheinstetten. Daily high and low were given, included are the ratio of pressure and temperature for both the high and the low values. This ratio is proportional to the air's density . Bare in mind that this data is only for the low atmospheric layer and the station is also around 20 km away from the KATRIN muon modules.

D. Other monitor spectrometer settings

non-axially symmetric magnetic field

solenoid source	solenoid detector	inner aircoil	outer aircoil	outer cent. aircoil	emcs x	emcs y
25	25	7	-7	5	0	-14
mos00159753- mos00159754	Two horizontal loops at 100 A					
mos00159755- mos00159758	Two horizontal loops at -100 A					
mos00159759- mos00159771	No current in horizontal loops - background measurement					
mos00159772- mos00159773	Two horizontal loops at 100 A					

solenoid source	solenoid detector	inner aircoil	outer aircoil	outer cent. aircoil	emcs x	emcs y
12.5	12.5	3.5	-3.5	2.5	0	0
mos00160661- mos00160666	Two horizontal loops at 50 A					
mos00160667- mos00160682	No current in horizontal loops - background measurement					
mos00160684- mos00160687	Two horizontal loops at -50 A					

solenoid source	solenoid detector	inner aircoil	outer aircoil	outer cent. aircoil	emcs x	emcs y
6.2	6.2	1.7	-1.7	1.2	0	0
mos00160688- mos00160691	Two horizontal loops at 25 A					
mos00160692- mos00160706	No current in horizontal loops - background measurement					
mos00160707- mos00160711	Two horizontal loops at -25 A					

E. Monitor spectrometer field setup and analysis

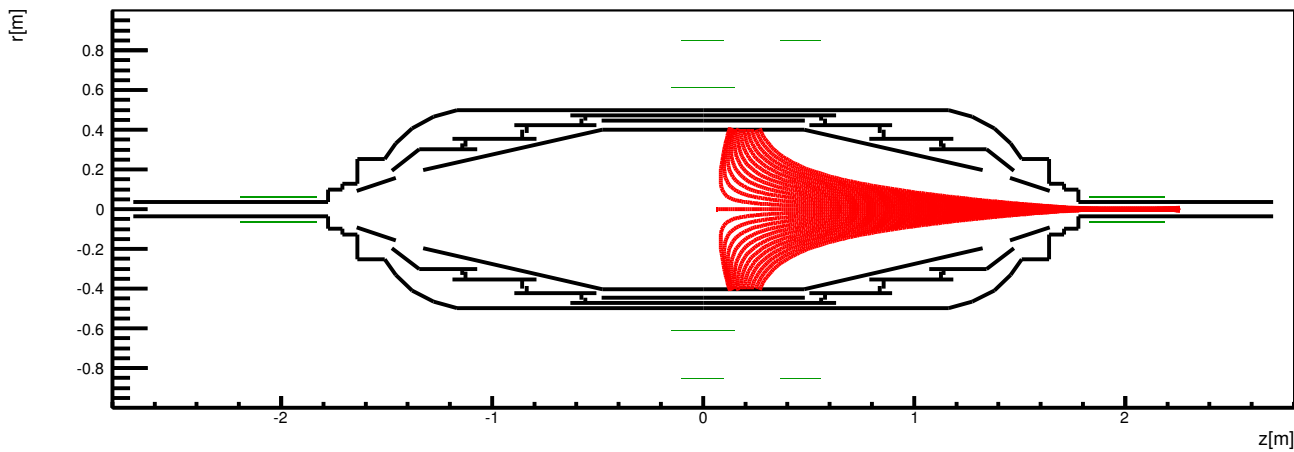


Figure E.2.: Flux tube for a 50 A detector solenoid, -8 A outer central air coil current.

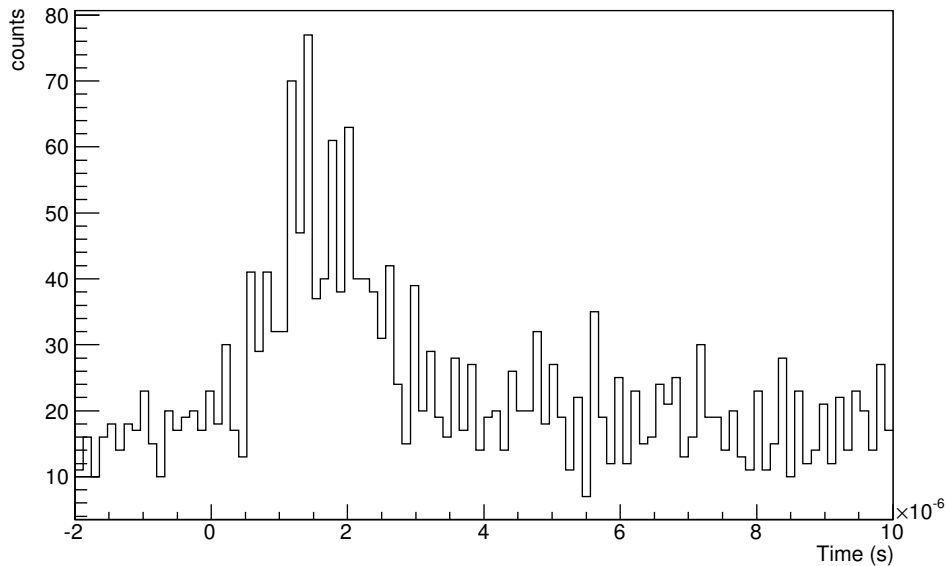


Figure E.3.: Source solenoid off, detector solenoid at 25 A. A peak in time is visible at $1.8 \mu\text{s}$.

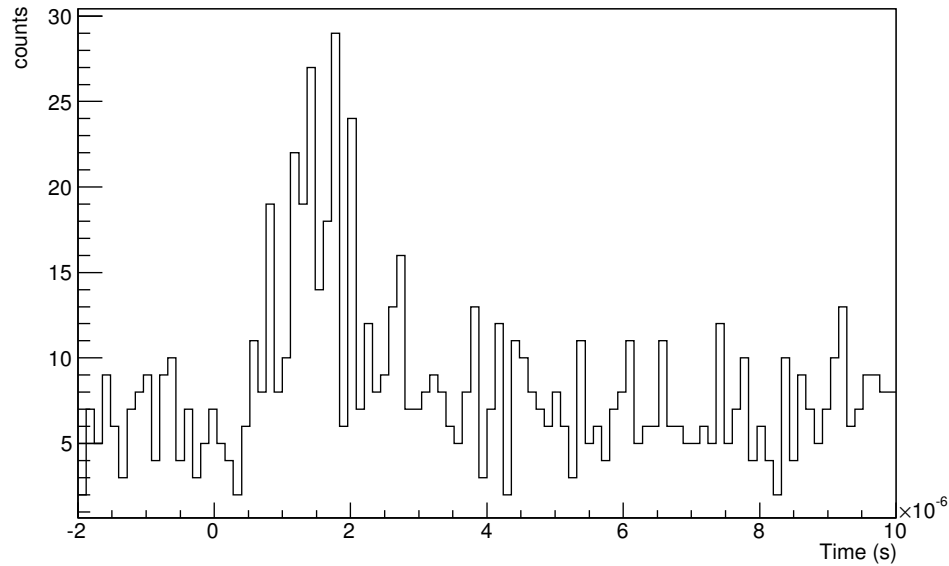


Figure E.5.: Source solenoid off, detector solenoid at 25 A

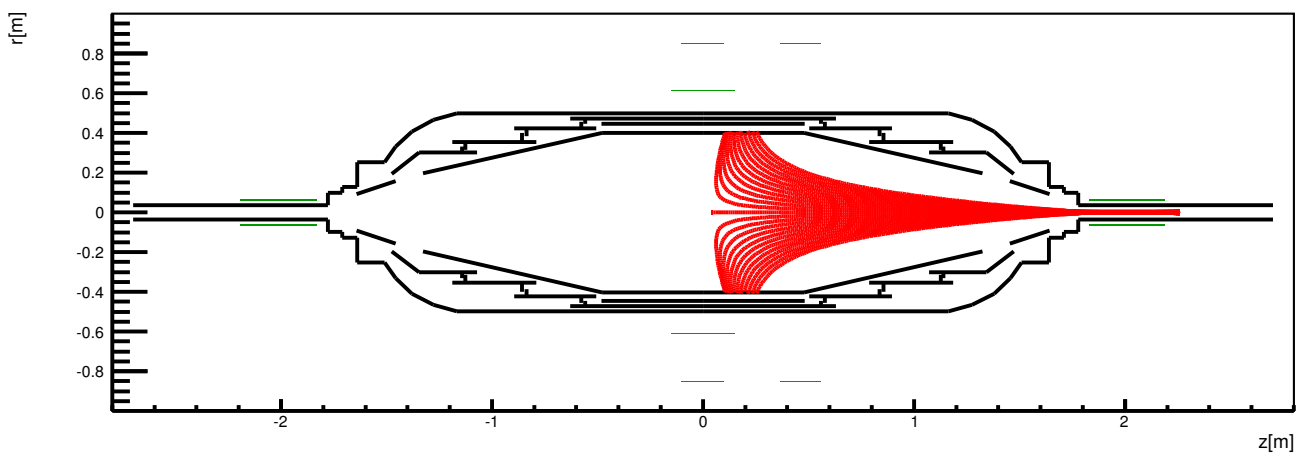


Figure E.4.: Flux tube for a 25 A detector solenoid.

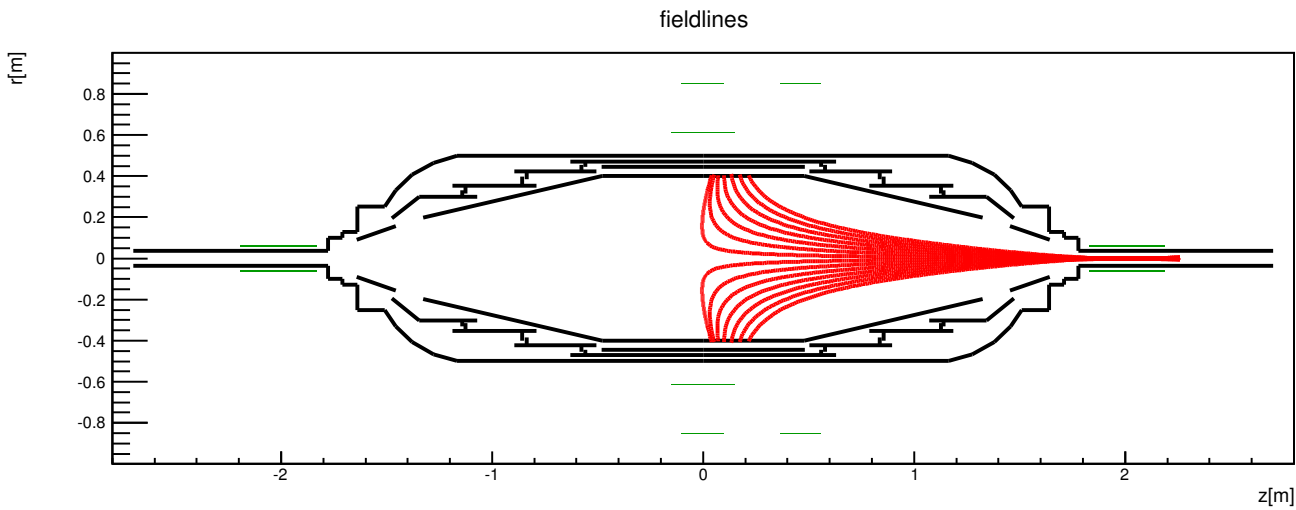


Figure E.6.: Flux tube for a 50 A detector solenoid, -7 A outer central air coil current.

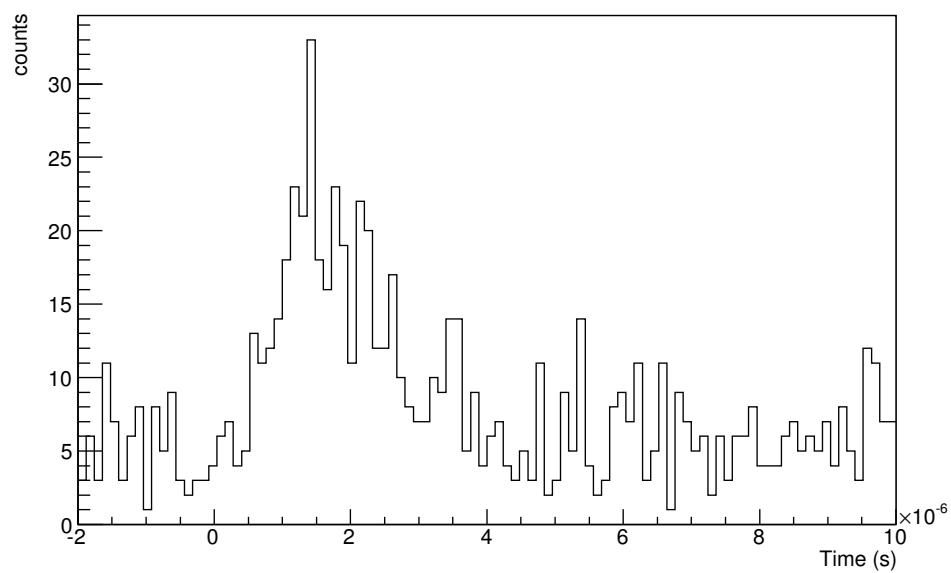


Figure E.7.: Two horizontal loops at 0 A current. Both solenoids at 25 A.

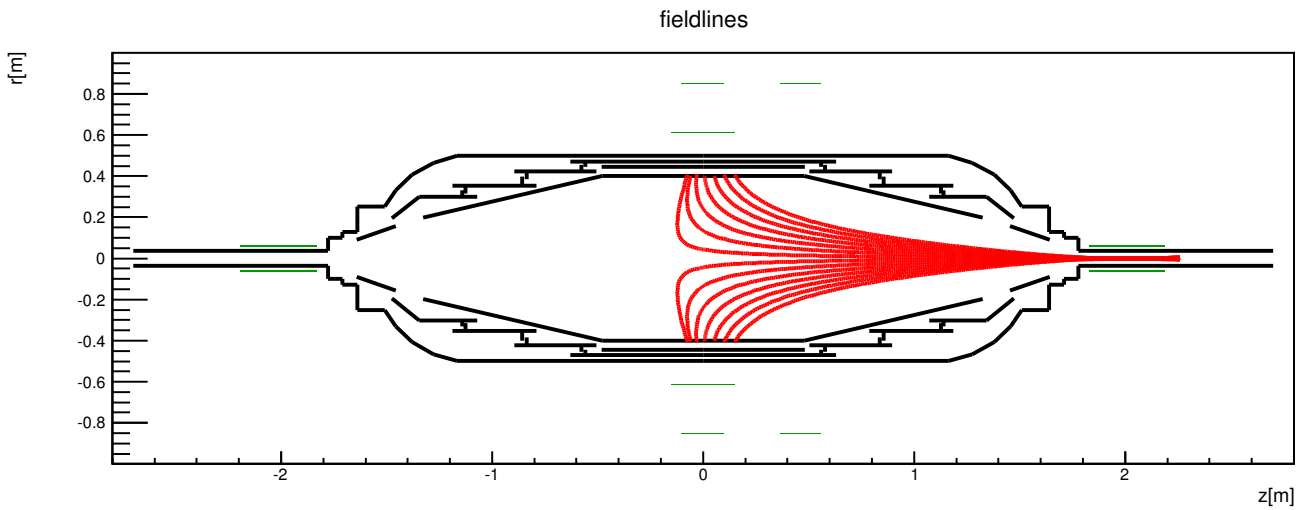


Figure E.8.: Flux tube for a 50 A detector solenoid, -6 A outer central air coil current.

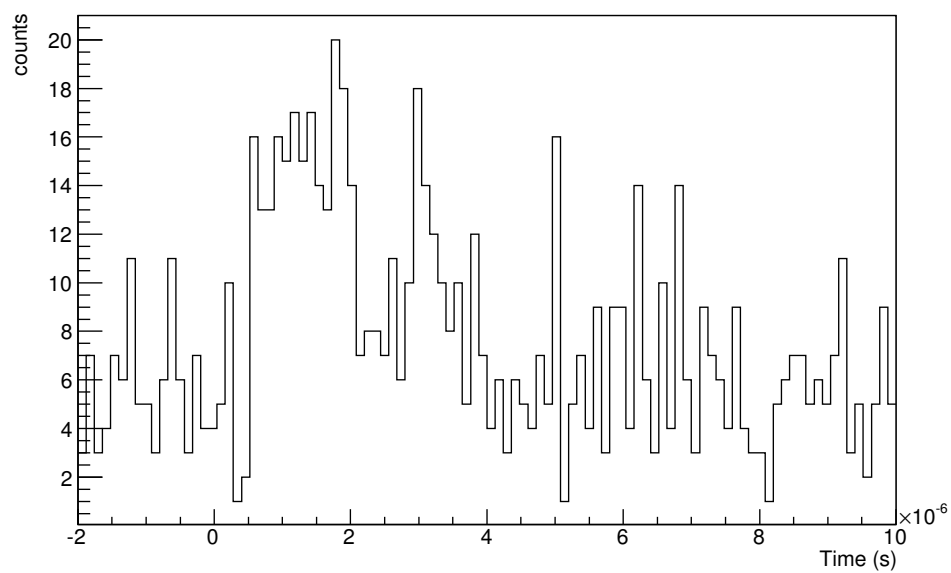


Figure E.9.: Two horizontal loops at 0 A current. Both solenoids at 25 A.

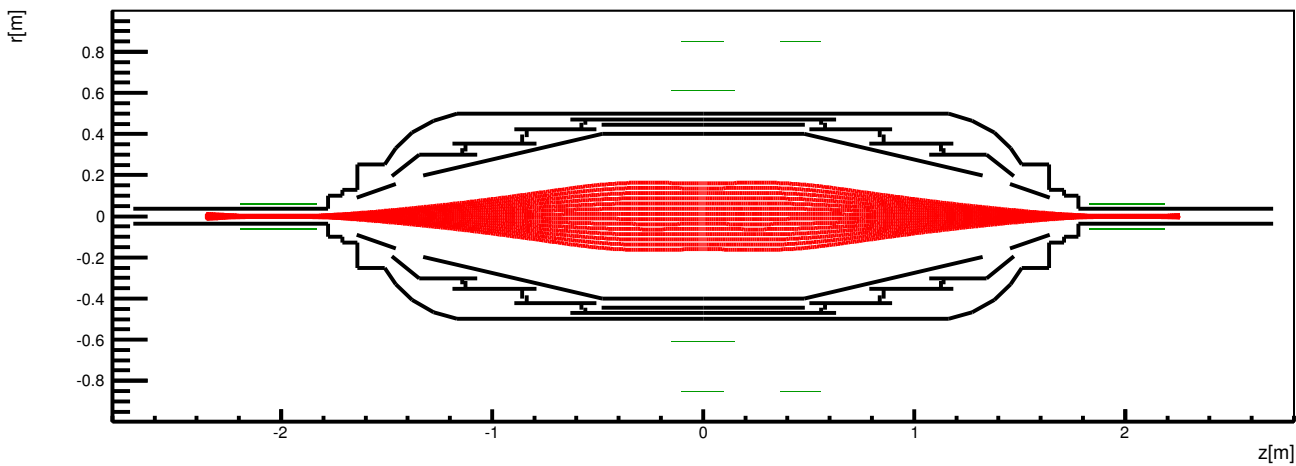


Figure E.10.: Two horizontal loops at 0 A current. Both solenoids at 25 A for a comparison of the background at different field widening.

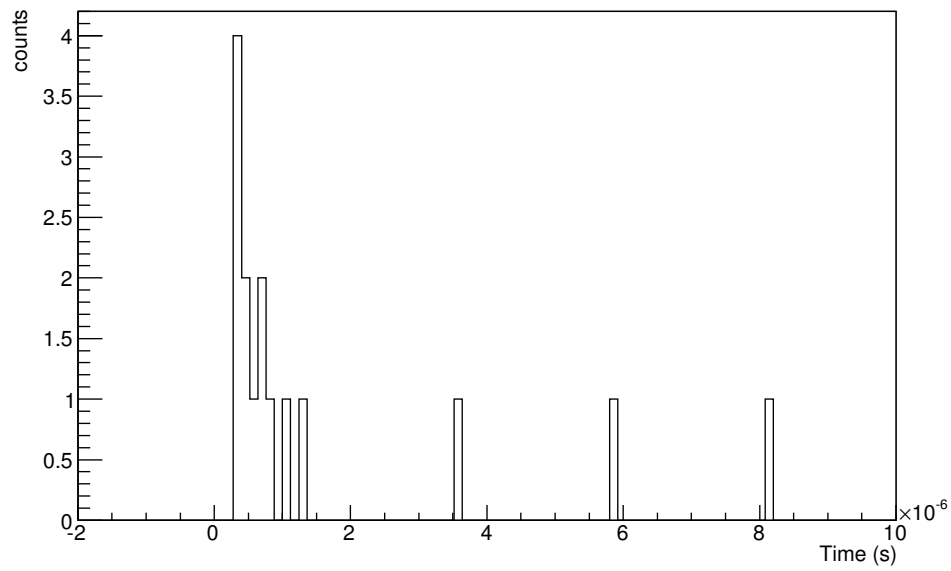


Figure E.11.: Two horizontal loops at 0 A current. Both solenoids at 25 A for a comparison of the background at different field widening. Some events occur in the expected time window.

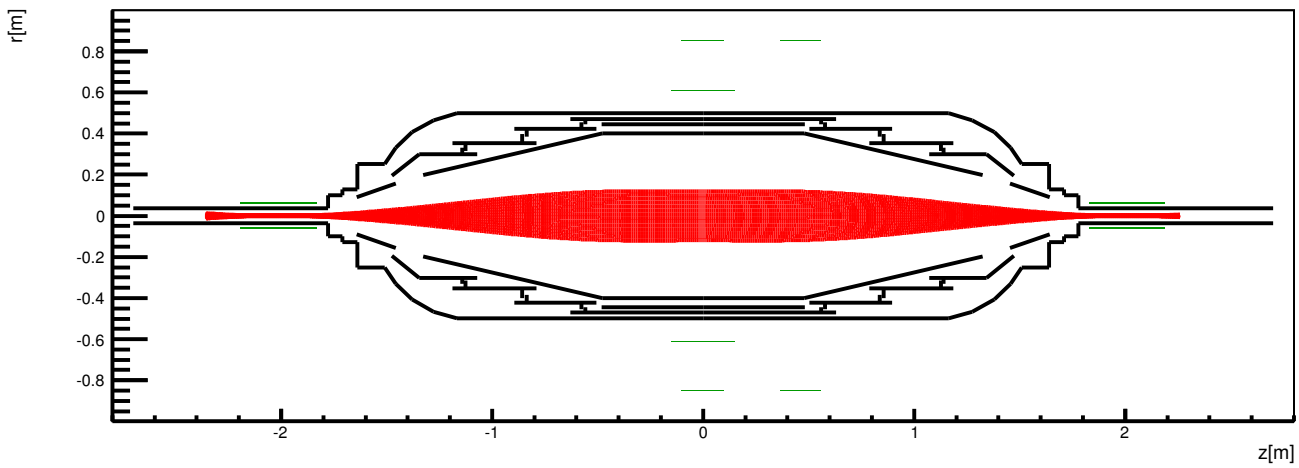


Figure E.12.: Two horizontal loops at 0 A current. Both solenoids at 12.5 A for a comparison of the background at different field widening.

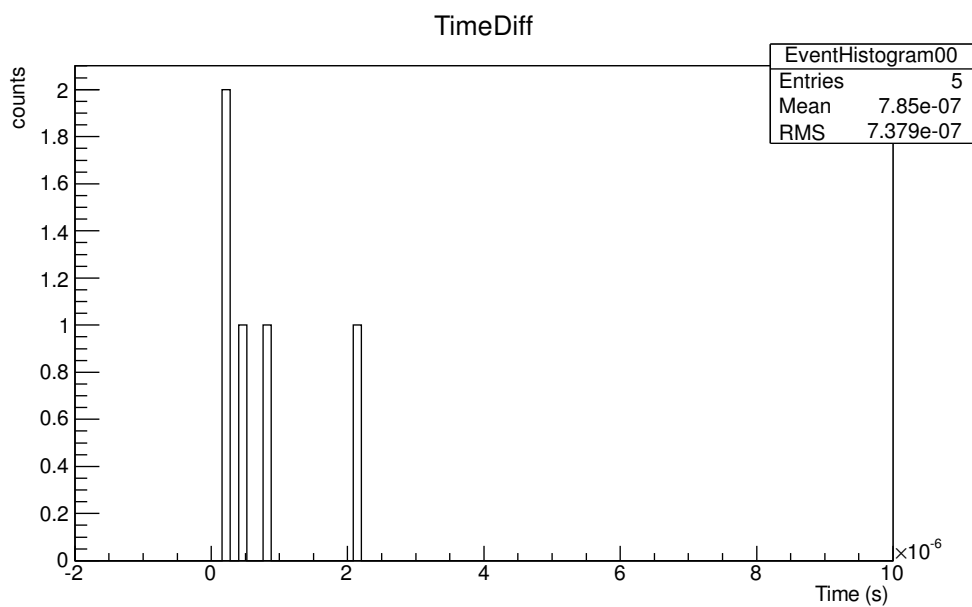


Figure E.13.: Two horizontal loops at 0 A current. Both solenoids at 12.5 A for a comparison of the background at different field widening.

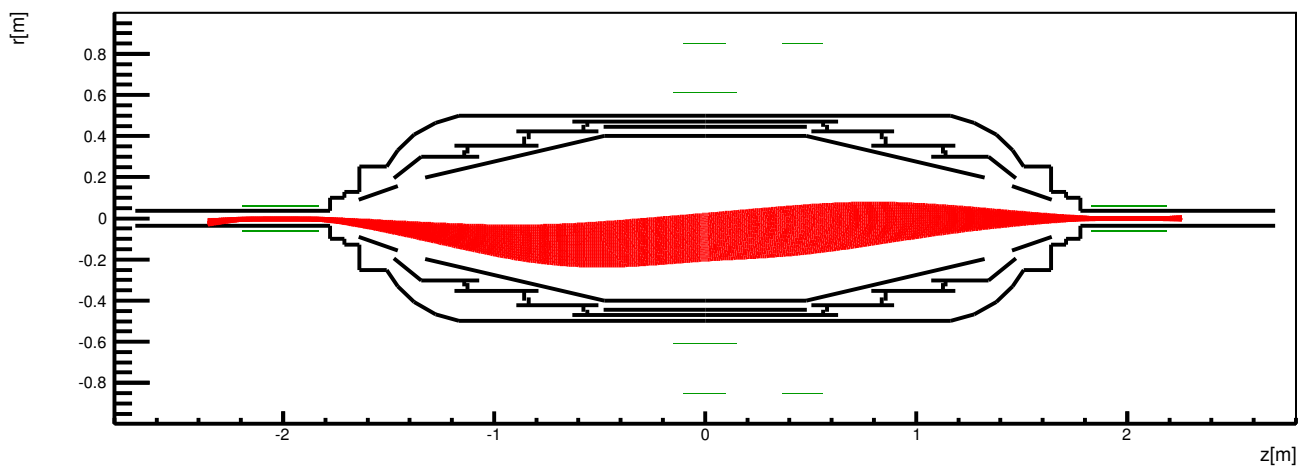


Figure E.14.: Two horizontal loops at 50 A current. Both solenoids at 12.5 A. Shift of the flux tube downwards visible.

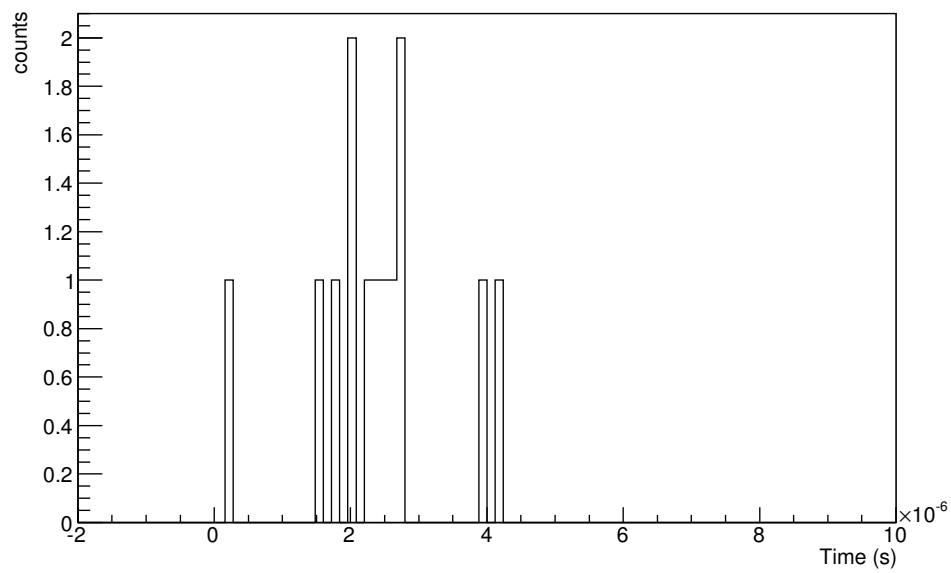


Figure E.15.: Two horizontal loops at 50 A current. Both solenoids at 12.5 A

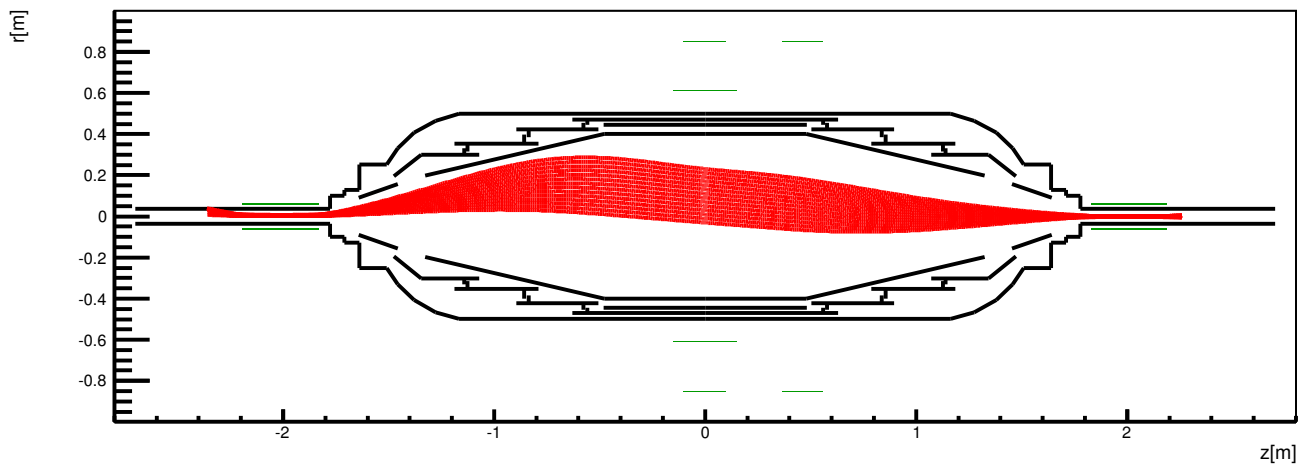


Figure E.16.: Two horizontal loops at -50 A current. Both solenoids at 12.5 A . Shift of the flux tube upwards visible.

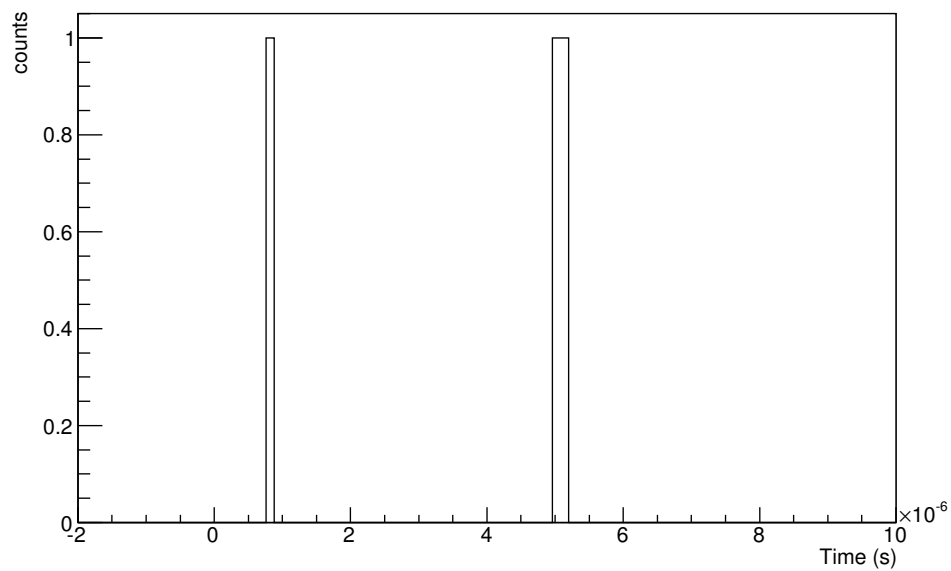


Figure E.17.: Two horizontal loops at -50 A current. Both solenoids at 12.5 A .

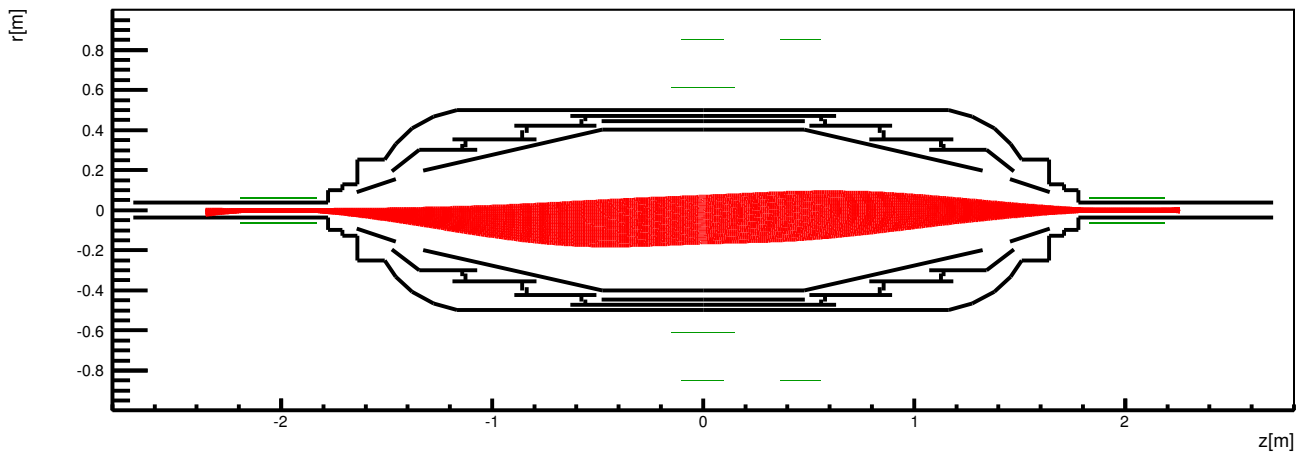


Figure E.18.: Two horizontal loops at 25 A current. Both solenoids at 12.5 A. Shift of the flux tube downwards visible.

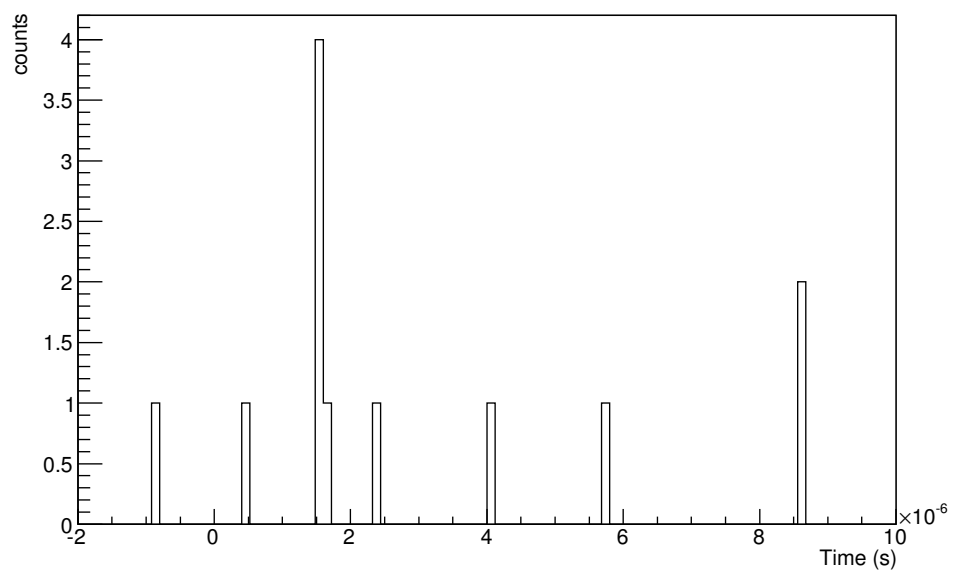


Figure E.19.: Two horizontal loops at 25 A current. Both solenoids at 12.5 A.

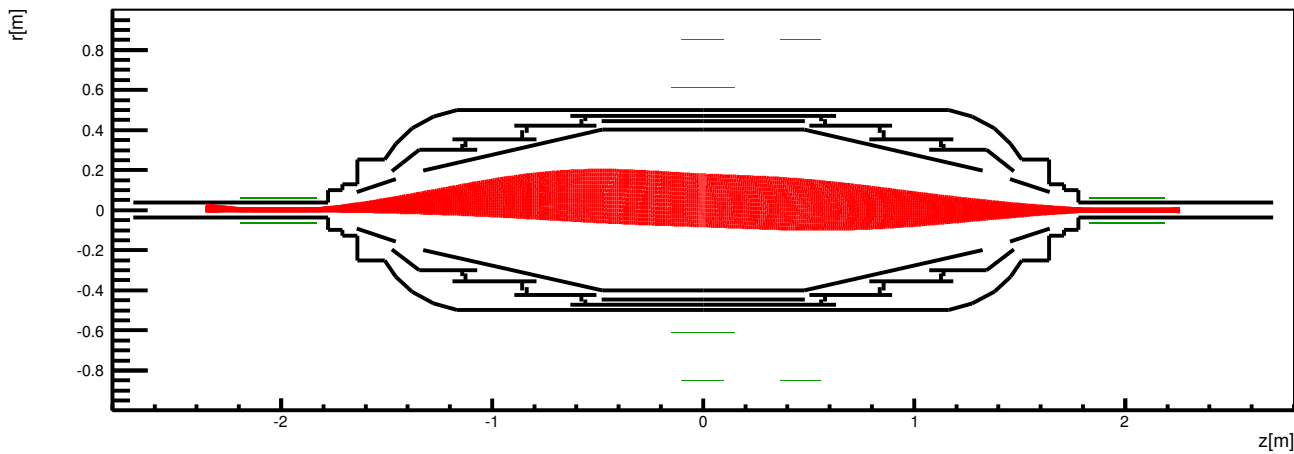


Figure E.20.: Two horizontal loops at -25 A current. Both solenoids at 25 A . Shift of the flux tube upwards visible.

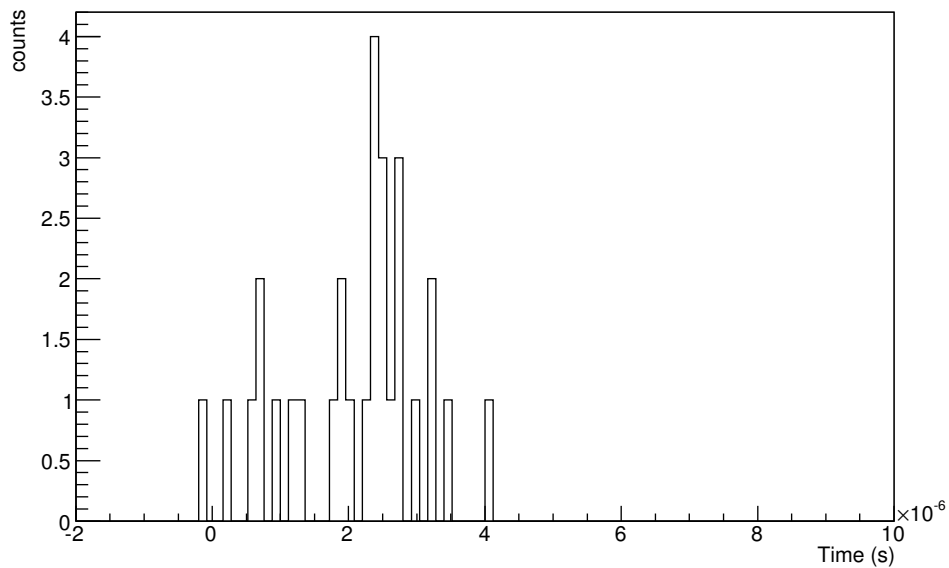


Figure E.21.: Two horizontal loops at -25 A current. Both solenoids at 25 A . Unexpectedly low counts probably due to a off-detector flux tube.

F. Main spectrometer analysis

G. A vis.mac file

```

# Macro file for the visualization setting in the initialization phase
# of the Geant4 simulation when running in interactive mode
#
# Use this open statement to create an OpenGL view:
/vis/open OGL 600x600-0+0
#
# Disable auto refresh and quieten vis messages whilst scene and
# trajectories are established:
/vis/viewer/set/autoRefresh false
/vis/verbose warnings
#
# Draw geometry:
/vis/drawVolume
#
# Specify view angle and zoom:
/vis/viewer/set/viewpointVector 0 0 1
#/vis/viewer/set/viewpointThetaPhi 40 40
/vis/viewer/zoomTo 2
#
# Specify style (surface, wireframe, auxiliary edges, display limit...)
/vis/viewer/set/style wireframe
/vis/viewer/set/auxiliaryEdge true
/vis/ogl/set/displayListLimit 100000000
#
# Draw smooth trajectories at end of event, showing trajectory points
# as markers 1 pixel wide:
/vis/scene/add/trajectories smooth
/vis/modeling/trajectories/create/drawByCharge
/vis/modeling/trajectories/drawByCharge-0/default/setDrawStepPts true
/vis/modeling/trajectories/drawByCharge-0/default/setStepPtsSize 1
#
# Draw hits at end of event:
/vis/scene/add/hits
#
# To draw only muons:
/vis/filtering/trajectories/create/particleFilter
/vis/filtering/trajectories/particleFilter-0/add mu+
# To superimpose all of the events from a given run:
/vis/scene/endOfEventAction accumulate
#
# Re-establish auto refreshing and verbosity:
/vis/viewer/set/autoRefresh true
/vis/viewer/set/background grey
/vis/viewer/set/projection perspective
/vis/verbose warnings
#
#Generate 5 muon events with the distribution provided in the code
/run/beamOn 5

```

Danksagung

Bei der Entstehung dieser Arbeit hatte ich Unterstützung von zahlreichen Personen, ohne die ich die Vielzahl an Probleme und Aufgaben nicht in diesem Umfang hätte lösen können. Dafür bedanke ich mich sehr herzlich. Besonderer Dank geht an:

Prof. Drexlin dafür, meine Diplomarbeit am Großprojekt KATRIN schreiben zu dürfen und dafür, durch eine interessante Vorlesung mein Interesse an Teilchenphysik geweckt zu haben.

Prof. Husemann für das Interesse an meiner Arbeit und die Übernahme der Zweitkorrektur.

Nancy Wankowsky für die Übernahme der Betreuung und die interessante Themenstellung sowie zahllose Korrekturen ohne die ich wahrscheinlich verzweifel wäre

Benjamin Leiber für zahlreiche Hilfestellungen, das Korrekturlesen, eine gute Zusammenarbeit und Messphasen mit Wartezeitverkürzung bei Rad & co.

Moritz Erhard und Norman Haußmann für das mehrfach gekürzte beste Büro, sehr hilfreiche Kommentare und Hilfestellungen während des Schreibens - sowie für das "constant noise level" [78], das mir die Zeit bei KATRIN versüßt hat.

Den Gaunern vom Detektor, die sich immer bemüht haben, dem kleinen aus dem Keller zu helfen - und dabei kein Blatt vor den Mund genommen haben.

Marco Haag für zahlreiche Hilfestellungen beim Lösen von C++ Problemen, die für ihn keine waren.

Florian Fränkle, der sich immer, wenn er am Projekt war, um meine Belange gekümmert hat.

Denis Tcherniakhovski für die grossartige Hilfe bei der Detektorsynchronisierung und anderen Fragen zur DAQ.

Arman Beglarian und Stefan Görhardt für die Hilfe bei der Kalibrierung der Luftspulen und die angenehme Arbeitsatmosphäre.

Und zuletzt meine Eltern, die mir das Studium ermöglicht, mich aber bei weitem nicht nur finanziell unterstützt haben, meinen Schwestern auf die ich immer zählen kann und Sinah - die wohl am meisten unter der Endphase gelitten hat, aber immer cool geblieben ist.